Diverse Lithologies and Alteration Events on the Rim of Noachian-Aged Endeavour Crater, Meridiani Planum, Mars: *In-Situ* Compositional Evidence

David W. Mittlefehldt[1], Ralf Gellert[2], Scott vanBommel[2], Douglas W. Ming[3], Albert S. Yen[4], Benton C. Clark[5], Richard V. Morris[1], Christian Schröder[6], Larry S. Crumpler[7], John A. Grant[8], Bradley L. Jolliff[9], Raymond E. Arvidson[9], William H. Farrand[5], Kenneth E. Herkenhoff[10], James F. Bell III[11], Barbara A. Cohen[12], Göstar Klingelhöfer[13], Christian M. Schrader[14], James W. Rice[15]

[1]Mail code XI3, Astromaterials Research Office, NASA/Johnson Space Center, Houston, TX 77058, USA.

[2]Department of Physics, University of Guelph, Guelph, ON N1G2W1, Canada.

[3]Mail code XI1, Astromaterials Research and Exploration Science Division, NASA/Johnson Space Center, Houston, TX 77058, USA.

[4]Jet Propulsion Laboratory, California Institute of Technology, Pasadena, CA 91125, USA.

[5]Space Science Institute, 4750 Walnut St., number 205, Boulder, Colorado 80301, USA.

[6]Biological and Environmental Sciences, Faculty of Natural Sciences, University of Stirling, Stirling FK9 4LA, Scotland, UK.

[7]New Mexico Museum of Natural History and Science, 1801 Mountain Rd NW, Albuquerque, New Mexico 87104, USA.

[8]Smithsonian Institution, NASM CEPS, 6th at Independence Ave. SW, Washington, DC 20560, USA.

[9]Department of Earth and Planetary Sciences, Washington University in Saint Louis, Saint Louis, MO 63130, USA.

[10]U. S. Geological Survey Astrogeology Science Center, Flagstaff, AZ 86001, USA.

[11]School of Earth and Space Exploration, Arizona State University, Tempe, AZ 85287, USA.

[12]NASA/Goddard Space Flight Center, Greenbelt, MD 20771, USA.

[13]Institute of Inorganic & Analytical Chemistry, Johannes Gutenberg-University Mainz, 55099 Mainz, Germany.

[14]Geology Department, SUNY-Potsdam, Potsdam, NY 13676, USA.

[15]Planetary Science Institute, 1700 East Fort Lowell Rd., Suite 106, Tucson, AZ 85719, USA.

Journal of Geophysical Research: Planets

Submitted: 01 November 2017

Revised: 07 February 2018

Abstract

We report the results of geological studies by the *Opportunity* Mars rover on the Endeavour Crater rim. Four major units occur in the region (oldest to youngest): the Matijevic, Shoemaker, Grasberg and Burns formations. The Matijevic formation, consisting of fine-grained clastic sediments, is the only pre-Endeavour-impact unit and might be part of the Noachian etched units of Meridiani Planum. The Shoemaker formation is a heterogeneous polymict impact breccia; its lowermost member incorporates material eroded from the underlying Matijevic formation. The Shoemaker formation is a close analog to the Bunte Breccia of the Ries Crater, although the average clast sizes are substantially larger in the latter. The Grasberg formation is a thin, fine-grained, homogeneous sediment unconformably overlying the Shoemaker formation, and likely formed as an airfall deposit of unknown areal extent. The Burns formation sandstone overlies the Grasberg, but compositions of the two units are distinct; there is no evidence that the Grasberg formation is a fine-grained subfacies of the Burns formation. The rocks along the Endeavour Crater rim were affected by at least four episodes of alteration in the Noachian and Early Hesperian: (i) vein formation and alteration of pre-impact Matijevic formation rocks; (ii) low-water/rock alteration along the disconformity between the Matijevic and Shoemaker formations; (iii) alteration of the Shoemaker formation along fracture zones; and (iv) differential mobilization of Fe and Mn, and $CaSO_4$-vein formation in the Grasberg and Shoemaker formations. Episodes (ii) and (iii) possibly occurred together, but (i) and (iv) are distinct from either of these.

1. Introduction

Mars Exploration Rover (MER) *Opportunity* has been exploring the geology of Meridiani Planum within Arabia Terra since landing on 25 January 2004. For over 7 Earth years, *Opportunity* traversed the hematite-rich plains making observations of sulfate-rich sedimentary rocks and associated hematitic concretions [*Arvidson et al*., 2011; *Squyres et al*., 2006] mapped as part of the Hesperian and Noachian highland undivided unit on the global geologic map of Mars [*Tanaka et al*., 2014]. On Sol (Mars day) 2681 (09 Aug. 2011), *Opportunity* reached the northwestern rim of Endeavour Crater, a 22 km diameter impact structure (Fig. 1a) formed in Noachian aged materials that predate the embaying sulfate-rich sedimentary rocks [*Arvidson et al*., 2014; *Hynek et al*., 2002]. The Endeavour Crater rim was chosen as a geological target because the rocks record an ancient epoch in martian history, and because orbital infrared data show that phyllosilicate minerals are present on portions of the rim, thereby implying that a period of aqueous alteration is recorded in the rocks [*Wray et al*., 2009]. Thus, exploration of the Endeavour Crater rim directly addresses one of the main goals of the MER mission: explore regions and associated rocks and soils where water might have been present and make assessments regarding past habitability [*Squyres et al*., 2003].

Opportunity arrived at the Endeavour Crater rim at Cape York, an ~700 m long segment rising just above the surrounding hematite plains (Fig. 1b). Shoemaker Ridge forms the spine of Cape York and is the type locality for the Noachian impact material of the rim, which has been informally named the Shoemaker formation [*Crumpler et al*., 2015a; *Squyres et al*., 2012].

Opportunity began investigations of the Endeavour rim at Spirit Point, the southwestern tip of Cape York, and then traversed northeast along the western (outboard) side of Cape York, climbed to the ridge crest and returned, rounded the northern tip, and traversed southwest along the eastern side. Roughly midway down the eastern side, an extensive investigation of the central portion of the rim segment was done because information from the Compact Reconnaissance Imaging Spectrometer for Mars (CRISM) instrument onboard the Mars Reconnaissance Orbiter (MRO) indicated the presence of ferric smectite in this region [*Arvidson et al*., 2014]. The investigation included a looping reconnaissance traverse from the eastern margin of Cape York, up to and along the ridge crest, back down to the eastern margin, followed by intensive study of selected regions identified as being of especial geological interest.

Subsequent to the exploration of Cape York, *Opportunity* was commanded to drive south to the next rim segment, Cape Tribulation. Along the way, cursory exploration of two small rim portions named Sutherland Point and Nobbys Head was done (Fig. 1b). Cape Tribulation was reached just east of its northern tip, a region named Solander Point (Fig. 1c). *Opportunity* rounded the northern tip, climbed along Murray Ridge, which forms the spine of the northern portion of Cape Tribulation, investigated rocks and soils within Cook Haven [*Arvidson et al*., 2016], and then traversed southward along the western side of Murray Ridge. The latter included investigations of the rocks on the outboard bench and up on Murray Ridge. *Opportunity* also did a reconnaissance investigation of a short, ~160 m long SW-NE trending ridge west of the Murray Ridge bench named Wdowiak Ridge (Fig. 1c). On Sol 3847 (18 Nov. 2014) *Opportunity* reached the northern end of a large, unnamed ridge and investigated bedrock in the Hueytown fracture zone on the outboard side of the ridge (Fig. 1c).

The rocks discussed here are all outcrop, ejecta-block and float-rock targets analyzed between sols 2669 and 3866 (28 July 2011 through 10 Dec. 2014), from the last plains outcrop prior to reaching Spirit Point, through to the Hueytown fracture zone. Subsequent to our investigations at the Hueytown fracture zone, *Opportunity* began investigations in Marathon Valley. Rocks from this region are briefly mentioned for textural comparisons, but they are not a focus of this paper. Soil analyses are not discussed.

The instruments of the Athena payload [*Squyres et al*., 2003] were used to investigate materials along the Endeavour rim: the Alpha Particle X-ray Spectrometer (APXS; *Rieder et al*. [2003]), the Microscopic Imager (MI; *Herkenhoff et al*. [2003]), the Panoramic Camera (Pancam; *Bell et al*. [2003]) and the Rock Abrasion Tool (RAT; *Gorevan et al*. [2003]), all supported by imaging from the engineering cameras – Navigation Cameras (Navcam) and front and rear Hazard Avoidance Cameras (Hazcam) [*Maki et al*., 2003]. Prior to arrival at Cape York, the Miniature Thermal Emission Spectrometer [*Christensen et al*., 2003] had ceased operating. By the time *Opportunity* had reached Cape York, the ^{57}Co source of the MIMOS II Mössbauer Spectrometer [*Klingelhöfer et al*., 2003] had decayed to the point where useful measurements were no longer possible.

The major focus of this paper is on the compositional information returned by the APXS and their use in defining alteration processes, but these data are not considered in isolation. We first put our study into geological context using information derived from orbital and *in-situ* mapping. Pancam and Navcam images are used to interpret outcrop textures and structures, and Pancam spectra are used to constrain mineralogy. The micro-textures of the rocks are interpreted from MI images. The Mars observations are then compared to a terrestrial analog site, the Ries Crater and tied into information derived from cratering mechanics studies. Finally, the observations discussed here are developed into a geological and alteration history for the region around Endeavour Crater.

2. The APXS Dataset

The APXS determines chemical compositions of rocks and soils using X-ray spectroscopy after irradiation with energetic alpha particles and X-rays. It therefore resembles a combination of the standard laboratory methods of X-ray fluorescence spectrometry (XRF) and particle induced X-ray emission spectrometry [*Rieder et al*., 2003]. The typical analysis field of view has a diameter of about 38 millimeters, with the instrument response being strongest in the central region. Concentrations are extracted from the X-ray spectra using the empirical method described in *Gellert et al*. [2006]. The areas of the characteristic peaks of each element are determined with a non-linear least-squares-fit algorithm and the peak areas are then quantified into elemental concentrations using the calibration sample set for MER, comprised of about 50 geological reference materials and additional simple chemical compounds (cf., *Gellert et al*. [2006]; *Rieder et al*. [2003]). For each major and minor element, the typical oxide – Na_2O for quantified Na, MgO for Mg, etc. – is assumed. The major element Cl and trace elements Ni, Zn, and Br are treated as elemental in the data reduction. Iron is reported as FeO because the Fe^{3+}/Fe^{2+} speciation could no longer be determined using the Mössbauer spectrometer. The sum of all components is normalized to 100% to compensate for a variable standoff distance. In the analysis model, self-absorption is taken into account using the assumption of a homogeneous, glass-like sample. This assumption is probably never correct, and is the underlying reason for a lower accuracy compared to analyses of glass disks in standard XRF. The absorption of the emitted X-rays, especially for lower Z elements that come from depths of only a few micrometers, depends on the composition of the host phase. Of necessity, absorption corrections for the APXS data use the average sample composition.

The results are reported with uncertainties for each element that represent 2σ precision errors of the peak areas (e.g., *Gellert et al*. [2006]; *Ming et al*. [2008]). Precision uncertainties are well suited to judge the similarity of samples rather than using the larger accuracy errors, and can be used to group rocks by their similar compositions. The rocks likely share a similar mineralogy and therefore any inaccurate corrections in the APXS analysis stemming from microscopic heterogeneity would be minimized for these rocks. The validity of using precision error bars for comparing and grouping rocks in classes is justified by the nearly identical and consistent composition of fine-grained, homogeneous igneous rocks like the Adirondack basalts from Gusev Crater analyzed by sister rover *Spirit* [*Gellert et al*., 2006; *McSween et al*., 2006].

The relatively large accuracy error bars can be explained in part by the very different compositions of possible minerals. For example, two possible Cl-rich minerals include NaCl and $NaClO_4$, where the difference in oxygen causes differences in the absorption cross sections that are needed for accurate correction. Independent knowledge of the mineralogy and phase distributions within the targets would be required to improve the accuracy of analyses. Table S1 of the on-line supplement gives the typical relative accuracy of the measurement, which is repeated from Table 1 by *Gellert et al*. [2006]. These accuracy measures are compared to the relative precision for the Shoemaker formation target Transvaal. This target has a composition close to the mean Shoemaker formation breccia, and an integration time close to the median of all Shoemaker formation target integrations. Thus, the precision of this analysis is typical for the APXS measurements reported here.

3. Geological Context

The oldest geologic structure in the region of Meridiani Planum is an ancient multiring basin that is at least 800, and possibly 1600 km, in diameter (Fig. 2a); the lithologic units of Meridiani Planum were deposited on this structure [*Newsom et al*., 2003]. Endeavour Crater was formed in materials of Noachian age. The basal unit in the immediate vicinity of the Meridiani plains is the Early to Middle Noachian highlands subdued crater unit (Fig. 2b) which is interpreted to be composed of a mixture of primary (volcanic, pyroclastic) and secondary (impact breccia, fluvial and aeolian sedimentary) rocks with a crater-density model age of ~3.9 Ga [*Hynek and Di Achille*, 2017]. This highlands unit is overlain by several hundreds of meters of Meridiani etched plains units; the lower two are Middle to late Noachian in age; the topmost unit is Late Noachian/Early Hesperian in age (Fig. 2b). The etched units are interpreted to be aeolian and/or volcanic deposits, with a combined crater-density model age also of roughly 3.9 Ga [*Hynek and Di Achille*, 2017; *Hynek and Phillips*, 2008]. The Burns formation investigated by *Opportunity* is the uppermost part of the etched unit stratigraphy. Based on mineralogy, composition, texture, and primary sedimentary features, the Burns formation is interpreted to be a sulfate-rich aeolian sandstone (e.g., *Squyres et al*. [2006]). The region is capped by the thin, surficial Hematite unit, mapped as Early Hesperian [*Hynek and Di Achille*, 2017]. This is an unconsolidated lag deposit rich in hematitic concretions derived from erosion of the underlying the Burns formation, plus basaltic sands in aeolian bedforms [*Squyres et al*., 2006].

Endeavour Crater lies to the northeast of Miyamoto Crater (Fig. 2a) [*Grant et al*., 2016; *Newsom et al*., 2003], an ~160 km diameter impact structure containing Fe-Mg-rich smectite phases on its floor [*Wiseman et al*., 2008]. Formation of the smectites is thought to have been engendered by the hydrological environment of western Arabia Terra in which groundwaters from the highlands to the south emerged from local topographic lows and promoted in-situ alteration of primary or impact-generated rocks [*Andrews-Hanna and Lewis*, 2011; *Andrews-Hanna et al*., 2007]. The Endeavour impact occurred well within the region where the continuous ejecta blanket of Miyamoto Crater would have been, and the pre-impact target stratigraphy would have included polymict breccias from that earlier impact. These could have been altered as were the Miyamoto Crater floor rocks.

Most of Endeavour Crater and portions of its rim are unconformably buried by the sulfate-rich sandstones of the Burns formation (Fig. 2c) [*Arvidson et al*., 2011; *Grant et al*., 2016; *Squyres et al*., 2006]. Portions of the crater rim rise above the Burns formation strata, forming a discontinuous ring of rim segments. There is no evidence, such as fragments of Burns rocks or hematitic concretion clusters high on the rim, that the Burns formation covered these rim segments. *Golombek et al*. [2006] estimated that ≤80 m of rock has been eroded in Meridiani Planum since the Hesperian, and *Grant et al*. [2016] estimated that Burns formation rocks might have been 80-100 m higher than at present in the region of Cape Tribulation. These estimates are less than the current Cape Tribulation height above the plains. Erosion has variably degraded the crater rims with on the order of 100-200 m having been removed, mostly before deposition of the Burns formation sands [*Crumpler et al*., 2015a; *Grant et al*., 2016]. Some of the rim segments show the infrared spectral signature of Fe-Mg-smectite clays in data returned by the CRISM instrument onboard MRO [*Fox et al*., 2016; *Noe Dobrea et al*., 2012; *Wray et al*., 2009], suggesting that they have undergone aqueous alteration under conditions of circumneutral pH. A localized area in the region explored by *Opportunity* during the sols covered here has yielded detections of phyllosilicates by CRISM (Fig. 1c). On the inboard side of Cape York is a small area on a feature dubbed by the team as Matijevic Hill that is thought to contain a few weight percent ferric smectites [*Arvidson et al*., 2014].

Burns formation sandstones are dominated by Mg-, Ca-, and Fe-sulfates, a silicic component and ferric oxides (e.g., *Clark et al*. [2005]; *Klingelhöfer et al*. [2004]; *McLennan et al*. [2005]; *Morris et al*. [2006a]). The sandstones are mostly aeolian in origin, with some aqueous facies that indicate local fluvial reworking, and a minor component of mudstones indicating localized deposition in quiet water, possibly a lacustrine setting [*Edgar et al*., 2012, 2014; *Grotzinger et al*., 2005, 2006; *Hayes et al*., 2011]. The sediments have undergone groundwater-influenced cementation and diagenesis, and are noteworthy for containing abundant hematitic concretions. They document a period of aqueous activity postdating the formation of Endeavour Crater in which groundwaters interacted with and altered mafic composition rocks (e.g., *Hurowitz et al*. [2010]). The solutions evaporated to form sulfate-rich evaporitic muds, which were subsequently redistributed by wind and water under increasingly arid conditions to form sandstones. Rocks of the Burns formation are not a focus of this paper, but we do discuss those Burns formation targets from near the margins of the Endeavour rim for comparison with rocks on the rim proper (Table S2). These targets are referred to here as “Burns margin.” We include in Table S2 the last Burns formation target analyzed before reaching Cape York, Gibraltar, and two Burns formation targets from the saddle between Cape York and Cape Tribulation, Tawny and Black Shoulder. These targets are approximately 320, 340 and 190 m from the nearest rim margins and are not included under the sobriquet “Burns margin” in the discussion.

The rocks of the Endeavour Crater rim have been divided into three units which are, oldest to youngest; the Matijevic, Shoemaker and Grasberg formations (Fig. 2c) [*Crumpler et al*., 2015a]. A continuous bench of bright rock surrounding Cape York, Sutherland Point and Nobbys Head, and partially along the margin of Cape Tribulation, is discernable in High Resolution Imaging Science Experiment (HiRISE) images of the western rim of Endeavour Crater (Fig. 1b, c). This bench is part of the Grasberg formation [*Crumpler et al*., 2015a]. Benches of bright rock are visible in HiRISE images around other rim segments of Endeavour Crater and these are interpreted to be Grasberg formation outcrops [*Grant et al*., 2016]. The spine of Cape York is formed by Shoemaker Ridge and is the type locality for the Shoemaker formation. This name is given to the polymict impact breccias of basaltic composition that comprise the major lithology of the Endeavour Crater rim [*Squyres et al*., 2012]. The Matijevic formation, consisting of bright clastic rock of basaltic composition [*Arvidson et al*., 2014], has been encountered only on the inboard side of Cape York at the base of Matijevic Hill (Fig. 1b). Murray Ridge is notable for having localized concentrations of dark-rock float (Figs. 3a, b), and Wdowiak Ridge is capped by fine-grained dark rocks (Fig. 3c). The former are allochthonous, while the latter cannot be placed within the local stratigraphic framework. Both are of uncertain provenance.

4. Rock Outcrop and Microscopic Textures

To set the stage for the discussion of unit compositions to follow, we present observations on outcrop morphology, and macroscopic and microscopic textures of the various lithologies on Endeavour Crater rim in this section. We also discuss constraints on mineralogy derived from Pancam spectra. The order in which the rock units are discussed mirrors the discussion of the compositions of lithologies in Section 5 and is not in stratigraphic sequence. Section 5 is ordered by the specific science issues we wish to explore. Observations for some of the rock types have been described previously [*Arvidson et al*., 2014, 2016; *Clark et al*., 2016; *Crumpler et al*., 2015a; *Farrand et al*., 2013, 2014; *Squyres et al*., 2012]. The outcrop morphology and textures for the units discussed here are summarized in Table 1. Details for the Pancam images used in this paper are given in Table S3 of the on-line supplementary material.

4.1. Grasberg Formation

The Grasberg formation is the oldest of the post-impact formations in the area and occurs as a shallowly tilted bench on the margins of both rim segments investigated by *Opportunity*. The description of the formation given here is largely derived from *Crumpler et al*. [2015a] plus new observations; *Crumpler et al*. [2015a] will be cited for specific interpretations, but not for basic descriptive information.

The Grasberg formation consists of an upper bright unit and a lower dark unit with a total formation thickness estimated as 1-2 m. The rocks are homogeneous and fine-grained, and are planar in outcrop (Fig. 4). The Grasberg formation presents hackly outcrop surfaces that are fractured into polygonal blocks or slabs (Fig. 4a, e). Sedimentary structures are lacking in most outcrops, but an exception is the lower unit target Poverty Bush from Solander Point which shows fine-scale, wavy laminations (Fig. 4e, arrows). Outcrops can exhibit fine-scale jointing (Fig. 4c). Outcrops of the lower Grasberg unit are commonly transected by bright veins tens of cm in length and of roughly cm-scale width (Fig. 4d). Short, bright streaks in the upper Grasberg unit could represent smaller versions of the coarse veins that are common in the lower unit (Fig. 4a, arrows). The contact between the lower and upper units is defined only by a color transition and no obvious textural or morphological difference is evident; the upper unit might simply reflect an indurated cap rock formed by weathering [*Crumpler et al*., 2015a]. Rocks of both units are composed of grains with diameters smaller than the ~100 µm (3 pixels) resolution of the MI (Fig. 5); clastic textures are generally not observed. If the texture is primary, then the homogeneous, fine-grained nature suggests deposition occurred in a relatively low-energy environment. Wind-polished surfaces show small pits that could belie initial porosity (Figs. 5c, d), but these are not evident in the interior of the only Grasberg formation target that was abraded (Fig. 5a). If that upper unit target is representative of the formation, then the Grasberg formation consists of homogeneous fine-grained rock later cut by veins (cf., *Crumpler et al*. [2015a]).

The Grasberg formation is distinct from the Burns formation sandstones in mineralogy and texture. The visible to near infrared (VNIR) reflectance spectra of the upper Grasberg resembles purple-colored Burns formation outcrops that have higher 482 to 535 nm slopes as described by *Farrand et al*. [2007]. However, the upper Grasberg has deeper 535 and 904 nm band depths indicative of higher fractions of crystalline red hematite in that unit and thus is mineralogically distinct from the Burns formation [*Farrand et al*., 2014]. The very fine-grained nature of the Grasberg formation is also distinct from coarser, sand-sized Burns formation sandstones (e.g., *Grotzinger et al*. [2005], and see *Crumpler et al*. [2015a]).

On Cape York, the Grasberg formation dips ~10° away from the rim segment in all directions, and is interpreted to lie on an erosional pediment forming the lower slopes of Cape York [*Crumpler et al*., 2015a]. The geometry of the Grasberg formation indicates that it underlies the Burns formation, and is interpreted to have unconformities as its lower and upper contacts [*Crumpler et al*., 2015a]. These authors inferred that the Grasberg formation draped paleotopography and could be an airfall deposit that covers an extensive region, for example, a distal deposit of volcanic ash or fine-grained impact ejecta.

4.2. Matijevic Formation

The Matijevic formation occurs on the in-board side of the Cape York rim segment, where the rocks have been described by *Arvidson et al*. [2014], *Crumpler et al*. [2015a] and *Farrand et al*. [2014]. Matijevic formation outcrops are most commonly bright, planar and exhibit polygonal jointing (Fig. 6a). The matrix consists of fine-grained clastic material of basaltic composition with grains up to ~1 mm in size and contains variable amounts of 2-4 mm-sized spherules (Fig. 7a). Local concentrations of the 2-4 mm-sized spherules form small, discontinuous ridge-forming units (Fig. 6b). Broken spherules show a variety of textures – hollow, partially filled and solid – suggesting a possible diversity of mineralogies (Fig. 7d). Clast-supported textures are evident in places, perhaps indicative of reworking. Note that we previously suggested that more resistant outcrops rich in spherules (Fig. 6b) are possibly part of the Shoemaker formation [*Crumpler et al*., 2015a], but our evaluation of rock compositions (Section 5.2) shows that they are part of the Matijevic formation. Matijevic formation outcrops have relatively flat Pancam VNIR spectra with slight negative sloping near-infrared reflectance [*Farrand et al*., 2014].

Three types of late modifications to the Matijevic formation are present: (i) thin, bright crosscutting veins; (ii) dark, patchy veneers; and (iii) thicker boxwork veins. Locally, irregular, anastomosing, feathery veins a few-mm wide composed of bright material cut the Matijevic formation matrix (Figs. 6a, 7a, b). Bright outcrops commonly host numerous small, irregular patches of a dark veneer that partially cover exposed surfaces (Figs. 6a, 7c). The dark veneer displays a shallow 904 nm band not observed in the light-toned matrix [*Farrand et al*., 2014]. These patches are erosional remnants of what was likely a continuous cover [*Crumpler et al*., 2015a]. Raised irregular ridges in the veneer that can be traced to anastomosing veins in the underlying matrix (inset, Fig. 6a, arrows) indicate the veneer was formed after the veins were emplaced. The Matijevic formation locally hosts boxwork veins enriched in Si and Al; these are discussed in detail in *Clark et al*. [2016]. Veneers, termed coatings in *Clark et al*. [2016], are also present in the region of the boxwork veins. Imaging of the boxwork veins and coatings shows that the coatings occur on top of the boxwork veins that crosscut the Matijevic formation outcrops [*Clark et al*., 2016], suggesting again that the coatings/veneers formed relatively late.

Matijevic formation is interpreted to be a pre-impact lithology [*Arvidson et al*., 2014; *Crumpler et al*., 2015a; *Farrand et al*., 2014]. However, establishing the origin of the formation is hampered by the limited areal extent of unit exposures and the absence of diagnostic structures. It could be a regional deposit, for example airfall fines from a distant impact or volcanic eruption, or a more localized deposit formed by reworking fine-grained clastic material [*Crumpler et al*., 2015a].

The Endeavour Crater rim segments investigated by *Opportunity* are in the equivalent position as the tectonic rim (sometimes referred to as the crater boundary or structural rim) of the 26 km diameter Ries Crater (e.g., *Pohl et al*. [1977]; *Stöffler et al*. [2013]; cf., *Grant et al*. [2016]). The pre-impact rocks at the Ries tectonic rim are Jurassic sediments from the uppermost part of the pre-impact stratigraphy. By analogy, the Matijevic formation likely represents part of the Noachian middle or lower etched units, which together might be 350-400 m thick in this area (Fig. 2b, c; *Hynek and Di Achille* [2017]). However, the etched units are not exposed along the southern edge of the Hesperian Hematite unit (hematitic concretion lag deposit) (Fig. 2a) indicating the etched units must pinch-out in a generally south/southeast direction across Meridiani Planum and could be much thinner than the estimated section given above. The 19 km diameter Bopolu Crater, located 65 km southwest of Endeavour Crater near the margin of the Hematite unit, has a 75-260 m thick section of layered sulfates (Burns equivalent) overlying a Noachian section interpreted to be part of the subdued crater unit of *Hynek and Di Achille* [2017] (*Grant et al*. [2016], and personal communication). If this is the stratigraphy in the region around Endeavour Crater, then the Matijevic formation would be part of the subdued crater unit.

4.3. Shoemaker Formation

The Shoemaker formation makes up the continuous ejecta blanket surrounding Endeavour Crater. The formation has been divided into three informal members on Cape York [*Crumpler et al*., 2015a]. From the bottom up, they are the Copper Cliff, Chester Lake and Greeley Haven members. These informal member designations will be used here when needed to facilitate discussion of specific compositional distinctions. One of the Chester Lake rocks, Tisdale, is an ejecta block from Odyssey crater at Spirit Point on the southwestern tip of Cape York (Fig. 1b). The targets on this block have some textural, Pancam reflectance properties and compositional differences from the other Shoemaker formation breccias [*Squyres et al*., 2012]. The Tisdale targets will be highlighted in the discussion as needed. On Murray Ridge the Shoemaker formation is undivided. We investigated a set of outcrops on the northern part of Murray Ridge and a set about 500 m to the south in the general region of Pillinger Point (Fig. 1c). These will be referred to as “north” and “central” targets in the discussion. Roughly 1.5 km separate the central Murray Ridge targets from those at the Hueytown fracture zone on the northern edge of the unnamed ridge south of Wdowiak Ridge (Fig. 1c). Targets from Hueytown fracture zone are indicated separately on graphs.

Shoemaker formation rocks are coarse, typically unbedded breccias of basaltic composition consisting of dark, relatively smooth, subrounded to angular clasts up to about 10 cm in size embedded in a brighter, fractured, fine-grained matrix (Figs. 8, 9) [*Crumpler et al*., 2015a; *Squyres et al*., 2012]. The matrix and clasts are both relatively dark compared to the Matijevic formation matrix and have negative near-infrared slopes. For the matrix, the negative slope is generally flatter while for the clasts there can be an increase in reflectance from 934 to 1009 nm. This could indicate the presence of low-Ca pyroxene in the clasts. Clast sizes and abundances vary within the formation (Figs. 8a-c, e), but sorting is not evident on the outcrop scale. Some clasts have internal textures including brighter patches within a darker matrix (Fig. 9c, arrows) suggesting that they are composed of brecciated material. The clasts are commonly more resistant to physical weathering in the current martian environment and often stand in positive relief on outcrops; this texture is especially evident in Fig. 8a (arrows).

Lineations are present especially in the Chester Lake member, and consist of trains of clasts and parallel alignments of elongated clasts [*Crumpler et al*., 2015a; *Squyres et al*., 2012]. The morphology of these outcrops is similar to that of suevite breccias common in moderate to large impact structures on Earth [*Squyres et al*., 2012]. Terrestrial suevite contains clasts and matrix rich in impact melt (e.g., *Osinski et al*. [2004]). However, the instrument suite on *Opportunity* does not allow for positive identification of impact-melt glass in the rocks.

The lowest member, Copper Cliff, lies disconformably on the Matijevic formation [*Arvidson et al*., 2014; *Crumpler et al*., 2015a]. The Copper Cliff member includes some spherules and fine, bright, anastomosing veins (Figs. 8a, 9a) similar in morphology to those in the underlying Matijevic formation. Spherules in the Copper Cliff member decrease in abundance up section [*Arvidson et al*., 2014]. These spherules are not hematitic spherules as are present in the Burns formation. This is discussed in Section 5.2.1. Bright veins that are coarser than the fine, anastomosing veins within the Copper Cliff member are present in some outcrops on Murray Ridge and at the Hueytown fracture zone (Figs. 8d, f, 9d).

Roughly 750 m further south of the Hueytown fracture zone in the Marathon Valley area (Fig. 1c), the Shoemaker formation is divided into lower and upper units, but we have not yet attempted to correlate these with the stratigraphy elsewhere on the rim [*Crumpler et al*., 2017]. The upper unit is clast-rich with relatively coarse clasts and is similar to many of the rocks forming prominent protuberances on Murray Ridge. The lower unit is clast-poor with relatively small clasts. The rocks in the Hueytown fracture zone are texturally more similar to the latter (Fig. 8f). Outcrops at the Cook Haven location on the northern part of Murray Ridge similarly have lower clast abundances and the clasts are relatively small (Fig. 9b).

4.4. Dark-rock Float and Ejecta

Concentrations of dark-rock float are present at several locations on Solander Point and Murray Ridge. On the northeast side of Solander Point a low ridge covered with scattered float lies at the transition from the relatively flat Burns formation/Grasberg formation terrain to the lower slopes of Murray Ridge (Fig. 3a). Dark cap rocks and associated float were encountered on a series of ridges in the McClure-Beverlin Escarpment region south of the Cook Haven winter-over site (Fig. 3b). Coherent outcrop units that could be the sources of the rocks are not observed. The distributions are consistent with lenses rich in coarse blocks being present within the Shoemaker formation breccias. Alternatively, they could represent inversions of topography. For example, the dark rocks could have been emplaced as massive deposits, such as impact melt collected in a local low or as fragments of a massive unit that were mobilized and collected in a trough, that then made the trough more resistant to erosion [*Crumpler et al*., 2015b].

The float rocks are dark, angular, often with conchoidal fracturing and some are vesicular (Figs. 10a, b). In one instance a rock appears to have the morphology of a hexagonal prism (Fig. 10b), suggesting that it might be a fragment of a massive, columnar-jointed cooling unit – basalt or impact melt. The rocks are very fine-grained; grains or clasts larger than 100 µm are not visible (Figs. 11a, b).

Wdowiak Ridge is partially capped by a massive dark-rock unit (Fig. 3c), but *Opportunity* was not commanded to climb the slope to investigate the unit in situ. Our contact science on Wdowiak Ridge dark rocks was limited to float, and ejecta blocks from the ~30 m diameter Ulysses crater on the southwestern end of the ridge (Fig. 1c). The morphology of most of these rocks is similar to that of the dark-rock float from Solander Point and Murray Ridge: angular and showing conchoidal fracturing (Fig. 10c). Some Wdowiak Ridge rocks have a more irregular, hackly morphology (Fig. 10d). Unlike the float from Solander Point/Murray Ridge, vesicularity is uncommon amongst the Wdowiak Ridge rocks. Planar fractures or partings are common in these rocks [*Arvidson et al*., 2015]. Remnants of these fractures/partings are expressed as dark flakes on flat surfaces (Fig. 10c). The angular rocks have a very fine-grained texture with no crystals, grains or clasts >100 µm visible (Fig. 11c). A few rocks have hackly-morphology, and the one investigated in detail shows fracturing in almost orthogonal directions and a few grains ≥100 µm in size are visible (Fig. 11d, arrows).

5. Rock Compositions

Compositional data for all rock targets discussed here are presented in Table 2, and the uncertainties (2σ precision) are given in Table S4. A listing of the rock targets investigated, from the last Burns formation outcrop analyzed prior to arrival at Cape York through investigation of the Hueytown fracture zone, are presented in the on-line supplementary material (Table S2). The generalized locations of the targets are shown in Fig. 1b, c. The compositions of some of the rock types have been previously described [*Arvidson et al*., 2014; *Crumpler et al*., 2015a; *Squyres et al*., 2012], and some unique lithologic types formed by late-stage alteration have been discussed in detail [*Arvidson et al*., 2016; *Clark et al*., 2016].

The elements S, Cl, Zn and Br are the most labile in the recent (possibly current) martian environment (e.g., see *Gellert et al*. [2004]; *Haskin et al*. [2005]; *McSween et al*. [2004]; *Yen et al.* [2005]). Amongst the elements determined by the APXS, these show the greatest variations associated with alteration. We refer to these elements as volatile/mobile elements because their variations in the rocks and soils, coupled with the documented or inferred alteration mineralogy, indicate that these elements were vapor and/or fluid-mobile during alteration.

Most of the analyses are for untreated targets, that is, the rock surfaces as exposed by the martian environment. In most cases, targets were chosen that appeared in *Opportunity*-based images to have been swept clean by wind. The diamond-impregnated resin pads on the grinding wheel of the RAT are significantly worn down. The remaining abrasion capability has been judiciously used to balance the need to obtain critical knowledge of current lithologies with the need to have an abrasion capability for future use; only 8% of the Endeavour rim targets were abraded. Use of the brush was based on perceived need to clean rock surfaces and concerns for instrument safety; brushing was used on 19% of the targets.

Wind-swept, untreated rock surfaces can host litter, including lithic debris from the outcrops, aeolian sand and airfall dust. The lithic debris is coarser than the other two components and is likely derived from the outcrops being interrogated; accordingly, inclusion of lithic debris should not have a significant impact on determining outcrop compositions. Aeolian sand is mobile in the current environment as saltating sands that form ripples composed of 50-125 µm sized grains [*Sullivan et al*., 2005]. These sands are dark and basaltic in composition (e.g., *Yen et al*. [2005]). To evaluate the possible compositional effects of this aeolian sand, referred to here as dark sand, we use the compositions of five Meridiani Planum soil targets that are of uniformly fine grain size and free of lithic clasts as observed in MI images, and have low albedo as seen in Pancam images.

Dust grains are suspended in the atmosphere as a result of seasonal storms on Mars, and are in the size range 1-3 µm [*Pollack et al*., 1979, 1995]. This is consistent with dust-size calculations of ~3 µm diameter made for Gusev Crater and Meridiani Planum by the MER rovers [*Lemmon et al*., 2004]. The estimated sedimentation rate of this airfall dust is 0.002 g/cm^2 per year [*Pollack et al*., 1979], which could form a 20 µm thick “layer” of dust annually, assuming a density of 1 g/cm^3 for the deposit. To evaluate the possible compositional effects of this airfall dust we use the compositions of five Meridiani Planum soil targets that are bright, of uniformly very-fine grain size, free of lithic clasts as observed in MI images, and have dust spectral-characteristics as seen in Pancam images. We refer to these as bright soil. The dark-sand and bright-soil targets used for comparisons are given in the on-line supplementary material (Table S5).

Compositional characteristics of the rock units discussed here are summarized in Table 1. The characteristics are given in relation to the average of the Shoemaker formation outcrops, excluding compositionally anomalous targets. The adjectival "low" and "high" mean the elements are between 1.5 to 2 times the standard deviation from the mean of the Shoemaker formation, while "very low" and "very high" mean they are more than twice the standard deviation from the Shoemaker mean.

5.1. Grasberg Formation

Analyses were done on lower and upper Grasberg targets, and on two veins cutting across the lower member of the Grasberg formation (Table S2). For the eponymous Grasberg outcrop block, two untreated targets, a brushed target, and an abraded target plus offset were measured. The lower-unit rock Monjon included a portion showing the normal purple color in Pancam false-color images and a small patch of grey material (Fig. 4c); both targets were analyzed. Table 3 gives the average compositions for the units, the ratio of lower/upper and an average of the vein targets. Table 1 summarizes the compositional characteristics of the two units relative to an average of the Shoemaker formation. Although there are significant compositional differences between the Grasberg and Shoemaker formations, the former is nevertheless of broadly basaltic composition. The veins investigated are narrower than the APXS field of view and thus the compositions of vein targets represent mixtures of vein material, host rock, aeolian sands and possibly other lithic debris (Fig. 4d). The vein targets are higher in CaO and SO_3 compared to the lower Grasberg lithology that hosts them (Table 3). Vein targets from all stratigraphic units are discussed collectively later (Section 5.4).

As discussed in Section 3 and shown in Fig. 2c, the Burns formation overlies the Grasberg formation [*Crumpler et al.*, 2015a]. Although an unconformity separates them, one issue is whether the Grasberg formation is an earlier facies of the Burns formation. We examine this issue here. The composition of the Grasberg formation is well-resolved from that of the Burns formation (Fig. 12). Compared to the Burns, the Grasberg has lower MgO (Fig. 12a) and SO_3, and higher SiO_2, K_2O, TiO_2, FeO (Fig. 12c) and Zn (Fig. 12e). The Grasberg formation has higher Cl contents than the Burns formation, although a subset of Burns rocks have Cl contents that substantially overlap the range for the Grasberg (Fig. 12e).

The distinction in composition between the two formations is evident even comparing Grasberg targets only with those Burns formation targets located near the contact with the Grasberg (Burns margin in Fig. 12). Two Burns-margin targets – Callitris and Dibbler – plot within the field of Grasberg rocks for some elements (e.g., Figs. 12b-d), but nevertheless can be clearly distinguished from the Grasberg based on overall composition. Burns formation target Tawny, from the saddle between Nobbys Head and Solander Point, has an FeO content within the range of Grasberg formation rocks (Fig. 12c) but otherwise is compositionally distinct from the latter. Similarly, the lower Grasberg target Poverty Bush falls within the field for the Burns formation in Fig. 12c, but is distinct from Burns for most elements. Note that Poverty Bush also has a distinctive outcrop texture, showing fine-scale, wavy laminations (Fig. 4e) that are not present on other Grasberg formation outcrops. Finally, the abraded Grasberg target is distinctly different in composition from abraded Burns formation rocks. Compared to abraded Burns formation targets, abraded Grasberg targets have lower MgO and Ni, and higher Cl, FeO and Zn (Fig. 12). The SO_3 content is only ~10 wt% in Grasberg abraded vs. 17.0-28.6 wt% for abraded Burns formation targets.

The relationship between the upper and lower Grasberg units is difficult to ascertain because Grasberg targets scatter considerably on many element-element plots and the fields for the two units overlap (Fig. 12). The scatter could be caused by surface debris, but the analyses do not appear to be significantly influenced by contamination from sand or dust on untreated surfaces. Some elements, such as Mg, are significantly lower for brushed vs. untreated surfaces, which ***could*** be consistent with contamination (Fig. 12). However, the compositions of untreated Grasberg targets cannot be explained as simple mixtures of brushed or abraded targets and surface contamination of dust or soil. This aspect is discussed in more detail in Section 5.2. Excluding the two abraded targets, the averages of the lower and upper targets cannot be distinguished; only the ratio of Na_2O is outside its uncertainty limit (Table 3). Although upper Grasberg is lighter in tone than lower Grasberg, this difference is not reflective of composition as determined for untreated surfaces. Note however, that the Grasberg formation is compositionally heterogeneous and only five analyses are averaged for each unit (Table 3). For these reasons, the averages are not tightly constrained.

The MER team commanded a sequence of target offsets, RAT treatments and APXS analyses for the upper unit target Grasberg in order to gain better knowledge of the true composition of the formation. Of particular importance are the differences between the abraded target and the untreated and brushed targets. Grasberg was a dusty rock surface and brushing resulted in a significant decrease in MgO and increase in Cl in the Grasberg1 target (Figs. 12b, d, e). Because of microtopography on the target surface, the abraded target still contains a substantial fraction of unabraded surface that is below the plane of abrasion (Fig. 5a), but brushing appears to have cleaned the loose debris out of the remaining depressions. Figure 13 shows the untreated and brushed Grasberg1 targets normalized to the abraded target for all elements. On this diagram, elements with ratios >1 had their concentrations lowered by abrasion. Of the major elements – here defined as those with concentrations ≥2 wt% – Na_2O, SiO_2, CaO and FeO were little-affected by the abrasion, suggesting that untreated, wind-cleaned surfaces faithfully record the true compositions for these elements. Magnesia and Al_2O_3 are much lower in the abraded target, while SO_3 and Cl are much higher. For these elements, the true composition of the Grasberg formation might not be well constrained.

A final observation concerns two targets, Monjon Purple and Monjon Grey. Most of the rock has the typical purple color of the Grasberg formation in Pancam false-color images but a small fraction is greyish in this rendition (Fig. 4c). Based on shadowing in the scene, the grey material appears to be a surficial coating or veneer on the rock. The Monjon Grey MI finder frame shows that the APXS target missed the bulk of the grey material (lower box; Fig. 4c), although it does contain more grey material than does Monjon Purple. For many elements, the targets are essentially identical in composition, however, Monjon Grey has roughly twice the MnO content of Monjon Purple; 0.58 vs. 0.27 wt%. There are also lesser enrichments in Ni and Zn, and modest depletions in SO_3 and Br in Monjon Grey. *Farrand et al*. [2016] noted that the grey material on Monjon, also observed in several other Grasberg exposures, had a positive sloping near-infrared spectrum similar to some Mn oxide minerals, which is borne out by the elevated Mn in Monjon Grey.

5.2. Matijevic Formation

There are five main lithic components of the Matijevic formation: matrix; spherules; veneers; thin, bright, anastomosing veins; and boxwork veins. Analyses were done on the matrix, spherule-bearing, veneer-rich and anastomosing-vein-rich materials in flat-lying Matijevic formation outcrops, on spherule-rich, ledge-forming outcrops, and on boxwork veins (Table S2). The compositions of the boxwork veins are discussed by *Clark et al*., [2016], and are not discussed here in detail. In no case did either veneer material or anastomosing-vein material completely fill the APXS field of view, although the Chelmsford3 veneer nearly did (Figs. 7b, c). We can nevertheless infer the compositional characteristics of veneers and anastomosing veins from a series of analyses of different targets. We commanded a series of analyses and surface treatments, but only in the case of the Sandcherry veneer target did we do the full treatment/analysis sequence. Table 1 summarizes the compositional characteristics of the Matijevic matrix, spherule-rich and veneer-rich targets relative to an average of the Shoemaker formation. Table 4 gives the most representative compositions for the different lithologies.

5.2.1. Matrix and Spherule-rich Targets

Our best estimate for the matrix composition is an average of the brushed and abraded Azilda targets weighted by the measurement uncertainty (Table 4). Compared to average Shoemaker formation breccia, the Matijevic formation matrix is very high in SiO_2, P_2O_5 and Ni, and low in K_2O, TiO_2 and SO_3 (Table 1).

The spherule-rich targets consist of dense clusters of several-mm-diameter spherules supported by matrix (Fig. 7d) and thus the compositions of these targets represent mixtures. For the best representation of the spherule-rich composition we use the deeply abraded Sturgeon River3 target on a ledge-forming outcrop (Table 4). This target contains an estimated 40-45% spherules by area [*Arvidson et al.*, 2014]. Compared to average Shoemaker formation breccia, spherule-rich Matijevic targets are very high in SiO_2, high in Ni, low SO_3 and very low in P_2O_5, CaO and TiO_2 (Table 1).

In general, the spherules are not substantially different in composition from the matrix. The ratio of the deeply abraded Sturgeon River3 spherule-rich target to average matrix composition is shown in Fig. 14b. Several elements have higher concentrations in the spherule-rich targets than the matrix – Mg, Cr, Fe and Ni – and several are lower – Na, Al, P, Cl, Ca, Ti, Mn and Br. However, the average matrix is based only on a series of offset measurements of a limited area of one outcrop and the spherule-rich material shown is based on a single target. A considerable fraction of the observed differences between the spherule-rich material and matrix could reflect general compositional variations of the Matijevic formation rather than differences between matrix and spherules. The Fullerton3 target is dominated by matrix, although some spherules are within the field of view of the APXS (Fig. 7a); its composition ought to be dominated by matrix. The element-ratio pattern of Fullerton3 mimics that of Sturgeon River3 in its low abundance ratios for Na, P and Mn (Fig. 14b). The low ratios for these elements in Sturgeon River3 are thus just as likely to be due to higher contents of these elements in the Azilda targets used for normalization relative to typical matrix, as they are to the spherules being poor in these elements. Amongst the major elements ($\geq$2 wt%), only Mg is more than 15% divergent from the matrix composition (gray band in Fig. 14b). Thus, although morphologically distinct, the spherules have compositions that are not greatly different from that of the matrix. This compositional similarity is quite different from the case of hematitic concretions (a.k.a. blueberries) found in the Burns formation, which are very different in composition from the host rock (e.g., *Clark et al*. [2005]; *Rieder et al*. [2004]; *Yen et al*. [2005]).

5.2.2. Veneers

The veneers are thin patches on outcrop surfaces (Figs. 6a, 7c), but not too thin for reliable APXS measurement. For the Sandcherry veneer target, we analyzed the target untreated, brushed and abraded (Table S2). The abrasion removed a portion of the veneer, exposing additional underlying matrix in the APXS field of view, but did not abrade the underlying bedrock. The outcrop surface was slightly angled with respect to the grind plane, and had a small amount of relief. This resulted in a beveled abrasion surface with an abrasion depth of 0.8 mm. Even given the uncertainties regarding the angle of the abrasion plane, the thickness of the veneer is on the order of the abrasion depth. This is effectively an infinitely thick target for the APXS instrument for all elements (cf., *Rieder et al.* [2003], Section 6.3].

Amongst the veneer-rich targets, the Sandcherry untreated and brushed targets show the greatest compositional differences from the average matrix; we use the brushed target as the best indicator of this veneer material (Table 4). We brushed the Chelmsford veneer-rich target and did two measurements of it, one slightly offset from the other; we include an average of these two analyses in Table 4. Veneers – a.k.a. coatings – are present in the locality of the boxwork alteration veins and APXS targets there included varying amounts of veneer [*Clark et al*., 2016]. Those authors derived an estimate of the veneer composition by deconvolving the compositions of the set of analyses; their estimate of the veneer is given in Table 4.

The veneer-rich targets have clear compositional distinctions from the matrix (Table 4). The veneer is richer in volatile/mobile elements S, Cl, Zn and Br than the matrix by factors >2.8 times for Sandcherry (Fig. 14a) indicating that these elements were substantially mobilized by the process that formed the veneer. The Chelmsford veneer shows lesser enrichments in these volatile/mobile elements - ~1.7-2.3 times – but has an enhancement in MnO not seen in the Sandcherry targets (Fig. 14a). Veneer-rich targets have small enrichments (~25%) in K and Ca, and small depletions (10-20%) in Na, Al, Si and P compared to matrix. The calculated veneer (coating) composition from *Clark et al*. [2016] shows essentially the same compositional trends – large enrichments in S, Cl, Zn and Br, with smaller enrichments in K and Ca (Fig. 14a).

The two veneer-rich targets discussed here show variations in composition, most likely due to variations of the amount of veneer material within the APXS field of view. (Because of the attitude of the analyzed surface with respect to the rover, the APXS placement might not have been co-registered with the center of the MI mosaics. This misalignment precludes accurate determination of the fraction of the veneer material within the APXS field of view.) The veneer-rich targets show a general trend of increasing Zn with Cl (Fig. 15e) consistent with analytical mixing of signal from the matrix with that from the veneer. Veneer-rich targets with the highest Cl and Zn contents have the lowest Al_2O_3 (Fig. 15c) and SiO_2 (Fig. 15b) contents, indicating the veneers are not enriched in aluminosilicates such as clay minerals. The calculated coating composition of *Clark et al*. [2016] is also low in Al_2O_3 and SiO_2, and high in S, Cl, Zn and Br (Table 4). The coating composition was calculated by computing the relative instrument responses from the areal fractions of boxwork vein and coating in the fields of view of two of the measurements, and extrapolating to 0% areal coverages to calculate the two components; there is greater uncertainty in the computed coating composition, but this is not quantified [*Clark et al*., 2016].

5.2.3. Anastomosing Veins

Amongst the anastomosing-vein-rich targets, Ortiz2B has the highest SO_3 and CaO contents. We use that targets as the best indicator of the composition of the veins. The Ortiz2B vein-rich target is richer in S, Cl, Ca, Mn and Br than the matrix. For most other major elements, Ortiz2B has abundance ratios of ~0.83. This pattern is generally consistent with the Ortiz2B analysis having two components, ~17% vein dominated by Ca-sulfate and ~83% matrix. The thin, feathery bright Ortiz veins have general compositional similarities to the wide veins in the Grasberg formation. Vein-rich targets are discussed in detail in Section 5.4.

5.2.4. Comparisons to Burns and Grasberg Formations

In general, the Matijevic formation is compositionally distinct from the Burns and Grasberg formations. Amongst the elements shown in Figure 15, Matijevic rocks have generally higher contents of MgO, Al_2O_3, and Ni, but have lower contents of FeO and Zn compared to Grasberg rocks. Excluding the veneer-rich targets, Matijevic rocks also have lower Cl contents than do Grasberg rocks. Similarly, Matijevic formation rocks have higher Al_2O_3 and Ni but lower Zn contents than Burns formation rocks (Fig. 15). Compared to the Grasberg formation, and especially the Burns formation, Matijevic formation rocks have lower SO_3 contents. However, for many other elements, the composition of the Matijevic formation overlaps the ranges for the Burns and/or Grasberg formations.

To examine possible compositional similarities between these three formations more rigorously, we did Agglomerative Hierarchical Cluster Analysis (AHCA) on the rocks. This is a multivariate technique that groups observations (APXS targets) by similarities in variables (element concentrations). For our analysis, we used element/Si mole ratios as the variables to minimize problems associated with closure restraint caused by normalizing the APXS data to sum to 100% [*Chayes*, 1971]. We excluded vein-rich targets from the analysis. We wish to compare the rock target compositions and including the vein-rich samples would return clusters biased by the distinctive vein compositions (e.g., Figs. 12a, 14a). We did include the Matijevic formation veneer-rich targets in order to evaluate their similarity/dissimilarity to the other lithologies. We also included dark-sand and bright-soil targets presented in the on-line supplementary material (Table S5) to help evaluate the possible effects these materials might have on the compositions of untreated surfaces. We ran two calculations; one using all elements and one excluding the volatile/mobile elements S, Cl, Zn and Br. We forced the calculation to return five clusters in order to obtain finer granularity on the results. Clusters can easily be merged at higher levels by inspection of dendrograms to yield geologically interpretable results. The resulting dendrograms are given in Figure 16.

Using all elements in the AHCA calculation, the highest (most dissimilar) clustering level separates clusters 1-3 from 4 and 5 (Fig. 16a). Clusters 1 through 3 are composed of Burns formation targets, the compositionally anomalous Grasberg formation target Poverty Bush (Fig. 12) and two veneer-rich Matijevic formation targets. Poverty Bush also has an unusual texture compared to other Grasberg formation outcrops (Fig. 4e). The two veneer-rich targets are the untreated and brushed Sandcherry analyses that have the clearest compositional signature of the veneer. Cluster 4 includes all the other Matijevic formation targets, the Burns-margin target Dibbler, and all the dark-sand and bright-soil targets. With the exception of the two Sandcherry targets, the other Matijevic formation targets cluster at a low level of dissimilarity (cluster 4), shown in more detail in Fig. 16b. Cluster 4 has two main subclusters. One (left side of Fig. 16b) contains mostly dark sand, bright soil and the remaining veneer-rich Matijevic targets. The Burns-margin target Dibbler is most similar in composition to the soils (Fig. 16b), as is also evident in Fig. 12. The Dibbler target consisted of soil and dark, rounded-pebble debris on top of a Burns formation outcrop pavement and its inclusion in cluster 4 reflects this rather than compositional similarity with the Matijevic formation. The other subcluster (right side of Fig. 16b) contains all but one of the matrix targets and all of the spherule-rich targets, confirming that the spherules are not greatly different in composition from the matrix. The Matijevic formation is well-resolved from the Burns formation, joining clusters 1-3 at the highest level of dissimilarity. Cluster 5 is composed solely of Grasberg formation rocks, which are compositionally more similar to the Matijevic formation (cluster 4) than to the Burns formation.

The Burns formation is composed of sulfate-rich sandstones that resulted from basaltic materials weathered by S-rich fluids [*McLennan et al*., 2005; *Squyres and Knoll*, 2005] and has a generally higher SO_3 content than the Grasberg or Matijevic formations. Further, untreated Burns targets have lower SO_3 contents than do abraded targets [*Rieder et al*., 2005] indicating preferential loss or obscuring of SO_3 once bedrock is exposed. Variations in halogens and Zn on rock and soil surfaces, as demonstrated by comparison of untreated, brushed and abraded rock targets and indurated soils in Gusev Crater, shows that they are mobile even in under low water/rock conditions [*Gellert et al*., 2004; *Haskin et al*., 2005; *McSween et al*., 2004]. This could have happened in the recent times in the current martian environment, or much earlier, perhaps ~3 Gyr ago. We thus ran the AHCA excluding these volatile/mobile elements to minimize the effects that environmental process would have on the results (Fig. 16c). In this calculation, the distance metric is roughly half that of when the mobile/volatile elements are included, which is consistent with the latter representing a significant component of the compositional variation.

As in the previous case, in the calculation sans volatile/mobile elements, the Burns formation dominates clusters 1-3, the Matijevic formation dominates cluster 4, and the Grasberg formation dominates cluster 5. However, the structure of linkages is significantly different; the Grasberg is most dissimilar from all other rock units, while the Matijevic formation is more similar to the Burns formation than to the Grasberg. This structure indicates a general compositional similarity between what might be called the “basaltic” component of the Burns and Matijevic formations. All Matijevic veneer-rich targets cluster with Burns formation targets, including those that cluster with the matrix and spherule-rich targets when all elements are used. Cluster 4 now consists of matrix and spherule-rich Matijevic targets (Fig. 16d) plus one dark sand (the same one in the right subcluster of Fig. 16b). All of the Grasberg formation targets are now collected in cluster 5, including Poverty Bush, which clusters with the Burns formation when all elements are used. Cluster 5 includes six Burns-formation targets; one is the Burns-margin target Callitris but the other five are from widely dispersed locations on Meridiani Planum. Thus the compositions of the Grasberg and Burns formations are distinct.

Earlier we remarked that we found no evidence suggesting that the untreated Grasberg targets had their compositions compromised by sand or dust surface contaminants. This is aptly demonstrated by the AHCA results. The untreated, brushed and abraded Grasberg targets strongly cluster in both dendrograms (Figs. 16a, c), and are moderately dissimilar from the soils included in the calculation.

5.3. Shoemaker Formation

Polymict-impact breccias are chaotic mixtures of the various lithologies excavated by the impact. We undertook compositional investigations of the Shoemaker formation to understand the broad compositional characteristics of the pre-impact terrane, and to identify the compositional effects of alteration processes that were documented in CRISM spectra [*Fox et al*., 2016; *Noe Dobrea et al*., 2012; *Wray et al*., 2009]. We did 72 analyses of Shoemaker formation targets, half from Cape York and half from Murray Ridge/Cape Tribulation (Table S2). Targets analyzed include a limited number of vein-rich targets from two locations and a series of 9 analyses of mineralization deposits on surfaces of two rocks at the Cook Haven location. These two rocks had been overturned by the rover wheels. The results on these latter are given in *Arvidson et al*. [2016] and are only briefly discussed here. The vein-rich targets are discussed separately in the next section. The compositions of some Shoemaker formation rocks were discussed in *Arvidson et al*. [2014, 2015], *Crumpler et al*. [2015a] and *Squyres et al*. [2012].

5.3.1. Shoemaker Formation Compositional Diversity

The Shoemaker formation rocks are generally distinct in composition from the Burns, Grasberg and Matijevic formations although there is some overlap in compositional space. In CaO vs. MgO, SO_3 vs. SiO_2, Al_2O_3 vs. FeO and Zn vs. Ni the Shoemaker formation rocks are largely, but not completely, distinguishable from the other formations (Fig. 17a, b, c, f).

The Shoemaker formation has been divided into three informal members on Cape York (Section 4.3). From stratigraphically lowest to highest they are the Copper Cliff, Chester Lake and Greeley Haven members [*Crumpler et al*., 2015a]. The rock Tisdale is distinct in texture and composition from other Chester Lake member targets. The targets on Cape Tribulation are divided here into three groups by location, two from Murray Ridge and a third from the Hueytown fracture zone. The discussion that follows utilizes these groupings. Table 5 gives the average compositions of Shoemaker formation units and the Shoemaker formation in toto. Two compositionally anomalous targets – Spinifex and Sledge Island – were excluded from the Murray Ridge north averages. These and the Tisdale targets were excluded from the Shoemaker formation average. Table 1 gives the compositional characteristics of individual Shoemaker units relative to the formation as a whole.

The Shoemaker is much more varied in composition than the three formations previously discussed. This variability is especially evident in the SO_3, FeO, Ni and Zn contents (Figs. 17b, c, f). These variations have both geographic and stratigraphic components. Geographic variation is illustrated by comparing rocks from Murray Ridge with those from Cape York. The former generally have lower Ni and Zn contents than the latter, for example (Fig. 17f). Stratigraphic variations are illustrated by the three Cape York members, which generally increase in FeO in the sequence Copper Cliff, Greeley Haven, Chester Lake (Fig. 17c).

The ejecta block Tisdale, from the small crater Odyssey at Spirit Point (Fig. 1b), is part of the Chester Lake member [*Crumpler et al*., 2015a], but it has clear differences in composition from other Shoemaker formation rocks. It has lower MgO and higher Ni and Zn compared to other rocks of the Chester Lake member (Figs. 17a, d-f). Most analyses of the Tisdale block are higher in P_2O_5, Ni, Zn and Br, but not SO_3 or Cl, compared to other Chester Lake member targets, or the Shoemaker formation more generally. The P_2O_5, Ni, Zn and Br contents of Tisdale include the highest measurements on the Endeavour Crater rim. As noted in Section 4.3, the Copper Cliff member contains spherules as does the underlying Matijevic formation. Copper Cliff targets commonly overlap the field for Matijevic formation targets in Fig. 17; we will explore this in more detail in Section 6.1.

5.3.2. Shoemaker Formation Heterogeneity; Clast-Matrix Comparisons and Outcrop-scale Variations

Clasts in polymict-impact breccias are mostly fragments of the pre-impact lithologies, whereas the matrix is a mixture of materials. To gain a clearer picture of the lithologic diversity of the Shoemaker formation, we have done paired analyses of host and clast-rich targets at four locations, two on each rim segment, and we did an extensive set of offset measurements of the Greeley Haven outcrop in the area of one of the host-clast pairs on Cape York. The host targets included a higher fraction of matrix, but are not pure matrix samples. Similarly, the clast-rich targets were centered on clasts, but have varying amounts of matrix in the field of view depending on the size of the targeted clast. The results of these measurements are shown in Figs. 18 and 19. Note that clasts in Shoemaker formation breccias are compositionally distinct from Matijevic formation matrix and spherule-rich rocks (Fig. 19). Although the Matijevic formation represent some portion of the pre-impact target terrane, none of the clasts analyzed are derived from this formation.

There are some commonalities in compositional differences between clasts and host, but no systematic differences that are always observed. For example, the Geluk/Salisbury, Mount Tempest/Tangalooma and Sarcobatus Clast/Sarcobatus Flat pairs all show higher Al_2O_3 and CaO in clasts than hosts, but the Komati/Boesmanskop pair does not (Figs. 18b, 19a). All clasts show resolvable enhancements in Mn, have lower Fe/Mn and higher Al/Mg compared to hosts. For the Geluk and Sarcobatus Clast targets, lowering of Fe/Mn is significantly contributed to by lower FeO compared to the host (Fig. 19c). The Komati/Boesmanskop clast/host pair is from the Greeley Haven outcrop block that was investigated as a series of 12 Amboy targets over the fourth winter. The variation in composition observed for the Amboy targets encompasses the range of variation observed for the Komati/Boesmanskop pair (Fig. 18b). These clast/host and Amboy series observations are consistent with the inference based on textures that Shoemaker formation rocks are heterogeneous polymict breccias composed of materials from different protoliths.

The compositional variations do not solely result from differences between clasts and matrix. We did Agglomerative Hierarchical Cluster Analysis on Greeley Haven member rocks - the Greeley Haven outcrop plus Transvaal located about 10 m away – and the dark-sand and bright-soil targets (Table S5). We did the analysis using all elements and again excluding the volatile/mobile elements. The results of the two calculations are essentially identical; we show the results of the first calculation in Fig. 20a. Three compositional clusters result. Cluster 1 is composed of Amboy 4 through 12, the Transvaal target and all but one of the soil targets. Cluster 2 is composed of Amboy 1 through 3, Boesmanskop (untreated and brushed) and the Komati clast. Cluster 3 consists of one dark-sand target (Fig. 20a), Auk, whose composition is consistent with having the highest plagioclase and lowest ferromagnesian-phases components amongst the dark sand targets (Table S5). Cluster-1 targets occupy a distinct sub-region of the Greeley Haven outcrop (Fig. 20b) suggesting a possible zone of compositionally distinctive material within the larger outcrop. The Pancam false-color image shows that the outcrop is generally less dusty in the region of the cluster-2 targets (Fig. 20b). The MI images also show more uniform surfaces for the cluster-2 targets (Fig. 20c) compared to the cluster-1 targets (Figs. 20d, e).

One possible explanation for the distinct compositional clusters returned by the AHCA is that surface litter on the cluster-1 targets masks the outcrop composition. We think this is unlikely to be the entire story for the following reasons. Much of the debris on the cluster-1 target surfaces is lithic fragments that are most likely locally derived (Figs. 20d, e). These lithic fragments would have the same composition as the outcrop. Some fine-grained sand is visible in the MI images and the Pancam image (Fig. 20b) indicates that dust is also present. However, the compositional distinctions between clusters 1 and 2 are not consistent with contamination by aeolian sand and/or airfall dust. Cluster-1 targets overlap the fields for dark sand and bright soil in MgO vs. Al_2O_3 and CaO vs. Al_2O_3 (Figs. 19a, b), which could suggest the soils dominate the compositions of some cluster-1 rocks. However, cluster 1 overlaps cluster 2 in Zn vs. Cl but not the soils, and cluster 1 extends from cluster 2 in FeO vs. MnO towards high MnO content and away from the soils (Figs. 19c, d). Dark sand and bright soil are members of cluster 1 (Fig. 20a), but we think this likely reflects a general similarity between these materials and the Shoemaker formation breccias rather than sand/dust completely masking of outcrop compositions. We conclude that while aeolian sand and airfall dust obscure to some extent the true rock compositions, the differences in composition between clusters 1 and 2 are in part due to the rocks themselves. This indicates that the polymict breccias include multi-decimeter-scale heterogeneities caused by differences in compositions of “packets” of impact debris deposited on the rim.

5.4. Vein-rich Targets

Crosscutting veins contained within outcrops document late additions of volatile/mobile elements resulting from alteration of preexisting rocks. The compositions and mineralogies of veins provide evidence constraining the nature of the alteration processes. We analyzed vein-rich targets in the Grasberg, Matijevic and Shoemaker formation rocks in order to understand the types of alteration that occurred around the Endeavour Crater rim (Table S2; Fig. 21). The

Shoemaker formation targets are from Murray Ridge/Cape Tribulation whereas the others are from Cape York.

5.4.1. $CaSO_4$-dominated Veins

We previously noted that the compositions of the coarse veins in the Grasberg formation are consistent with $CaSO_4$ [*Squyres et al*., 2012]. This is illustrated in Fig. 21a which shows that a mixing line between the composition of Deadwood, host of the Homestake vein, and $CaSO_4$ passes through the compositions of the coarse vein targets. These targets did not completely fill the APXS field of view and some of the host rock plus surficial litter contribute to the compositions determined by the instrument. Roughly 45-48% of the instrument response for Homestake2, the target with the highest CaO and SO_3 contents, is derived from the vein, assuming it is pure $CaSO_4$. The veins have distinctive Pancam spectra that show drops in reflectance from 934 to 1009 nm that is consistent with the H_2O overtone absorption in gypsum reflectance spectra [*Farrand et al*., 2013]. The Pancam spectra for the hydrated $CaSO_4$ bassanite would be distinct from that of gypsum in having a much weaker H_2O absorption feature; we concluded that the Homestake vein is not composed of bassanite [*Squyres et al*., 2012].

The veins cutting Shoemaker formation breccias are similarly consistent with being pure $CaSO_4$, and they show the drop in Pancam spectral reflectance from 934 to 1009 nm indicative of gypsum. We commanded three offset measurements of the Bristol Well target to sample an irregular patch of bright vein material, lithic debris and aeolian drift sand (Fig. 22a). As in the previous case, the vein did not fill the field of view of the instrument and the integration centered on the vein includes response from surrounding non-vein materials. The Bristol Well3 target was commanded to be centered on lithic debris and drift sand (Fig. 22b). A mixing line between Bristol Well3 and $CaSO_4$ passes through the other Bristol Well target consistent with a pure Ca-sulfate vein (Fig. 21b). However, the vein material would only make up ~9% of the APXS response signal. Because of this we cannot definitively assign a composition to the vein other than to note that it is dominantly $CaSO_4$. Two offset integrations on the bright vein Cottondale (Fig. 8f) from the Hueytown fracture zone do not form a mixing line between the average Hueytown outcrop composition and $CaSO_4$ (solid line, Fig. 21c). Again, because the vein material did not fill the field of view of the instrument, lithic debris and aeolian drift sand were included in the instrument response. The Cottondale vein target compositions are consistent with a response that includes $CaSO_4$, the average Hueytown outcrop and average dark sand (dotted line, Fig. 21c). The simplest interpretation of the data from vein-rich targets in the Shoemaker formation breccias is that the veins are composed mostly of Ca-sulfate.

In the case of the Matijevic formation, mixing the average matrix composition with Ca-sulfate does not pass through the compositions of the Ortiz targets that contain the anastomosing veins (solid line, Fig. 21d). Regressing the CaO and SO_3 data for the vein-rich targets results in a correlation with one endmember consistent with the average Matijevic formation matrix, but the high CaO-SO_3 endmember would have molar Ca/S < 1, inconsistent with pure $CaSO_4$ (dotted line, Fig. 21d); the vein endmember has excess S compared to pure Ca-sulfate. The Matijevic formation vein-rich targets have decreasing MgO and FeO with increasing CaO (e.g., Fig. 15a) and SO_3, suggesting that the excess S is not due to Mg- or Fe-sulfates. Indeed, with the exception of Ca, none of the cations measured by the APXS are positively correlated with S. One possible conclusion is that the vein-rich material includes one or more unknown S-bearing phases. However, the data could be explained if the anastomosing veins are some mixture of Mg- and/or Fe-sulfates with Ca-sulfate such that as the Ca-sulfate content increases, other sulfates systematically decrease. Nevertheless, the anastomosing veins are dominated by $CaSO_4$. The Ortiz veins show the same drop in reflectance from 934 to 1009 nm in Pancam spectra as observed for the Grasberg veins and we interpret this as evidence for gypsum [*Arvidson et al*., 2014].

Calcium sulfate is only slightly soluble in aqueous solutions and the common presence of $CaSO_4$-rich veins in rocks along the Endeavour Crater rim indicates movement of relatively large volumes of water through the fractures. Calcium sulfate is soluble in solutions from acidic to mildly alkaline (e.g., *Shukla et al*. [2008]), and solubility is modestly enhanced in solutions containing chlorides and other sulfates (e.g., *Azimi and Papangelakis* [2010]; *Azimi et al*. [2007]; *Zhang et al*. [2013]). Solubility of $CaSO_4$ has a maximum in pure water around 30-50°C; the veins likely were formed at moderate temperatures. The identification of gypsum in Ca-sulfate veins in all three formations [*Arvidson et al*., 2014; *Farrand et al*., 2013; this work] indicates temperatures of <50°C [*Nachon et al*., 2014].

5.4.2. Aluminosilicate-dominated Boxwork Veins

In addition to the Ca-S-rich veins, the Matijevic formation hosts bright boxwork veins in some locations [*Arvidson et al*., 2014; *Crumpler et al*., 2015a]. Two targets at one location were analyzed, with one including abrasion to expose the interior [*Clark et al*., 2016]. Unlike the common $CaSO_4$-rich veins on Endeavour Crater rim, the boxwork veins have high Al_2O_3 and the highest SiO_2 measured at Meridiani Planum. The calculated "pure" vein composition is consistent with a mixture dominated by montmorillonite and a silica phase [*Arvidson et al*., 2014; *Clark et al*., 2016]. Pancam spectra of the boxwork veins also display a drop in reflectance from 934 to 1009 nm as seen in the $CaSO_4$-rich veins, but display subtle spectral differences from those veins [*Farrand et al*., 2014]. For the boxwork veins, the silica phase might be hydrated silica as observed by the *Spirit* rover near Home Plate [*Rice et al*., 2010]. *Clark et al*. [2016] suggest that the boxwork veins formed from solutions with pH values that were circumneutral to mildly alkaline. Deposition of aluminosilicates in cm-wide, crosscutting boxwork veins suggests that the solutions were hydrothermal (few hundred C) to allow dissolution of primary feldspar from their source (cf., *Catalano* [2013]) with relatively high water/rock ratios. The differences in alteration conditions inferred for the aluminosilicate boxwork veins and the Ca-sulfate-dominated anastomosing veins in the Matijevic formation indicates that they were distinct events.

5.5. Dark-rock Float and Ejecta

The dark rocks encountered as float on Murray Ridge and as a capping rock on Wdowiak Ridge have an uncertain origin. They potentially could be fragments of a pre-impact lithology, materials formed during the impact (e.g. impact melt), or even a post-impact addition to the region. Compositional data can help constrain their origin and how they fit into the impact and alteration history of the region. Two analyses were done on the dark vesicular float-rock Tick Bush (Figs. 10a, 11a) from the Solander Point region, and two separate dark float-rocks - Augustine (Fig. 10b) and Point Bede (Fig. 11b) - from the McClure-Beverlin Escarpment region (Table S2). These were untreated targets. From Wdowiak Ridge we analyzed a total of four dark rocks. Two of these were untreated, and one brushed. For the remaining rock we did analyses before and after brushing on the main rock, and two slightly offset analyses of a dark flake on the opposite side of that rock. Mount Edgecumbe was found as float off the northeast tip of Wdowiak Ridge, while the others were ejecta blocks from Ulysses crater on the southwestern end (Fig. 1c).

The analysis results are shown in Fig. 23. Table 1 gives the compositional characteristics of the dark rocks relative to the average Shoemaker formation composition. Amongst the dark-rock float targets, Tick Bush is compositionally distinct from any of the major lithologies found on the Endeavour Crater rim. The low MgO and FeO contents, coupled with high Al_2O_3 (Figs. 23a, b) and SiO_2 (not shown) would be consistent with Tick Bush being an evolved mafic volcanic rock, but this origin is not compatible with the high Ni and Zn contents (Figs. 23c, d). Tick Bush also has higher MnO contents than any other rock from the Endeavour rim, excluding the salt-encrusted surfaces of two rocks dislodged by *Opportunity*'s wheels – Pinnacle Island and Stuart Island [*Arvidson et al*., 2016]. We will return to the origin of Tick Bush in Section 6.2.

The two float rocks from the McClure-Beverlin Escarpment have major element compositions that are generally within family of the Shoemaker formation impact breccias although their Al_2O_3 contents are higher than those of the breccias (Fig. 23b). These two rocks plot at the low MgO and low FeO ends of arrays of compositions of Gusev Crater mafic volcanic rocks (Figs. 23a-c). The fine-grained homogeneous textures of the rocks are compatible with a volcanic origin. These two rocks are low in Zn and Cl compared to the Shoemaker formation breccias or the Matijevic formation (Fig. 23d), and again they are similar to the Gusev Crater mafic volcanic rocks in volatile/mobile element contents [*Gellert et al*., 2006; *McSween et al*., 2006a, b, 2008; *Ming et al*., 2006, 2008]. The compositional and textural characteristics of Augustine and Point Bede are consistent with an origin as mafic volcanic rocks.

Rocks from Wdowiak Ridge are compositionally distinct from all other Endeavour rim lithologies (Fig. 23). They typically have a heterogeneously distributed coating of dust on some surfaces (Fig. 10c) that is effectively removed by brushing (Fig. 11c). Comparing the untreated and brushed compositions of the target Lipscomb-Margaret (hereafter, Margaret), the brushing resulted in lowering of the SO_3 and Cl by about 10%, but all other elements are within measurement uncertainty for the two analyses. The only other brushed target is Hoover (Figs. 10c, 11c), and this target is compositionally anomalous compared to all other Wdowiak Ridge targets. It has by far the lowest Na_2O, Al_2O_3, SiO_2 and TiO_2 contents, and highest SO_3, Cl, FeO and Zn contents (e.g., Figs. 23b, d). The high SO_3, Cl and Zn contents suggest that this rock has an altered composition. The planar fractures [*Arvidson et al*., 2015] that result in dark flakes on flat surfaces after physical weathering (Fig. 11c) are evidence for late alteration of the dark cap rocks prior to impact excavation and deposition in the ejecta field of Ulysses crater. The flake target Lipscomb-Victory (hereafter, Victory) is smaller than the APXS field of view and thus the underlying Margaret substrate contributed to the instrument response. We did two integrations on Victory that were slightly offset, but the two compositions are almost identical. Compared to the Margaret brushed target, the Victory flake targets have ~50% higher Cl contents, and ~18% lower MnO and ~55% lower Ni contents. A small decrease in Al_2O_3 and a small increase in FeO are also evident in the analyses, but these could simply reflect small variations in the Margaret rock composition rather than differences between the flakes and the rock. The change from Margaret to Victory are shown by dashed arrows in Figs. 23b-d.

Compositional variations between Margaret and Victory are unlike the differences between Hoover and the other Wdowiak Ridge rocks indicating that the alteration that we infer occurred along the planar fractures in these rocks was not the same alteration that engendered the Hoover composition. There are general increases in SO_3 and Zn with Cl amongst the Wdowiak Ridge rocks indicating that the suite likely represents a series of variably altered rocks of broadly mafic composition.

6. Discussion

The geological, textural, mineralogical and compositional evidence presented is used below to explore several aspects of the nature and origin of the lithologies seen in the Endeavour Crater rim: (i) the nature of the pre-impact surface; (ii) which rocks, if any, are pristine; (iii) which are altered; (iv) the origin of the dark rocks; (v) formation of veneers; and (vi) the origin of the Grasberg formation. The discussion ends with a scenario developed to explain the geological and alteration history of rocks on the rim of Endeavour Crater.

6.1. Nature of the Pre-impact Terrane

As discussed in Sections 4 and 5, we have several types of materials whose textures and compositions can inform us of the lithologic diversity of the pre-impact terrane: the Matijevic formation, clasts within the Shoemaker formation breccias, and dark rocks from Murray and Wdowiak Ridges. The latter are discussed in Section 6.4. Interpretations of the former two are explored in this section.

The Matijevic formation is interpreted as representing a pre-impact lithology upon which the polymict impact breccias of the Shoemaker formation on Cape York were deposited [*Arvidson et al*., 2014; *Crumpler et al*., 2015a]. The limited areal and stratigraphic extent of the Matijevic formation outcrops hampers interpretation of the origin and scope of the formation. It could be regional or localized in extent [*Crumpler et al*., 2015a], but it is plausible that it is part of the Noachian etched unit of Meridiani Planum (Figs. 2b, c). However, because of uncertainty in the thickness of the etched unit in the location of Endeavour Crater, the Matijevic formation could instead be part of the Noachian subdued crater unit that is exposed to the south of the hematite-spherule lag deposits [*Hynek and Di Achille*, 2017]. Rocks similar to the Matijevic formation have yet to be identified on the Cape Tribulation segment of the rim, but as of the time this paper was accepted, we have not investigated a similar location – the inboard side of the rim – for this segment. The impact process also plausibly resulted in differing degrees of motion of blocks around the rim which would have affected exposures of the pre-impact surface (e.g., *Crumpler et al*. [2015a]; *Grant et al*. [2016]). The Matijevic rocks give us our only definitive direct look at the nature of the pre-impact surface, albeit very limited in geographic extent.

A broader-scale, but fragmented view of the pre-impact terrane can be attained by examining clasts in the Shoemaker formation breccias, informed by knowledge gained from the study of terrestrial craters. Close to the rims of small craters, low-velocity ejecta can form "inverted stratigraphy" in which the local stratigraphic column can be recognized in the ejecta blanket, albeit upside down. However, for larger, complex craters such as Endeavour, the transient crater rim, where low-velocity ejecta would occur, slumps inward forming the inner ring of the final crater. This inner ring and possible preserved inverted stratigraphy is not accessible by *Opportunity*. At the location of the tectonic rim where *Opportunity* has worked, ejecta strikes the surface at high velocity, effectively mixing the ejecta blanket. Material is ejected from a crater only to a depth of about 1/3 the transient crater depth, or approximately 0.1 times the transient crater diameter (see *Melosh* [1989], page 78). The clast suite in the Shoemaker formation thus represents a mixture of the lithologic diversity of the upper portion of the pre-impact geology. Comparison with a terrestrial crater can aid in the interpretation of the Matijevic formation and clast suite.

6.1.1. Ries Crater; a Terrestrial Analog

The Ries Crater is a well-studied Miocene impact crater in southern Germany that is similar in size – 26 km diameter – to Endeavour Crater and thus serves as a useful analog; the discussion here is summarized from *Hörz* [1982], *Hörz et al*. [1983], *Pohl et al*. [1977] and *Stöffler et al*. [2013], except as noted. The pre-impact target of the Ries consisted of 550-750 m of terrestrial and marine sediments overlying a metamorphic/granitic crystalline basement. The surface topography and the unconformity surface each had on the order of 10^2 m of relief.

Two types of polymict breccia occur on the tectonic rim of the Ries, the Bunte Breccia and the outer suevite. The Bunte Breccia is almost exclusively derived from the sedimentary target rocks that are modestly shocked, if at all, whereas the suevite derives predominantly from the crystalline basement and contains shocked rocks and impact melts. Within the Bunte Breccia deposits, blocks >25 m across are classified as megablocks and mapped individually as to stratigraphic source region, while blocks <25 m across are subsumed as part of the Bunte Breccia. The Bunte Breccia is much coarser grained than the suevite and forms the bulk of the continuous ejecta blanket. It is roughly 100 m thick at the tectonic rim (see Fig. 35 of *Hörz et al*. [1983]) and directly overlies the pre-impact surface. The Bunte Breccia is thus *stratigraphically* equivalent to the Shoemaker formation, which formed the continuous ejecta blanket around the Endeavour Crater tectonic rim. Note that the Bunte Breccia is substantially coarser-grained than is the Shoemaker formation at Endeavour. At the position of the tectonic rim of the Ries, the *mean* fragment size of the Bunte Breccia is ~50 cm (using eq. 4 of *Hörz et al*. [1983]), whereas the *largest* clasts we have observed in the Shoemaker formation are ~10 cm across. The instrumentation on-board *Opportunity* does not allow for characterization of shock state of rocks and we cannot thus determine whether Shoemaker formation clasts are of low shock stage as is the case for the Bunte Breccia.

Outer suevite overlies the Bunte Breccia with very sharp contacts and is a finer-grained polymict breccia. The unit is presently discontinuous and is thought to have been emplaced as discontinuous patches, likely of varying thicknesses. The maximum thickness of suevite observed outside the tectonic rim is ~30 m. In some locations, a top quenched zone is present indicating little erosion. The outer suevite was not part of the primary ejecta curtain that deposited the Bunte Breccia but its mode of transportation and emplacement is uncertain. Based on a synthesis of observations and modeling, *Artemieva et al*. [2013] and *Stöffler et al*. [2013] concluded that the outer and crater suevite of the Ries represent polymict fallback deposits from a secondary plume engendered by interaction of volatiles ($H_2O \pm CO_2$) with impact melt and hot breccia on the crater floor. This follows earlier work that concluded that the suevite of the Onaping Formation of the Sudbury impact structure was formed by a melt-fuel-coolant-interaction process rather than as primary ejecta [*Grieve et al*., 2010]. A 20-40 cm thick basal sublayer of the Ries outer suevite – a miniscule fraction of the total suevite – might be fallback breccia from the primary ejecta plume, but this is uncertain [*Stöffler et al*., 2013].

Osinski et al. [2016] have compared the morphologic and petrologic characteristics of Ries suevite with those of volcanic rocks formed by a melt-fuel-coolant-interaction process, and with the Onaping Formation suevite, and concluded that an origin of the Ries suevite as proposed by *Artemieva et al*. [2013] and *Stöffler et al*. [2013] is not supported. *Osinksi et al*. [2016] affirmed an origin for the Onaping suevite as deposits from secondary, phreatomagmatic eruption plumes. However, these authors concluded that the Ries suevite was emplaced as melt-rich flows on the Bunte Breccia. *Osinksi et al*. [2016] documented that emplacement of melt-rich flows on top of continuous ejecta blankets is commonly observed on the inner planets, the Moon and asteroid 4 Vesta.

We earlier noted that Shoemaker formation rocks bear a textural resemblance to suevite [*Crumpler et al*., 2015a; *Squyres et al*., 2012]. Note that because *Opportunity* cannot determine whether glass is present, the textural resemblance cannot extend to the presence of impact-melt, a hallmark of Ries Crater suevite (e.g., *Osinski et al*. [2004]; *Siegert et al*. [2017]). Given that (i) suevite overlies the continuous ejecta blanket at the Ries, (ii) Reis suevite was deposited as discontinuous patches only a few tens of meters thick, (iii) 100-200 m of erosion has occurred on the Endeavour Crater rim [*Grant et al*., 2016], which would have removed any suevite that might initially have been present, and (iv) the Shoemaker formation directly overlies pre-impact rocks, comparison of Shoemaker formation rocks with the Bunte Breccia is more apt.

The lithic clast population in the Bunte Breccia is dominated by sedimentary rocks from the upper 550-750 m of the target stratigraphy and <1% of the clast population is derived from the approximately 800-1000 m of crystalline basement excavated by the impact. As a crude approximation, clasts in the Bunte Breccia are dominantly from the upper ~40% of the target zone. *Melosh* [1989] states (page 144) that a typical result of crater studies is that a transient crater expands by about 60% of its diameter to form the final diameter of a complex crater, and the transient crater diameter is roughly equivalent to the floor diameter of the final crater. This would put the transient crater and final floor diameter for Endeavour at ~14 km. This is consistent with the inner diameter of 17-19 km defined by terrace blocks [*Grant et al*., 2016] which would be somewhat greater than the floor diameter. Material is excavated from a depth of roughly 0.1 times the transient crater diameter, or ~1400 m for Endeavour. However, the depth of Endeavour Crater is estimated to have been 1500-2200 m before infilling with Burns formation sands [*Grant et al*., 2016], which suggests a greater excavation depth than that estimated here. Using a range of excavation depths of 1400-2200 m, and based on the results from the Ries crater, we expect the clasts in the Shoemaker formation to have been derived mostly from the upper 560-880 m of the pre-impact surface.

6.1.2. Matijevic Formation; Origin and Mixing During Impact

None of the clasts in Shoemaker formation breccias resemble pre-impact Matijevic formation rocks. Although there is some overlap in composition for some elements in some clasts with Matijevic rocks, no clasts fall within the fields for the latter for all elements (see Fig. 19). The textures for clasts are also distinct from the Matijevic rocks (compare Figs. 7a, 9c). More generally, clasts are typically dark in Pancam images in contrast to the bright Matijevic formation matrix and are distinct from the Matijevic matrix in terms of their VNIR Pancam spectra. Thus, none of the few clasts we have analyzed are from a Matijevic protolith, and it likely was not a major component of the pre-impact terrane.

Although clasts of Matijevic formation have not been identified within the Shoemaker formation, there is nevertheless evidence for localized contamination of the lowermost Shoemaker formation with material derived from the Matijevic formation. In Section 4.3 we noted that spherules like those found in the Matijevic formation are present in the Copper Cliff member of the Shoemaker formation that lies in direct contact with it. In Section 5.3 we noted that there is some compositional overlap for some elements between the Matijevic and Shoemaker, and that Copper Cliff member rocks commonly overlapped. We ran an AHCA calculation for all Matijevic, Shoemaker and Grasberg formation targets for all elements except the volatile/mobile elements. All of the Matijevic formation matrix and spherule-rich targets but one cluster with six of the nine Copper Cliff member targets. No Grasberg or other Shoemaker formation targets are in this cluster. This indicates a general compositional similarity between the Matijevic formation and the overlying Copper Cliff member. At the Ries crater, emplacement of the Bunte Breccia on the rim caused erosion of the paleosurface and incorporation of the eroded debris into the Bunte Breccia [*Hörz et al*. 1983]. The textural and compositional data from the Cape York rim segment are consistent with this same process occurring locally at Endeavour Crater.

As mentioned in Section 4.2, one possible origin for the Matijevic formation is as volcanic ash [*Crumpler et al*., 2015a]. We can compare this lithology with pristine, ancient Adirondack-class olivine basalts that form the cratered plains of Gusev Crater [*McSween et al*., 2004, 2006; *Morris et al*., 2004, 2006b]. These were analyzed by sister rover *Spirit* using an identical instrument. The cratered plains unit is of Early Hesperian age [*Tanaka et al., 2014*] with an estimated age based on crater counting of 3.65 Ga [*Greeley et al*., 2005; *Parker et al*., 2010]. These are near-primary melts of the martian mantle and are likely representative of basalts that were formed during early martian history [*Filiberto et al*., 2008; *Monders et al*., 2007; *Schmidt and McCoy*, 2010]. Basaltic cobbles (Group 1) with fairly primitive compositions (high MgO) have also been analyzed by the Chemical Camera (ChemCam) instrument on the Mars Science Laboratory rover *Curiosity* in Gale Crater [*Cousin et al*., 2017].

Compared to the abraded interiors of Adirondack-class basalt targets, Matijevic formation matrix and spherule-rich targets are higher in SiO_2 and lower in MgO, CaO and FeO (Fig. 15); all consistent with a more evolved magmatic composition. However, the Ni contents of Matijevic formation rocks are much higher than for Adirondack-class basalts (Fig. 15d); higher Ni coupled with lower MgO is inconsistent with igneous fractionation. The Matijevic formation rocks are similarly lower in MgO and FeO than the primitive Group 1 basalts from Gale Crater, but overlap the latter in SiO_2 and CaO (cf., Table 6, *Cousin et al*. [2017]).

The abraded interiors of Matijevic formation are slightly higher in Cl (~0.5 wt%) and SO_3 (2-3 wt%) compared to the Adirondack-class (0.2-0.3 wt% and ~1.5 wt%), but Zn and Br contents are similar. The veneer-rich targets of the Matijevic formation are substantially enriched in these volatile/mobile elements (Fig. 14a) plausibly as a result of leaching from the matrix and deposition on the surface. Thus, the concentrations of the volatile/mobile elements measured in matrix/spherule-rich targets are likely lower than when the rocks were deposited. Together, the compositional data indicate that the Matijevic formation is composed of altered rocks, but whether alteration occurred prior to or after the Endeavour impact is unclear. If Ni concentrations were enhanced by the alteration, the fine-grained clastic Matijevic formation might have originated as moderately evolved volcanic ash or impact debris from an evolved igneous terrane.

6.1.3. Origin of Clasts

Some clasts appear to be breccias (Fig. 9c), which could suggest that their protolith was an earlier-formed impact breccia, possibly from Miyamoto Crater for example (see Section 3; Fig. 2a). However, polymict-breccia clasts can be formed in a single impact event, and multiple generations of breccia are observed at the Ries (see *Hörz et al*. [1983], page 1681). For this reason, the protoliths for breccia clasts in the Shoemaker formation could have been primary crustal units. More generally, clasts in Shoemaker breccias have textures that indicate that they are very fine-grained or glassy rocks (Figs. 9a, b). Potentially, they are fine-grained primary volcanic rocks.

We have done only a small number of analyses of clasts from the Shoemaker formation, and they do not allow firm conclusions to be drawn regarding the origin of their protoliths. The clast data scatter on major-element diagrams (Fig. 19). This is not surprising as they likely represent material from widely separated locations and depths within the pre-impact terrane. They do not match Adirondack-class basalts in composition, nor are they obvious magmatic progenitors or derivatives from similar basalts. The clasts are also distinct in major element composition from the primitive Group 1 basalts from Gale Crater [*Cousin et al*., 2017]. There is some evidence that the clasts were derived from altered materials. Many of the clasts have FeO/MnO ratios much lower than observed for pristine martian magmatic rocks (Fig. 19c). Igneous processes do not greatly fractionate FeO and MnO, and pristine igneous rocks from Mars, such as the Adirondack-class basalts, have a limited range in FeO/MnO; the Mars line in

Fig. 19c is an average derived from compositions of abraded Adirondack-class-basalt targets. Most of the Shoemaker formation host targets and the dark sands plot along this line, indicating their FeO/MnO ratios are primary. Many of the clasts and some of the Amboy outcrop targets have low ratios as a result of high MnO contents. This indicates likely Mn mobility in the precursor lithologies as a result of alteration of the pre-impact terrane. Manganese mobility is explored in more detail in the next section.

Although definitive conclusions cannot be reached, the textures and compositions of clasts within the Shoemaker formation suggest that they are fragments of mildly altered volcanic units.

6.2. Iron and Mn Variations with Alteration

The geochemical behaviors of Fe and Mn vary greatly depending on oxidation state. Iron and Mn behave very similarly in geochemical systems when in their divalent states. Because of their similar ionic radii, Fe^{2+} and Mn^{2+} are not greatly fractionated by the major ferromagnesian minerals crystallizing from magmas, and igneous rocks from a given planetary body have relatively limited ranges in FeO/MnO [*Papike et al*., 2003]. However, aqueous alteration processes can lead to substantial fractionation of these elements because of differences in solubility with oxidation state and solution chemistry (e.g., *Drever* [1997]; *Lindsay* [1979]; *Stumm and Morgan* [1996]). Fractionation of Mn from Fe in an aqueous environment is demonstrated by Mn-rich dark coatings on surfaces of rocks flipped by *Opportunity*'s wheels in the Cook Haven fracture zone of Murray Ridge [*Arvidson et al*., 2016], and in Mn- rich veins crosscutting Kimberley formation sandstones in Gale Crater [*Lanza et al*., 2016]. The targets in the Cook Haven fracture zone (rock alteration in Fig. 24a; Table 2) have low and widely varying molar Fe/Mn (13.7 – 4.3) caused by increasing MnO content with only modest variation in FeO content. The coatings on these rocks are interpreted as having two main components: an earlier bright coating dominated by Mg-rich sulfates; a later dark, Mn-rich precipitate composed of Mn^{3+} and Mn^{4+} oxide phases [*Arvidson et al*., 2016]. Chemical modeling in which a solution calculated to be in equilibrium with Shoemaker formation composition rock is allowed to precipitate at low T produces a sequence of secondary phases that is consistent with the observations [*Arvidson et al*., 2016]. The physicochemical conditions of this alteration process are poorly constrained at present, but late-stage oxidation to form Mn^{3+} and Mn^{4+} oxide phases is required. Similarly, the Mn-rich veins in Gale Crater are composed of Mn oxides and indicate deposition from highly oxidizing aqueous solutions, which is considered to be evidence for more abundant O in the ancient martian atmosphere than observed today [*Lanza et al*., 2016].

The dark-rock float target Tick Bush has high MnO and low Fe/Mn (10.9 for the higher Mn target) compared to Mars (Fig. 24). (The Mars line shown corresponds to a molar Fe/Mn of 44.9, an average for abraded targets of Early Hesperian Adirondack-class basalts. For comparison, an average Fe/Mn for Late Amazonian martian basaltic meteorites is 36.3 based on compiled literature data.) Tick Bush has lower FeO (13.2-14.0 wt%) compared to the other dark-rock float and Wdowiak Ridge targets (15.2-17.1 wt%, excluding Hoover), but the low Fe/Mn is largely a result of its higher MnO. We did not abrade or brush the surface of Tick Bush, but the composition of this rock is not consistent with dark-sand or bright-soil contamination (Fig. 23), nor does Pancam imaging indicate the presence of a coating (Fig. 10). The high MnO is consistent with enrichment via an alteration process, which could also be the cause of its high Ni and Zn contents (Fig. 23). In particular, the high Ni content associated with low MgO, high Al_2O_3 (Fig. 23) and high SiO_2 in Tick Bush is inconsistent with magmatic fractionation processes and indicates later addition by an alteration process. High Ni contents could result from chondritic contamination (e.g., in an impact-generated rock), but this can be ruled out for Tick Bush because of its association with high MnO and Zn, neither of which would be enriched by chondritic contamination. Note that the SO_3 and Cl contents of Tick Bush are not exceptionally high; they overlap the ranges for dark rock from Wdowiak Ridge that have Mars-like Fe/Mn. Tick Bush is vesicular and very fine grained, possibly glassy (Fig. 11a) indicating a melt origin. Together, the textural and compositional data support an origin as an impact melt of a moderately altered protolith, possibly of evolved volcanic materials. Impact melting plausibly allowed volatilization of SO_3 and Cl, lowering their content and contributing to the vesiculation of the melt.

Figure 24b shows an expanded view of the FeO-MnO relationships for Endeavour rim rocks compared to the Fe/Mn ratio for Mars as represented by abraded Adirondack-class basalts from Gusev Crater analyzed by sister rover *Spirit* [*McSween et al*., 2004, 2006]. With the exception of the Monjon Grey target, the Grasberg formation is high in Fe/Mn, low in MnO and high in FeO compared to the average Shoemaker formation breccia (Table 1). As discussed in Section 5.1, the grey material on Monjon appears to be a coating, with only a portion of the APXS field of view of the Monjon Grey target including this coating. The high MnO content of Monjon Grey is accompanied by the highest Zn content of any Grasberg formation target, and the two Monjon targets have the lowest CaO contents (Fig. 12). The halogen, SO_3 and P_2O_5 contents of Monjon are not dramatically different between the Grey and Purple targets, which are similar to those of most Grasberg formation targets. However, Pancam spectra of these grey coatings are distinct from purple Grasberg targets and are consistent with some fraction of the coating consisting of Mn-oxides [*Farrand et al*., 2016]. Thus, the grey material on Monjon could be an oxide coating rich in MnO similar to those seen at Cook Haven, but we have insufficient data to test this hypothesis further.

There is a dichotomy in Fe/Mn ratios of the Shoemaker formation on the two Endeavour rim segments investigated; rocks on Murray Ridge tend to have Mars-like or higher Fe/Mn while those on Cape York tend to have Mars-like or lower Fe/Mn (Fig. 24b). Separate fields for the anomalous Tisdale block and Shoemaker formation members on Cape York are shown, and compositionally anomalous and clast targets are plotted separately. Two bulk-rock targets, Amboy12 (Greeley Haven, Cape York) and Spinifex (Murray Ridge) have high MnO, but have FeO typical of other rocks from those regions. Clast samples Geluk and Komati similarly have modestly higher MnO, but only marginally higher than some of the Greeley Haven cluster 2 rocks; in the case of Geluk, it has substantially lower FeO compared to its host breccia (cf., Fig. 19c).

We did a series of three measurements of the Murray Ridge Sarcobatus target, a bulk sample and two integrations on a large clast (Fig. 8e), the second of which was better-centered on the clast. For most elements, there is a progression from either low to high contents (Al_2O_3,

SiO_2, P_2O_5, CaO, TiO_2), high to low (MgO, SO_3, Cl, Cr_2O_3, FeO, Br) or roughly constant within measurement precision (Na_2O, K_2O, Ni) (cf., Fig. 18d, 19). This is consistent with the Clast2 target representing the purer sampling of clast material than the first clast target. However, MnO and Zn are exceptions; they are much higher in the first clast target than either the host or Clast2, which are almost identical (Fig. 18d). Sarcobatus Clast has internal variations in MnO and Zn that suggest alteration mobilized these elements. The clast appears fine-grained and homogeneous in Pancam (Fig. 8e) and MI imaging, with no coatings evident. The data and observations are consistent with the alteration having occurred in the protolith of the clast prior to impact excavation.

6.3. Sulfur and Fe/Mn Relationships

We have previously noted a correlation between the S contents and Fe/Mn ratios for rocks from the Endeavour Crater rim that we concluded provided evidence for differential mobilization of Fe and Mn in S-bearing solutions [*Ming et al*., 2015]. In general, data for coarse $CaSO_4$ veins (Grasberg formation) or targets containing finer-scale $CaSO_4$ veins (Hueytown vein, Murray Ridge vein-rich) have Fe/Mn that are Mars-like (Fig. 24b). An exception is the Matijevic formation vein-rich targets, which have Fe/Mn ratios that are lower than the Mars igneous and Matijevic-formation-matrix-target ratios. The relationship between S mobilization and Fe/Mn variation is explored in Fig. 25. As discussed in Section 5.4, the sulfate veins in the Grasberg formation, Bristol Well on Murray Ridge and Cottondale at the Hueytown fracture zone are consistent with being composed of $CaSO_4$, but the Ortiz veins in Matijevic formation are inconsistent with simply being $CaSO_4$ crosscutting typical Matijevic formation matrix rock. A curious characteristic of the vein-rich targets, excluding the Ortiz veins, is that their compositions closely approach the Mars Fe/Mn ratio even though the host rocks might have a distinctly different ratios (Fig. 25a). The difference for the Bristol Well vein on Murray Ridge is small, but the host is already close to the Mars Fe/Mn ratio. For the vein sampled at the Hueytown fracture zone, the Fe/Mn ratio is higher than that of the modeled bedrock-dark sand mixed composition that is plausible for the substrate hosting the vein (Fig. 21c). The largest difference is for the Deadwood-Homestake host-vein pair from the Grasberg formation (Fig. 25a). The CaO and SO_3 data are consistent with $CaSO_4$ contributing ~45-48% of the instrument response for Homestake2 compared to an assumed substrate equivalent to Deadwood.

For the Deadwood-Homestake host-vein pair, the Mn/Si ratio of the host and vein are very similar (Fig. 26a) indicating that the Grasberg formation substrate included in the Homestake analysis field of view has the same Mn/Si ratio as the nearby Deadwood target, and the lower member of the Grasberg formation more generally. (This assumes that the Homestake vein is free of Si and Mn.) In contrast, the Homestake targets have substantially lower Fe/Si than does Deadwood, or any of the targets of the lower member of the Grasberg formation. The substrate included in the APXS field of view is depleted in FeO compared to the Grasberg formation and indicates that FeO was mobilized by the solutions responsible for the veins, but MnO was not. Although the signal is less clear for the other vein-rich targets because of the lower fraction of vein material in the APXS field of view, the Bristol Well vein similarly shows little difference in Mn/Si and lower Fe/Si whereas the Hueytown fracture zone vein shows lower ratios for both, with a proportionally greater decrease in Mn/Si (Fig. 26). The Ortiz veins in the Matijevic formation are the oddballs, showing essentially no difference in Fe/Si but a large increase in Mn/Si. We noted in Section 5.4 that the Ortiz veins are compositionally distinct from the other Ca-sulfate veins we have analyzed.

As noted in Section 6.2, Fe and Mn behave nearly identically in basaltic magma systems, but they can be quantitatively fractionated in some aqueous systems. Mildly acidic to circumneutral solutions at low a_{O_2} can precipitate Fe as oxides/hydroxides while Mn^{2+} remains in solution (see *Stumm and Morgan* [1996], Fig. 7.7). Varying the redox condition is a candidate mechanism for Mn mobilization, but we cannot rule out mobilization by changes in pH. Our hypothesis is that oxidized solutions from the overlying Burns formation interacted with Grasberg formation sediments leading to redox exchange of Fe and Mn. Initially immobile, oxidized Mn was mobilized via reduction by late stage fluxes of Fe^{2+}-rich fluids through the Grasberg sediments via the reaction:

$$MnO_2 + 2Fe^{2+} + 4H_2O \rightarrow Mn^{2+} + 2Fe(OH)_3 + 2H^+$$

This reaction produces acidity similar to that calculated by *Hurowitz et al*. [2010] for interaction of groundwaters with basaltic rock as a mechanism for formation of jarosite and other sulfates in the Burns formation. Regional groundwater upwelling, possibly with recharge from the southern highlands [*Andrews-Hanna et al*., 2007, 2011] might have been a source for the water. This process could have depleted the Grasberg formation in Mn and slightly elevated it in Fe. Fluids that precipitated $CaSO_4$ differentially mobilized FeO from MnO in the vicinity of the veins.

Enrichments of Mn are associated with S. This is suggested by the Fe/Mn and S relationships shown in Figs. 24 and 25 for the Matijevic formation veneers and Ortiz veins, and by the rock alteration targets discussed by *Arvidson et al*. [2016]. This relationship suggests that Mn^{2+} and possibly other ions (e.g., Ni^{2+}, [*Ming et al*., 2015]) were transported with S-rich fluids through fractures and porous substrates in Endeavour Crater rim materials. Manganese, S, and other ions such as Ni precipitated in veins (e.g., Matijevic formation veins) and on other surfaces that came into contact with the fluids. Redox reactions appeared to have played a role in the mobilization and transportation of redox sensitive elements in Endeavour Crater rim deposits. These reactions are likely late-stage diagenetic processes.

6.4. Origin of Dark Rocks

We have already touched upon the compositional characteristics of some of the dark rocks that relate to evidence for alteration. Here we will summarize the compositional and textural evidence and discuss possible origins for these rocks. Dark rocks were encountered on Solander Point, near Cook Haven on Murray Ridge and on Wdowiak Ridge. The reasons for these concentrated occurrences of dark rocks are unresolved. Those on Solander Point and Murray Ridge could be examples of inverted topography [*Crumpler et al*., 2015b], or perhaps remnants of breccia lenses rich in exceptionally large clasts. Several possible origins for the dark rocks capping Wdowiak Ridge have been put forth: (i) impact melt emplaced with ejecta during formation of Endeavour Crater [*Grant et al*., 2015], (ii) an exhumed mega-block of target rock [*Mittlefehldt et al*., 2015], (iii) relief on the pre-impact surface [*Mittlefehldt et al*., 2015], (iv) an upraised fault block created during impact [*Crumpler et al*., 2015b], or (v) inverted topography of resistant rock of former valley-fill materials remaining after erosion of less competent rock [*Crumpler et al*., 2015b]. Wdowiak Ridge is one of several structural elements in the Murray Ridge-Cape Tribulation area with a general NE-SW strike that includes topographic breaks within the bounding rim segments; these might have been engendered by the Endeavour impact [*Crumpler et al*., 2015a; *Grant et al*., 2016]. If so, this would suggest that mechanisms (ii), (iii) and (v) are less likely because that would suggest coincidental alignment of Wdowiak Ridge with impact-generated structures.

The dark rocks from these three locations share a common aphanitic texture, and some are vesicular. As discussed in Sections 5.5 and 6.2, Tick Bush is compositionally distinct from the other dark-rock targets and we interpret it to be an impact-melt rock. It is the only dark rock target from Solander point analyzed using the APXS. If Tick Bush is representative of those rocks, then the scattering of dark rocks on Solander Point (Fig. 3a) plausibly represents a broken-up remnant of an impact-melt lens in the rim ejecta.

The dark rocks from the McClure-Beverlin Escarpment region (Fig. 3b) of Murray Ridge – Augustine and Point Bede – have compositions consistent with their being mafic volcanic rocks. They are distinct in composition from the erratic block Bounce Rock that is a close match to some of the martian basaltic meteorites [*Zipfel et al*., 2011]. Thus, Augustine and Point Bede are not sourced from the same location as Bounce Rock. These two dark rocks are closest in composition to some of the brushed targets on Adirondack-class olivine basalts from Gusev Crater [*McSween et al*., 2006], but are not identical to them. Augustine and Point Bede have generally low SO_3, Cl, Zn and Br contents (see Fig. 23d); Zn and Br are within range of abraded targets on Adirondack-class basalts; SO_3 and Cl are higher. Their Fe/Mn is higher than the typical Mars value (Fig. 24b). These data indicate that they are modestly altered, plausibly as a result of mild weathering. The compositional data for Augustine and Point Bede do not allow for a firm conclusion regarding a volcanic versus impact-melt origin for them, but the simplest interpretation is that they are weathered mafic volcanic rocks.

Wdowiak Ridge rocks have compositions that are very distinct from the Shoemaker formation (Fig. 23; Table 1). Hoover from Wdowiak Ridge is compositionally distinct from the other dark rocks on the ridge, and we conclude that it is substantially altered (see Section 5.5). The Victory flake differs slightly in composition from the Margaret target. Victory has higher Cl and Fe/Mn, which is consistent with slightly greater degree of alteration for material composing the flake. However, the rocks from Wdowiak Ridge in general are not highly altered. Several of them have Fe/Mn close to the primary martian ratio (Fig. 24b) and have SO_3, Cl and Zn contents similar to those of brushed basalt targets from Gusev Crater (Fig. 23d) and generally lower than those of Shoemaker formation breccias (Table 1). Further, CRISM spectra of Wdowiak Ridge have relatively deep olivine and pyroxene absorption features compared to surrounding regions [*Arvidson et al*., 2015], which suggests that rocks on the ridge are less altered.

As was the case for Tick Bush, Wdowiak Ridge rocks have lower MgO and FeO, but higher Al_2O_3 than do Gusev Crater basalts, consistent with a more evolved volcanic composition (Fig. 23). However, these rocks show little variation in MgO coupled with substantial variation in Ni content; the high end of the range being similar to the Ni contents of Tick Bush (Fig. 23c). Excluding the Victory alteration flake, the Margaret target has the lowest Ni content amongst Wdowiak Ridge dark rocks. Its Ni content is similar to those of Gusev Crater basalts with much higher MgO contents (Fig. 23c). The Ni-MgO distribution for Wdowiak Ridge is inconsistent with magmatic trends in which MgO and Ni are typically well correlated. This suggests that either the Wdowiak Ridge rocks are fragments of impact melt variably contaminated with chondritic impactor material, or that Ni was mobilized during the modest alteration experienced by these rocks. Robust correlations between Ni and other volatile/mobile elements do not exist for these rocks, but there are general trends of increasing Ni with increasing SO_3, Cl and Zn, suggesting that Ni was indeed mobilized by alteration.

As discussed above, the two hypotheses for the origin of dark capping rocks on Wdowiak Ridge that are consistent with its common orientation with Endeavour Crater structural-elements are that they are impact melt emplaced with ejecta during formation of Endeavour Crater [*Grant et al*., 2015], or that Wdowiak Ridge is an upraised fault block created during impact [*Crumpler et al*., 2015b]. The first hypothesis implies that Wdowiak Ridge should contain a lithologic suite generally similar to the rocks elsewhere on the rim. Thus, the dark capping rock would be erosion-resistant material allowing formation of the topographic feature, while below the cap one would expect to find impact breccias, which are the dominant lithologic type of the rim. The abundance of unbrecciated rocks and an absence of impact breccias on Wdowiak Ridge suggest that this hypothesis is unlikely to be correct. The second hypothesis indicates that the dark capping rocks could represent a pre-impact surface. The many fracture planes within the rocks seem consistent with damage done during movement of a fault block during the impact. The compositions of the dark capping rock indicate that it is variably altered volcanic rock. Wdowiak Ridge is much smaller than the km-scale terrace blocks observed on the eastern side of Endeavour Crater [*Grant et al*., 2016], but these were formed by a different mechanism – collapse of the transient crater wall – and occur in the crater interior rather than outside the rim. Other linear ridges of the same scale as Wdowiak Ridge and subparallel to it occur nearby (see *Grant et al*., 2016, figure 5), but *Opportunity* was not commanded to investigate them. Considering the geological and compositional evidence, an origin for the Wdowiak Ridge dark rocks as an uplifted block of the pre-impact surface is more plausible.

6.5. Formation of Veneers on Matijevic formation Outcrops; Timing and Mechanism

The relative timing of veneer formation can be deduced using standard geological superposition criteria. As discussed in Section 4.2, veneers on Matijevic formation outcrops are small erosional remnants of a formerly more extensive coating on the outcrop (Fig. 6a). In one area (Fig. 6a inset), bright veins underlie a patch of veneer. Vein morphology is imposed on the veneer surface, but the veins do not cut the veneer. None of the images of Matijevic formation show instances where the bright Ca-sulfate-rich veins crosscut veneer. Similarly, dark veneer patches are present on the Lihir/Espérance boxwork vein that crosscuts the Matijevic formation [*Clark et al*., 2016]. These relationships indicate that veneer formation post-dated formation of veins in the Matijevic formation, regardless of vein type.

Veins are also present in the overlying Shoemaker and Grasberg formations, but these represent a distinct episode of fluid movement from those that formed the veins in the Matijevic formation. As noted in Sections 5.4 and 6.3, the fine, bright anastomosing veins in the Matijevic formation are compositionally distinct from the $CaSO_4$ veins that crosscut the Shoemaker and Grasberg formations, and the Lihir/Espérance boxwork vein is composed dominantly of aluminosilicate-rich phases, not Ca-sulfate [*Clark et al*., 2016]. *Farrand et al*. [2014] noted VNIR spectral differences between the Ca-sulfate veins in the Matijevic and Grasberg formations on the one hand, and between them and the boxwork veins on the other. These differences were most pronounced in the form of differences in 535 nm band depth, a good indicator for hematite or other ferric oxides. Together, the evidence indicates that the veins in the Matijevic formation are products of an earlier episode of fluid flowing through the Endeavour Crater rim rock suite than that which produced Ca-sulfate veins in the Grasberg and Shoemaker formations, a conclusion reached by *Farrand et al*. [2014].

One possible piece of contrary evidence is that fine, bright anastomosing veins, possibly of Ca-sulfate, occur in the Copper Cliff outcrop of the Shoemaker formation that directly overlies the Matijevic formation (Fig. 9 of *Arvidson et al*. [2014]). However the contact is often obscured by soil and lithic fragments (see Fig. 14 of *Crumpler et al*. [2015a]). Veins cannot be traced from Matijevic into Shoemaker rock.

The surface of the Matijevic formation was modified by the Endeavour impact. As discussed in Section 6.1, the composition of the Copper Cliff member and occurrences of spherules in it are consistent with erosion of the Matijevic formation during emplacement of the Endeavour ejecta and incorporation of eroded debris in the lowest unit of the Shoemaker formation. For comparison, emplacement of the Bunte Breccia at the Ries Crater caused tens of meters of erosion of the paleosurface [*Hörz et al*., 1983]. Erosion of the Matijevic formation surface thus would have removed the ~mm-thick veneer had it been present on the pre-impact surface.

Finally, geological evidence suggests that veneer formation predates development of the current surface. Veneer patches are present on the Matijevic surface below the Copper Cliff outcrop, but not on the smooth, gently sloped top surface of the Copper Cliff outcrop only a few tens of cm above veneer patches on the Matijevic formation. We conclude that it is unlikely that the veneers were formed on the current erosional surface.

Previously we concluded that the veneers were formed either on an ancient surface or along bedding plane fractures [*Arvidson et al*., 2014; *Crumpler et al*., 2015a]. Because dark veneers are present on the eroded surface of the crosscutting Lihir/Espérance boxwork vein, we conclude that the veneers were formed on an ancient erosional surface. Previously, we concluded that this occurred prior to deposition of the Shoemaker breccias [*Crumpler et al*., 2015a]. However, in view of the evidence presented here that the Matijevic was eroded and incorporated into the lower Shoemaker breccias during emplacement of the latter, we suggest that the veneers were formed by fluids moving through the Matijevic formation, altering the rock and precipitating salts along the Matijevic-Shoemaker unconformity.

We have concluded that the veneers are the host of the ferric smectite signature observed from orbit for this location [*Arvidson et al*., 2014]. The most likely smectite is nontronite, but the veneers do not show a strong enrichment in Fe as would be expected for a nontronite-rich rock. However, nontronite only needs to be a small fraction of the scene to engender the spectral signature detected by the CRISM instrument [*Arvidson et al*., 2014]. The veneer is enriched in the volatile/mobile elements (S, Cl, Zn and Br), K and Ca, with or without Mn compared to Matijevic formation matrix (Figs. 14, 15). A scenario consistent with the in-situ and orbital data is that small amounts of aqueous fluid mobilized the more labile elements, deposited them along the unconformity and altered a fraction of the silicates to ferric smectite with little change in bulk major element composition.

Thermodynamic modeling shows that ferric smectites can form on Mars through low-temperature oxidative weathering of basalt, or through later oxidative alteration of ferrous smectites produced during anoxic weathering [*Catalano*, 2013]. The calculations presented in that study were done for T = 25°C with different fluid contents of H_2SO_4 and HCO_3^-; the solutions were mildly acidic. The water/rock ratio for veneer formation cannot be constrained based on these calculations because we have no information on the total mineral assemblage. However, the veneers are thin, roughly mm-thickness, and are enriched, not depleted, in the more soluble elements (Fig. 14a). Together, this suggest relatively low water/rock ratios for the alteration process.

We infer that the sequence of events experienced by the Matijevic formation was: (i) deposition of clastic sediments; (ii) formation of fine, anastomosing Ca-sulfate veins and aluminosilicate boxwork veins; (iii) erosion exposing a pre-impact surface close to the present surface of the Matijevic formation; (iv) further erosion and deposition of Shoemaker formation breccias by the Endeavour impact; (v) veneer and ferric smectite formation along the unconformity; and (vi) erosion to form the present surface with remaining veneer scattered in patches.

6.6. Origin of the Grasberg Formation

The origin of the Grasberg formation is enigmatic. The consensus view of the MER science team, presented in *Crumpler et al*. [2015a], is that the Grasberg formation is a thin unit unconformably lying on an erosion surface (pediment) forming the lower slopes of the Endeavour Crater rim segments explored by *Opportunity*. Similar benches are present elsewhere at the contact between Endeavour Crater rim segments/terrace blocks and the Burns formation, and these are interpreted to be Grasberg formation [*Grant et al*., 2016]. An erosional unconformity in turn forms the upper contact with the overlying Burns formation [*Crumpler et al*., 2015a]. A contrary view, that the Grasberg formation overlies and is younger than the Burns formation [*Ruff*, 2013], is not well-supported by the geological observations as discussed in *Crumpler et al*. [2015a]. Our hypothesis is that the Grasberg formation was emplaced as a fine-grained airfall deposit that mantled paleotopography, and is a local expression of a widespread, homogeneous unit, possibly fine volcanic ash or distal debris from an impact [*Crumpler et al*., 2015a].

Assuming textures are primary, the fine-grained nature and general lack of sedimentary structures suggest formation in a low-energy environment such as by air fall of ash or dust. The only interior view we have of textures for the Grasberg formation are from the abrasion hole in the upper unit target Grasberg (Fig. 5a). As noted [*Crumpler et al*., 2015a], the lack of identifiable contact structures between the lower and upper Grasberg suggest that the upper unit might be a weathering cap rather than a distinct depositional unit. This is generally consistent with the compositions of the two units; we find no significant compositional differences between the two (Table 3). However, because the Grasberg formation is compositionally heterogeneous (Fig. 12) and few targets were analyzed, the compositional averages of the two units are not tightly constrained. If the upper unit is a weathering cap, then the featureless texture of the Grasberg target could simply reflect recrystallization that destroyed primary textures. In this case, we could make no conclusion regarding the environment of deposition from rock textures.

Two Burns formation targets, Guadalupe and Lion Stone, are composed of crystalline material with primary textures poorly preserved, possibly because of more extensive cementation and/or recrystallization [*McLennan et al*., 2005]. The specific grind energies for Guadalupe and Lion Stone were 46.2 and 18.1 J/mm^3, much higher than the values of <2 J/mm^3 typical for Burns formation targets (Table 20.4 of Herkenhoff et al. [2008]), and within or higher than the range of terrestrial limestone [*Arvidson et al*., 2004]. The compositions of Guadalupe and Lion Stone are within the ranges for other abraded Burns formation targets (Fig. 12). Erosion-resistant fracture fills present within the Burns formation are possibly cemented by Fe-oxides and/or silica [*Knoll et al*., 2008]. Guadalupe and Lion Stone are amongst the more FeO-poor abraded Burns formation targets (Fig. 12c), and their SiO_2 contents (36.2 and 37.2 wt%) are within the range of other abraded Burns formation targets; most are between 34.4 and 41.1 wt%. Thus, there is no compositional evidence for mineralization of Guadalupe or Lion Stone that could explain their high specific grind energy. The strengths of these two targets reflect a higher degree of recrystallization and/or cementation under isochemical conditions than experienced by most Burns formation rocks.

The specific grind energy for Grasberg is 7.6 J/mm^3 [*Crumpler et al*., 2015a], substantially less than that for Guadalupe or Lion Stone. Because Grasberg is considerably weaker than either of those Burns formation rocks, and the latter still retain some evidence of their primary sedimentary structures, we conclude that Grasberg originated as a very fine-grained sediment. However, the lower Grasberg unit target Poverty Bush shows fine-scale wavy laminations in outcrop (Fig. 4e), yet appears homogeneous and very fine-grained in MI images (Fig. 5d). This could be contrary evidence to our conclusion: Poverty Bush could be completely recrystallized with primary macroscopic sedimentary structures remaining as pseudomorphs. Pancam and MI observations on untreated and abraded targets of a Grasberg formation rock like Poverty Bush would be required to address this issue. Note that the fine-scale wavy lamination texture of Poverty Bush does not obviously fit with an interpretation as an airfall deposit, but is not entirely inconsistent with that hypothesis. For example, localized reworking of the sediment prior to lithification, possibly by water, could explain the textures. Additional observations of the Grasberg formation would be needed to address this issue.

Absent definitive evidence to the contrary, we continue to carry the working hypothesis that the Grasberg formation is a widespread airfall deposit draped on an erosional pediment. Originally, the Grasberg sediments would have also formed a layer on the ridges of Endeavour rim segments, but must have been eroded from them. The rim segments have been degraded by 100-200 m since formation, but much of that occurred prior to deposition of the Burns formation [*Grant et al*., 2016]. The interpretation that the Grasberg formation sits on an erosional pediment [*Crumpler et al*., 2015a] indicates that much of the rim degradation also occurred prior deposition of the Grasberg sediments. Continuing erosion during the Hesperian [*Golombek et al*., 2006] would have been sufficient to remove a thin draping unit such as the Grasberg from the ridges.

The composition of the Grasberg formation is distinct from the other lithologies in the region, especially so if volatile/mobile elements are excluded from consideration (Fig. 16c). We posited that the Grasberg could be either volcanic or impact-derived in origin [*Crumpler et al*., 2015a]. Grasberg rocks are broadly basaltic in composition, but are not well-matched by expectations for volcanics. The MgO contents are lower than likely martian basalts (e.g., Fig. 23a) which could indicate an evolved magma. However, the Al_2O_3 contents are low and FeO contents are high (Fig. 23b) which preclude such an origin. The high Fe/Mn, most likely caused by low MnO contents (Fig. 24), indicates mobilization of elements during alteration as discussed in Sections 6.2 and 6.3. For this reason, we cannot infer a plausible origin for the Grasberg formation based on composition. The origin of the Grasberg formation remains enigmatic, and study of further outcrops are required to test our working hypothesis.

6.7. Geological and Alteration History of the Endeavour Crater Rim

Based on the geological and compositional evidenced presented above, we suggest the following scenario for the geological and alteration history of the region of the western rim of Endeavour Crater:

1. Alteration of pre-impact rocks prior to the impact, including formation of fine, anastomosing Ortiz $CaSO_4$-rich veins and aluminosilicate (boxwork) veins that crosscut the Matijevic formation [*Arvidson et al*., 2014; *Clark et al*., 2016]. Calcium-sulfate-rich veins were likely precipitated from dilute solutions at moderate (<50°C temperatures. The formation of the boxwork veins was a hydrothermal process. Modest alteration by low-temperature weathering processes of dark rocks that were ultimately emplaced on the rim and the cap rock on Wdowiak Ridge may also have occurred at this time.

2. Erosion to form the pre-impact surface.

3. The Endeavour impactor excavated the crater, eroded the surface outside the crater and deposited polymict-breccia ejecta.

4. Alteration under low water/rock mobilized elements within the Matijevic formation and formed veneers along the unconformity between the Matijevic and Shoemaker. This was a low-temperature alteration process in mildly acidic solutions at a low

water/rock ratio. These are the presumed carriers of the ferric-smectite signature observed in CRISM spectra [*Arvidson et al*., 2014].

5. Fracture zones served as conduits for alteration fluids, possibly mobilized by heat from the impact. The Cook Haven region lies within one such fracture zone [*Arvidson et al*., 2016]. The Shoemaker formation targets from this region have generally higher SO_3 and Cl contents indicative of alteration. Rocks in this region that were flipped by *Opportunity's* wheels have compositions and mineralogies that reflect precipitation of sulfate salts and Mn oxides precipitated from solutions formed through alteration of basaltic-composition protoliths, but the processes that produced the solutions are not well-constrained by data [*Arvidson et al*., 2016].

6. Following a period of erosion, the deposition of fine-grained Grasberg formation sediments as airfall unconformably on the Shoemaker formation and any exposed pre-impact surfaces occurred [*Crumpler et al*., 2015a].

7. After additional erosion, the sulfate-rich sands of the Burns formation were deposited on the Grasberg and Shoemaker formations. The timing of the diagenesis of the Burns formation [*Grotzinger et al*., 2005; *McLennan et al*., 2005; *Squyres and Knoll*, 2005] in this sequence is unclear.

8. The final alteration event was formation of $CaSO_4$ veins in the Grasberg and Shoemaker formations under conditions similar to those described above for the Ortiz veins. The coarsest veins crosscut the Grasberg formation. A hydrologic head is required to have forced fluids up to locations as high as Bristol Well on Pillinger Point, suggesting that this episode likely occurred later, after a thick section of Burns formation was in place. Groundwaters flushed through the region and redox exchange differentially mobilized Fe and Mn in the Grasberg and Shoemaker formations in mildly acidic to circumneutral solutions. This event might have indurated the Grasberg formation.

9. Degradation of the rim likely began as soon as, or shortly after, it was formed [*Grant et al*., 2016], but degradation since the final alteration event would have been sufficient to remove Grasberg formation sediments from higher positions on the rim (cf., *Golombek et al*. [2006]).

Endeavour Crater is Noachian in age and events 1 through 3 occurred during that epoch. We infer that events 5 and 6 are also Noachian, but we have no hard constraints on this. Because formation of $CaSO_4$ veins in the Grasberg and Shoemaker formations likely occurred after deposition of the Burns formation, this alteration was Early Hesperian in age.

7. Conclusions

The imaging of and compositional data for pre-Burns-formation rocks from along the Endeavour Crater rim allow us to further refine our interpretations of the origin of the rocks and the alteration processes that affected them:

- The Matijevic formation is a unit of fine-grained clastic sediments that, because of the limited exposure, is of unknown areal and stratigraphic extent. It is the only definitive intact, pre-impact unit examined, and might be part of the Noachian etched units of Meridiani Planum (cf., *Hynek and Di Achille* [2017]). Dark cap rocks on Wdowiak Ridge might be a pre-impact lithology, but the case is less compelling for them.
- The Shoemaker formation is a heterogeneous polymict breccia. The lowermost unit on Cape York incorporates material eroded from the underlying Matijevic formation during deposition of the ejecta. The Shoemaker is heterogeneous on the cm to km scale as revealed by compositional differences between clasts and matrix, variations within outcrops (Greeley Haven) and differences between rim segments. The Shoemaker formation is an analog to the Bunte Breccia of the Ries Crater, but average clast sizes are substantially smaller in the Shoemaker.
- The Grasberg formation is a 1-2 m thick fine-grained, homogeneous sedimentary unit that lies unconformably on the Shoemaker formation. It typically does not show sedimentary structures, consistent with deposition in a low-energy environment. It likely represents an airfall deposit of widespread areal extent. Although the Burns formation overlies the Grasberg, the compositions of two units are quite distinct. There is no evidence, compositional or textural, that the Grasberg formation might be a separate, fine-grained facies of the Burns formation as has been argued for the rare mudstones found on the plains in the ejecta from Santa Maria crater [*Edgar et al*, 2014]. The composition of Grasberg rocks was changed by aqueous alteration which cause differential mobility of Mn and Fe, and possibly other elements, and deposition of $CaSO_4$ in coarse veins.
- At least four episodes of alteration occurred in the Noachian and Early Hesperian in the region, not counting diagenesis of the Burns formation sandstones: (i) pre-impact alteration of regional rocks, including formation of $CaSO_4$-rich and aluminosilicate veins in the Matijevic formation; (ii) low water/rock alteration along the disconformity between the Matijevic and Shoemaker formations forming veneers; (iii) alteration along fracture zones in the rim segments; and (iv) differential mobilization of Fe and Mn, and $CaSO_4$ vein formation. Episodes (ii) and (iii) possibly occurred together, but (i) and (iv) are distinct.

Acknowledgements-Rover operations described in this paper were conducted at the Jet Propulsion Laboratory, California Institute of Technology, under a contract with NASA. We thank the members of the MER project who enabled daily science observations at the *Opportunity* landing site. The senior author is supported by the NASA Mars Exploration Rover Participating Scientist Program. We thank F. Hörz for enlightening and enormously helpful discussions on the geology of the Ries crater. We thank him and M. Cintala for discussions on cratering and impact phenomena in general, B. L. Redding for preparing the MI mosaics used here, J. B. Proton for help with some of the Pancam images, and J. R. Johnson and S. M. McLennan for comments on a draft version of the manuscript. We thank the reviewers A. Fraeman and H. Newsom, and Associate Editor A. D. Rogers for their comments and suggestions which led to substantial improvement of the manuscript. All data used in this article are listed in the references, tables, and supplements. Data for APXS integrations on all rock and soil targets acquired by *Opportunity* through Sol 4000 are available on the NASA Planetary Data System website: http://pds-geosciences.wustl.edu/.

References

Andrews-Hanna, J. C., and K. W. Lewis (2011), Early Mars hydrology: 2. Hydrological evolution in the Noachian and Hesperian epochs, *Journal of Geophysical Research: Planets*, *116*(E2), E02007, doi:10.1029/2010JE003709.

Andrews-Hanna, J. C., R. J. Phillips, and M. T. Zuber (2007), Meridiani Planum and the global hydrology of Mars, *Nature*, *446*(7132), 163-166, doi:http://www.nature.com/nature/journal/v446/n7132/suppinfo/nature05594_S1.html.

Artemieva, N. A., K. Wünnemann, F. Krien, W. U. Reimold, and D. Stöffler (2013), Ries crater and suevite revisited—Observations and modeling Part II: Modeling, *Meteoritics & Planetary Science*, *48*(4), 590-627, doi:10.1111/maps.12085.

Arvidson, R. E., R. Anderson, P. Bartlett, J. Bell, D. Blaney, P. Christensen, P. Chu, L. Crumpler, K. Davis, and B. Ehlmann (2004), Localization and physical properties experiments conducted by Spirit at Gusev Crater, *Science*, *305*(5685), 821-824.

Arvidson, R. E., et al. (2011), *Opportunity* Mars Rover mission: Overview and selected results from Purgatory ripple to traverses to Endeavour crater, *Journal of Geophysical Research: Planets*, *116*(E7), E00F15, doi:10.1029/2010JE003746.

Arvidson, R. E., et al. (2014), Ancient Aqueous Environments at Endeavour Crater, Mars, *Science*, *343*(6169), doi:10.1126/science.1248097.

Arvidson, R. E., S. W. Squyres, R. Gellert, and A. S. Team (2015), Recent Results from the Opportunity Rover's Exploration of Endeavour Crater, Mars, in *46th Lunar and Planetary Science Conference*, edited, p. Abstract #1118, Lunar and Planetary Institute, Houston.

Arvidson, R. E., et al. (2016), High concentrations of manganese and sulfur in deposits on Murray Ridge, Endeavour Crater, Mars, *American Mineralogist*, *101*(6), 1389-1405, doi:10.2138/am-2016-5599.

Azimi, G., and V. G. Papangelakis (2010), Thermodynamic modeling and experimental measurement of calcium sulfate in complex aqueous solutions, *Fluid Phase Equilibria*, *290*(1), 88-94, doi:https://doi.org/10.1016/j.fluid.2009.09.023.

Azimi, G., V. G. Papangelakis, and J. E. Dutrizac (2007), Modelling of calcium sulphate solubility in concentrated multi-component sulphate solutions, *Fluid Phase Equilibria*, *260*(2), 300-315, doi:https://doi.org/10.1016/j.fluid.2007.07.069.

Bell, J., S. Squyres, K. Herkenhoff, J. Maki, H. Arneson, D. Brown, S. Collins, A. Dingizian, S. Elliot, and E. Hagerott (2003), Mars exploration rover Athena panoramic camera (Pancam) investigation, *Journal of Geophysical Research: Planets (1991–2012)*, *108*(E12).

Catalano, J. G. (2013), Thermodynamic and mass balance constraints on iron-bearing phyllosilicate formation and alteration pathways on early Mars, *Journal of Geophysical Research: Planets*, *118*(10), 2124-2136, doi:10.1002/jgre.20161.

Chayes, F. (1971), *Ratio correlation: a manual for students of petrology and geochemistry*, 99 pp., University of Chicago Press, Chicago.

Christensen, P. R., G. L. Mehall, S. H. Silverman, S. Anwar, G. Cannon, N. Gorelick, R. Kheen, T. Tourville, D. Bates, and S. Ferry (2003), Miniature thermal emission spectrometer for the Mars Exploration rovers, *Journal of Geophysical Research: Planets (1991–2012)*, *108*(E12).

Clark, B. C., et al. (2005), Chemistry and mineralogy of outcrops at Meridiani Planum, *Earth and Planetary Science Letters*, *240*(1), 73-94, doi:10.1016/j.epsl.2005.09.040.

Clark, B. C., et al. (2016), Esperance: Multiple episodes of aqueous alteration involving fracture fills and coatings at Matijevic Hill, Mars, in *American Mineralogist*, edited, pp. 1515-1526, doi:10.2138/am-2016-5575.

Cousin, A., V. Sautter, V. Payré, O. Forni, N. Mangold, O. Gasnault, L. Le Deit, J. Johnson, S. Maurice, and M. Salvatore (2017), Classification of igneous rocks analyzed by ChemCam at Gale crater, Mars, *Icarus*, *288*, 265-283.

Crumpler, L. S., et al. (2015a), Context of ancient aqueous environments on Mars from in situ geologic mapping at Endeavour Crater, *Journal of Geophysical Research: Planets*, *120*(3), 2014JE004699, doi:10.1002/2014JE004699.

Crumpler, L. S., R. E. Arvidson, W. H. Farrand, M. P. Golombek, J. A. Grant, D. W. Ming, D. W. Mittlefehldt, and T. J. Parker (2015b), Opportunity In Situ Geologic Context of Aqueous Alteration Along Offsets in the Rim of Endeavour Crater, in *46th Lunar and Planetary Science Conference*, edited, p. Abstract #2209, Lunar and Planetary Institute, Houston.

Crumpler, L. S., R. E. Arvidson, M. Golombek, B. L. Jollif, and D. W. Mittlefehldt (2017), Rim Structure, Stratigraphy, and Aqueous Alteration Exposures Along Opportunity Rover's Traverse of the Noachian Endeavour Crater, in *48th Lunar and Planetary Science Conference*, edited, p. Abstract #2276, Lunar and Planetary Institute, Houston.

Drever, J. I. (1997), *The Geochemistry of Natural Waters: Surface and Groundwater Environments*, 436 pp., Prentice Hall, Eaglewood Cliffs, NJ.

Edgar, L. A., J. P. Grotzinger, A. G. Hayes, D. M. Rubin, S. W. Squyres, J. F. Bell, and K. E. Herkenhoff (2012), Stratigraphic architecture of bedrock reference section, Victoria crater, Meridiani Planum, Mars, *Sedimentary Geology of Mars, SEPM Special Publication*, *102*, 195-209.

Edgar, L. A., J. P. Grotzinger, J. F. Bell, and J. A. Hurowitz (2014), Hypotheses for the origin of fine-grained sedimentary rocks at Santa Maria crater, Meridiani Planum, *Icarus*, *234*, 36-44.

Farrand, W.H., J.F. Bell III, J.R. Johnson, B.L. Joliff, A.H. Knoll, S.M. McLennan, S.W. Squyres, W.M. Calvin, J.P. Grotzinger, R.V. Morris, J. Soderblom, S.D. Thompson, W.A. Watters, and A.S. Yen (2007) Visible and near-infrared multispectral analysis of rocks at Meridiani Planum, Mars by the Mars Exploration Rover Opportunity, *Journal of Geophysical Research: Planets*, *112*, E06S02, 10.1029/2006JE002773.

Farrand, W.H., J.F. Bell III, J.R. Johnson, M.S. Rice, and J.A. Hurowitz (2013) VNIR multispectral observations of rocks at Cape York, Endeavour crater, Mars by the Opportunity rover's Pancam, *Icarus*, *225*, 709-725.

Farrand, W.H., J.F. Bell III, J.R. Johnson, M.S. Rice, B.L. Jolliff, and R.E. Arvidson (2014) Observations of rock spectral classes by the Opportunity rover's Pancam on northern Cape York and on Matijevic Hill, Endeavour Crater, Mars, *Journal of Geophysical Research: Planets*, *119*, doi:10.1002/2014JE004641.

Farrand, W.H., J.R. Johnson, M.S. Rice, A. Wang, and J.F. Bell III (2016) VNIR multispectral observations of aqueous alteration materials by the Pancams on the Spirit and Opportunity Mars Exploration Rovers, *American Mineralogist*, *101*, 2005-2019, doi:0.2138/am-2016-5627.

Fox, V. K., R. E. Arvidson, E. A. Guinness, S. M. McLennan, J. G. Catalano, S. L. Murchie, and K. E. Powell (2016), Smectite deposits in Marathon Valley, Endeavour Crater, Mars, identified using CRISM hyperspectral reflectance data, *Geophysical Research Letters*, 43, 4885-4892, doi:10.1002/2016GL069108.

Filiberto, J., A. H. Treiman, and L. Le (2008), Crystallization experiments on a Gusev Adirondack basalt composition, *Meteoritics & Planetary Science*, *43*(7), 1137-1146, doi:10.1111/j.1945-5100.2008.tb01118.x.

Gellert, R., R. Rieder, R. Anderson, J. Brückner, B. Clark, G. Dreibus, T. Economou, G. Klingelhöfer, G. Lugmair, and D. Ming (2004), Chemistry of rocks and soils in Gusev Crater from the Alpha Particle X-ray Spectrometer, *Science*, *305*(5685), 829-832.

Gellert, R., et al. (2006), Alpha Particle X-Ray Spectrometer (APXS): Results from Gusev crater and calibration report, *Journal of Geophysical Research: Planets*, *111*(E2), E02S05, doi:10.1029/2005JE002555.

Golombek, M., J. Grant, L. Crumpler, R. Greeley, R. Arvidson, J. Bell, C. Weitz, R. Sullivan, P. Christensen, and L. Soderblom (2006), Erosion rates at the Mars Exploration Rover landing sites and long-term climate change on Mars, *Journal of Geophysical Research: Planets (1991–2012)*, *111*(E12).

Gorevan, S., T. Myrick, K. Davis, J. Chau, P. Bartlett, S. Mukherjee, R. Anderson, S. Squyres, R. Arvidson, and M. Madsen (2003), Rock abrasion tool: Mars exploration rover mission, *Journal of Geophysical Research: Planets (1991–2012)*, *108*(E12).

Grant, J. A., L. S. Crumpler, T. J. Parker, M. P. Golombek, S. A. Wilson, and D. W. Mittlefehldt (2015), Degradation of Endeavour Crater, Mars, in *46th Lunar and Planetary Science Conference*, edited, p. Abstract #2017, Lunar and Planetary Institute, Houston.

Grant, J. A., T. J. Parker, L. S. Crumpler, S. A. Wilson, M. P. Golombek, and D. W. Mittlefehldt (2016), The degradational history of Endeavour crater, Mars, *Icarus*, *280*, 22-36, doi:http://dx.doi.org/10.1016/j.icarus.2015.08.019.

Greeley, R., B. H. Foing, H. Y. McSween, G. Neukum, P. Pinet, M. van Kan, S. C. Werner, D. A. Williams, and T. E. Zegers (2005), Fluid lava flows in Gusev crater, Mars, *Journal of Geophysical Research: Planets*, *110*(E5), E05008, doi:10.1029/2005JE002401.

Grieve, R. A. F., D. E. Ames, J. V. Morgan, and N. Artemieva (2010), The evolution of the Onaping Formation at the Sudbury impact structure, *Meteoritics & Planetary Science*, *45*(5), 759-782, doi:10.1111/j.1945-5100.2010.01057.x.

Grotzinger, J. P., et al. (2005), Stratigraphy and sedimentology of a dry to wet eolian depositional system, Burns formation, Meridiani Planum, Mars, *Earth and Planetary Science Letters*, *240*(1), 11-72, doi:https://doi.org/10.1016/j.epsl.2005.09.039.

Grotzinger, J., et al. (2006), Sedimentary textures formed by aqueous processes, Erebus crater, Meridiani Planum, Mars, *Geology*, *34*(12), 1085-1088, doi:10.1130/g22985a.1.

Haskin, L. A., A. Wang, B. L. Jolliff, H. Y. McSween, B. C. Clark, D. J. Des Marais, S. M. McLennan, N. J. Tosca, J. A. Hurowitz, and J. D. Farmer (2005), Water alteration of rocks and soils on Mars at the Spirit rover site in Gusev crater, *Nature*, *436*(7047), 66-69.

Hayes, A., J. Grotzinger, L. Edgar, S. Squyres, W. Watters, and J. Sohl-Dickstein (2011), Reconstruction of eolian bed forms and paleocurrents from cross-bedded strata at Victoria Crater, Meridiani Planum, Mars, *Journal of Geophysical Research: Planets*, *116*(E7).

Herkenhoff, K., S. Squyres, J. Bell, J. Maki, H. Arneson, P. Bertelsen, D. Brown, S. Collins, A. Dingizian, and S. Elliott (2003), Athena Microscopic Imager investigation, *Journal of Geophysical Research: Planets (1991–2012)*, *108*(E12).

Herkenhoff, K. E., M. P. Golombek, E. A. Guinness, J. B. Johnson, A. Kusack, L. Richter, R. J. Sullivan Jr, and S. Gorevan (2008), In situ observations of the physical properties of the Martian surface, in *The Martian Surface: Composition, Mineralogy, and Physical Properties*, edited by J. F. Bell III, pp. 451-467, Cambridge University Press, Cambridge, UK.

Hörz, F. (1982), Ejecta of the Ries crater, Germany, in *Geological Implications of Impacts of Large Asteroids and Comets on the Earth*, edited by L. T. Silver and P. H. Schultz, pp. 39-55, Geological Society of America, Boulder, CO, USA.

Hörz, F., R. Ostertag, and D. A. Rainey (1983), Bunte Breccia of the Ries: Continuous deposits of large impact craters, *Reviews of Geophysics*, *21*(8), 1667-1725, doi:10.1029/RG021i008p01667.

Hurowitz, J. A., W. W. Fischer, N. J. Tosca, and R. E. Milliken (2010), Origin of acidic surface waters and the evolution of atmospheric chemistry on early Mars, *Nature Geoscience*, *3*(5), 323.

Hynek, B. M., and G. Di Achille (2017), Geologic map of Meridiani Planum, Mars, U.S. Geological Survey Scientific Investigations Map 3356, https://doi.org/10.3133/sim3356.

Hynek, B. M., and R. J. Phillips (2008), The stratigraphy of Meridiani Planum, Mars, and implications for the layered deposits' origin, *Earth and Planetary Science Letters*, *274*(1–2), 214-220, doi:https://doi.org/10.1016/j.epsl.2008.07.025.

Hynek, B. M., R. E. Arvidson, and R. J. Phillips (2002), Geologic setting and origin of Terra Meridiani hematite deposit on Mars, *J. Geophys. Res.*, *107*(E10), 5088, doi:10.1029/2002je001891.

Klingelhoefer, G., R. V. Morris, B. Bernhardt, D. Rodionov, P. De Souza, S. Squyres, J. Foh, E. Kankeleit, U. Bonnes, and R. Gellert (2003), Athena MIMOS II Mössbauer spectrometer investigation, *Journal of Geophysical Research: Planets (1991–2012)*, *108*(E12).

Klingelhöfer, G., et al. (2004), Jarosite and Hematite at Meridiani Planum from Opportunity's Mössbauer Spectrometer, *Science*, *306*(5702), 1740-1745, doi:10.1126/science.1104653.

Knoll, A. H., et al. (2008), Veneers, rinds, and fracture fills: Relatively late alteration of sedimentary rocks at Meridiani Planum, Mars, *Journal of Geophysical Research: Planets*, *113*(E6), E06S16, doi:10.1029/2007JE002949.

Lanza, N. L., et al. (2016), Oxidation of manganese in an ancient aquifer, Kimberley formation, Gale crater, Mars, *Geophysical Research Letters*, *43*(14), 2016GL069109, doi:10.1002/2016GL069109.

Lemmon, M. T., et al. (2004), Atmospheric Imaging Results from the Mars Exploration Rovers: Spirit and Opportunity, *Science*, *306*(5702), 1753-1756, doi:10.1126/science.1104474.

Lindsay, W. L. (1979), *Chemical Equilibria in Solids*, 449 pp., John WIley and Sons, New York, NY.

Maki, J., J. Bell, K. Herkenhoff, S. Squyres, A. Kiely, M. Klimesh, M. Schwochert, T. Litwin, R. Willson, and A. Johnson (2003), Mars Exploration Rover engineering cameras, *Journal of Geophysical Research: Planets*, *108*(E12).

McLennan, S. M., et al. (2005), Provenance and diagenesis of the evaporite-bearing Burns formation, Meridiani Planum, Mars, *Earth and Planetary Science Letters*, *240*(1), 95-121, doi:https://doi.org/10.1016/j.epsl.2005.09.041.

McSween, H., R. Arvidson, J. Bell, D. Blaney, N. Cabrol, P. Christensen, B. Clark, J. Crisp, L. Crumpler, and D. Des Marais (2004), Basaltic rocks analyzed by the Spirit rover in Gusev Crater, *Science*, *305*(5685), 842-845.

McSween, H. Y., et al. (2006), Characterization and petrologic interpretation of olivine-rich basalts at Gusev Crater, Mars, *Journal of Geophysical Research: Planets*, *111*(E2), E02S10, doi:10.1029/2005JE002477.

Melosh, H. J. (1989), *Impact cratering: A geologic process*, 253 pp., Oxford University Press, New York.

Ming, D. W., et al. (2008), Geochemical properties of rocks and soils in Gusev Crater, Mars: Results of the Alpha Particle X-Ray Spectrometer from Cumberland Ridge to Home Plate, *Journal of Geophysical Research: Planets*, *113*(E12), E12S39, doi:10.1029/2008JE003195.

Ming, D. W., et al. (2015), Iron-Manganese Redox Reactions in Endeavour Crater Rim Apron Rocks, in *46th Lunar and Planetary Science Conference*, edited, p. Abstract #2676, Lunar and Planetary Institute, Houston.

Mittlefehldt, D. W., et al. (2015), Noachian Impact Ejecta on Murray Ridge and Pre-Impact Rocks on Wdowiak Ridge, Endeavour Crater, Mars: Opportunity Observations, in *46th Lunar and Planetary Science Conference*, edited, p. Abstract #2705, Lunar and Planetary Institute, Houston.

Monders, A. G., E. Médard, and T. L. Grove (2007), Phase equilibrium investigations of the Adirondack class basalts from the Gusev plains, Gusev crater, Mars, *Meteoritics & Planetary Science*, *42*(1), 131-148, doi:10.1111/j.1945-5100.2007.tb00222.x.

Morris, R. V., G. Klingelhoefer, B. Bernhardt, C. Schröder, D. S. Rodionov, P. De Souza, A. Yen, R. Gellert, E. Evlanov, and J. Foh (2004), Mineralogy at Gusev Crater from the Mössbauer spectrometer on the Spirit Rover, *Science*, *305*(5685), 833-836.

Morris, R. V., et al. (2006a), Mössbauer mineralogy of rock, soil, and dust at Meridiani Planum, Mars: Opportunity's journey across sulfate-rich outcrop, basaltic sand and dust, and hematite lag deposits, *Journal of Geophysical Research: Planets*, *111*(E12), E12S15, doi:10.1029/2006JE002791.

Morris, R. V., G. Klingelhoefer, C. Schröder, D. S. Rodionov, A. Yen, D. W. Ming, P. De Souza, I. Fleischer, T. Wdowiak, and R. Gellert (2006b), Mössbauer mineralogy of rock, soil, and dust at Gusev crater, Mars: Spirit's journey through weakly altered olivine basalt on the plains and pervasively altered basalt in the Columbia Hills, *Journal of Geophysical Research: Planets (1991–2012)*, *111*(E2).

Nachon, M., S. Clegg, N. Mangold, S. Schröder, L. Kah, G. Dromart, A. Ollila, J. Johnson, D. Oehler, and J. Bridges (2014), Calcium sulfate veins characterized by ChemCam/Curiosity at Gale crater, Mars, *Journal of Geophysical Research: Planets*, *119*(9), 1991-2016.

Newsom, H. E., C. A. Barber, T. M. Hare, R. T. Schelble, V. A. Sutherland, and W. C. Feldman (2003), Paleolakes and impact basins in southern Arabia Terra, including Meridiani Planum: Implications for the formation of hematite deposits on Mars, *Journal of Geophysical Research: Planets*, *108*(E12), doi:10.1029/2002JE001993.

Noe Dobrea, E. Z., J. J. Wray, F. J. Calef III, T. J. Parker, and S. L. Murchie (2012), Hydrated minerals on Endeavour Crater's rim and interior, and surrounding plains: New insights from CRISM data, *Geophys. Res. Lett.*, *39*, L23201, doi:10.1029/2012GL053180.

Osinski, G. R., R. A. F. Grieve, and J. G. Spray (2004), The nature of the groundmass of surficial suevite from the Ries impact structure, Germany, and constraints on its origin, *Meteoritics & Planetary Science*, *39*(10), 1655-1683, doi:10.1111/j.1945-5100.2004.tb00065.x.

Osinski, G. R., R. A. F. Grieve, A. Chanou, and H. M. Sapers (2016), The "suevite" conundrum, Part 1: The Ries suevite and Sudbury Onaping Formation compared, *Meteoritics & Planetary Science*, *51*(12), 2316-2333, doi:10.1111/maps.12728.

Papike, J. J., J. M. Karner, and C. K. Shearer (2003), Determination of planetary basalt parentage: A simple technique using the electron microprobe, *American Mineralogist*, *88*(2), 469-472.

Parker, M. v. K., T. Zegers, T. Kneissl, B. Ivanov, B. Foing, and G. Neukum (2010), 3D structure of the Gusev Crater region, *Earth and Planetary Science Letters*, *294*(3–4), 411-423, doi:http://dx.doi.org/10.1016/j.epsl.2010.01.013.

Pohl, J., D. Stöffler, H. Gall, and K. Ernstson (1977), The Ries impact crater, in *Impact and explosion cratering: Planetary and terrestrial implications*, edited by D. J. Roddy, R. O. Pepin and R. B. Merrill, pp. 343-404, Pergamon Press, New York.

Pollack, J. B., D. S. Colburn, F. M. Flasar, R. Kahn, C. E. Carlston, and D. Pidek (1979), Properties and effects of dust particles suspended in the Martian atmosphere, *Journal of Geophysical Research: Solid Earth*, *84*(B6), 2929-2945, doi:10.1029/JB084iB06p02929.

Pollack, J. B., M. E. Ockert-Bell, and M. K. Shepard (1995), Viking Lander image analysis of Martian atmospheric dust, *Journal of Geophysical Research: Planets*, *100*(E3), 5235-5250, doi:10.1029/94JE02640.

Rice, M.S., J.F. Bell III, E.A. Cloutis, A. Wang, S.W. Ruff, M.A. Craig, D.T. Baily, J.R. Johnson, P.A. de Souza Jr., and W.H. Farrand (2010) Silica-rich deposits and hydrated minerals at Gusev crater, Mars: Vis-NIR spectral characterization and regional mapping, *Icarus*, *205*, 375–395.

Rieder, R., R. Gellert, J. Brückner, G. Klingelhöfer, G. Dreibus, A. Yen, and S. Squyres (2003), The new Athena alpha particle X-ray spectrometer for the Mars Exploration Rovers, *Journal of Geophysical Research: Planets (1991–2012)*, *108*(E12).

Rieder, R., et al. (2004), Chemistry of Rocks and Soils at Meridiani Planum from the Alpha Particle X-ray Spectrometer, *Science*, *306*(5702), 1746-1749, doi:10.1126/science.1104358.

Ruff, S. W. (2013), The Enigmatic Bench Unit of Endeavour Crater Rim in Meridiani Planum, Mars, *AGU Fall Meeting Abstracts*, P23F-1857.

Schmidt, M. E., and T. J. McCoy (2010), The evolution of a heterogeneous Martian mantle: Clues from K, P, Ti, Cr, and Ni variations in Gusev basalts and shergottite meteorites, *Earth and Planetary Science Letters*, *296*(1–2), 67-77, doi:10.1016/j.epsl.2010.04.046.

Shukla, J., V. P. Mohandas, and A. Kumar (2008), Effect of pH on the Solubility of $CaSO_4 \cdot 2H_2O$ in Aqueous NaCl Solutions and Physicochemical Solution Properties at 35 °C, *Journal of Chemical & Engineering Data*, *53*(12), 2797-2800, doi:10.1021/je800465f.

Siegert, S., M. J. Branney, and L. Hecht (2017), Density current origin of a melt-bearing impact ejecta blanket (Ries suevite, Germany), *Geology*, *45*(9), 855-858, doi:10.1130/G39198.1.

Squyres, S. W., and A. H. Knoll (2005), Sedimentary rocks at Meridiani Planum: Origin, diagenesis, and implications for life on Mars, *Earth and Planetary Science Letters*, *240*(1), 1-10, doi:https://doi.org/10.1016/j.epsl.2005.09.038.

Squyres, S. W., R. E. Arvidson, E. T. Baumgartner, J. F. Bell, P. R. Christensen, S. Gorevan, K. E. Herkenhoff, G. Klingelhöfer, M. B. Madsen, and R. V. Morris (2003), Athena Mars rover science investigation, *Journal of Geophysical Research: Planets (1991–2012)*, *108*(E12).

Squyres, S. W., et al. (2006), Overview of the *Opportunity* Mars Exploration Rover Mission to Meridiani Planum: Eagle Crater to Purgatory Ripple, *J. Geophys. Res.*, *111*(E12), E12S12, doi:10.1029/2006je002771.

Squyres, S. W., et al. (2012), Ancient Impact and Aqueous Processes at Endeavour Crater, Mars, *Science*, *336*(6081), 570-576, doi:10.1126/science.1220476.

Stöffler, D., N. A. Artemieva, K. Wünnemann, W. U. Reimold, J. Jacob, B. K. Hansen, and I. A. T. Summerson (2013), Ries crater and suevite revisited—Observations and modeling Part I: Observations, *Meteoritics & Planetary Science*, *48*(4), 515-589, doi:10.1111/maps.12086.

Stumm, W., and J. J. Morgan (1996), *Aquatic Chemistry: Chemical Equilibria and Rates in Natural Waters*, 1022 pp., John Wiley and Sons, New York, NY.

Sullivan, R., et al. (2005), Aeolian processes at the Mars Exploration Rover Meridiani Planum landing site, *Nature*, *436*(7047), 58-61.

Tanaka, K. L., J. A. Skinner, Jr., J. M. Dohm, R. P. Irwin, III, E. J. Kolb, C. M. Fortezzo, T. Platz, G. G. Michael, and T. M. Hare (2014), Geologic map of Mars, U.S. Geological Survey Scientific Investigations Map 3292.

Wiseman, S. M., et al. (2008), Phyllosilicate and sulfate-hematite deposits within Miyamoto crater in southern Sinus Meridiani, Mars, *Geophysical Research Letters*, *35*(19), L19204, doi:10.1029/2008GL035363.

Wray, J. J., E. Z. Noe Dobrea, R. E. Arvidson, S. M. Wiseman, S. W. Squyres, A. S. McEwen, J. F. Mustard, and S. L. Murchie (2009), Phyllosilicates and sulfates at Endeavour Crater, Meridiani Planum, Mars, *Geophys. Res. Lett.*, *36*(21), L21201, doi:10.1029/2009gl040734.

Yen, A. S., R. Gellert, C. Schröder, R. V. Morris, J. F. Bell, A. T. Knudson, B. C. Clark, D. W. Ming, J. A. Crisp, and R. E. Arvidson (2005), An integrated view of the chemistry and mineralogy of martian soils, *Nature*, *436*(7047), 49-54.

Zhang, Y., Z. Yang, D. Guo, H. Geng, and C. Dong (2013), Effect of Chloride Salts and Bicarbonate on Solubility of CaSO4 in Aqueous Solutions at 37°C, *Procedia Environmental Sciences*, *18*(Supplement C), 84-91, doi:https://doi.org/10.1016/j.proenv.2013.04.012.

Zipfel, J., et al. (2011), Bounce Rock—A shergottite-like basalt encountered at Meridiani Planum, Mars, *Meteoritics & Planetary Science*, *46*(1), 1-20, doi:10.1111/j.1945-5100.2010.01127.x.

Table 1. Summary of rock units at Endeavour Crater rim.

formation	unit	morphology and texture[1]	"silicate" characteristic[2]	volatile/mobile element characteristic[3]
Burns	n/a	laminated to cross-laminated medium to coarse, well-sorted sand, 1-2 mm,	low to very low Al; very high K; abraded only: high P, Fe; very high Mg	very high S; high to very high Zn
Grasberg	upper	planar, fractured, homogeneous, <100 µm	low Al, Mn; very low Mg; very high K, Fe	very high Cl, Zn, Br
	lower	devoid of structure, homogeneous, <100 µm	low Mn; very low Mg; very high K, Fe	very high Zn, Br
Shoemaker	Greeley Haven	breccia, cm-sized angular/subrounded clasts in fine-grained matrix	*(average)*	*(average)*
	Chester Lake	as for Greeley Haven; with prominent lineation of clasts	low Si	*(average)*
	Copper Cliff	as for Greeley Haven; with1-2 mm spherules, fine, anastomosing bright veins	high Ni	*(average)*
	Tisdale	as for Chester Lake	low Ca; very low Mg; high Fe; very high P, Ni	very high Zn, Br
	Murray Ridge	as for Greeley Haven	*(average)*	*(average)*
	Hueytown	as for Greeley Haven; poorer in clasts, generally smaller size	*(average)*	very high S
Matijevic	matrix	tabular, clastic, poorly laminated, <100 µm	low K, Ti; very high Si, P, Ni	low S
	spherule-rich	linear, fin-like, 2-4 mm matrix-supported spherules	very low P, Ca, Ti; high Ni; very high Si	low S
	veneer	tabular surface lamination, homogeneous	high Ni; very high P	very high Cl, Br
dark rocks	float	allochthonous blocks, homogeneous, <100 µm	low Fe; very low Mg, Cr; very high Al, Mn	low S, Cl
	Wdowiak Ridge	as for float	low Cr; very low Mg; high Na; very high Al	low S, Cl

[1]*Arvidson et al*. [2014]; *Crumpler et al*. [2015a]; *Edgar et al*. [2012]; *Grotzinger et al*. [2005, 2006]; *Squyres et al*. [2012]; this work.

[2]Elements normalized to be free of volatile/mobile elements (S, Cl, Zn and Br); compared to an average of Shoemaker formation breccias, excluding Tisdale and anomalous targets (see text).

[3]Volatile/mobile elements compared to an average of Shoemaker formation breccias, excluding Tisdale and anomalous targets.

Table 2. Compositional data for Endeavour Crater rim rocks organized by formation and measurement Sol.

Target	Sol	treatment	unit/identifier	hours	Na_2O wt%	MgO wt%	Al_2O_3 wt%	SiO_2 wt%	P_2O_5 wt%	SO_3 wt%	Cl wt%	K_2O wt%	CaO wt%	TiO_2 wt%	Cr_2O_3 wt%	MnO wt%	FeO wt%	Ni μg/g	Zn μg/g	Br μg/g
								Burns formation												
Gibraltar	2669	untreated	n/a	2.4	2.13	7.41	7.77	41.8	1.03	13.70	1.01	0.57	6.19	0.84	0.22	0.30	16.9	426	414	498
Rushall	3027	untreated	margin	23.9	2.03	6.97	7.69	40.8	0.95	13.91	0.95	0.49	7.51	0.86	0.25	0.28	17.2	379	390	210
Tawny	3352	untreated	n/a	1.5	1.83	6.80	7.58	40.7	0.96	11.93	0.81	0.54	6.54	0.82	0.27	0.27	20.9	339	322	348
Black Shoulder	3378	untreated	n/a	9.0	1.81	8.35	6.81	38.4	1.03	19.72	1.18	0.60	4.66	0.81	0.20	0.25	16.0	677	275	46
Black Shoulder2	3380	untreated	n/a	3.0	1.79	7.73	7.16	39.3	1.03	17.65	1.17	0.55	5.59	0.84	0.22	0.30	16.5	616	319	77
Black Shoulder3	3381	untreated	n/a	2.2	1.96	7.96	6.69	37.6	1.00	19.86	1.40	0.53	6.00	0.82	0.22	0.21	15.6	660	252	60
Black Shoulder	3383	abraded	n/a	2.2	1.78	8.15	5.95	36.5	1.02	22.36	1.60	0.64	4.28	0.79	0.18	0.23	16.5	612	294	40
Red Poker	3390	untreated	margin	3.1	2.07	7.14	7.50	40.6	1.04	15.53	1.05	0.57	6.16	0.85	0.20	0.29	16.8	545	538	632
Dibbler	3415	untreated	margin	10.0	2.12	6.84	8.85	44.5	0.95	8.05	0.79	0.52	7.12	0.91	0.33	0.35	18.6	378	431	222
Callitris	3445	brushed	margin	6.2	1.54	5.52	6.71	39.4	1.06	18.77	0.84	0.49	7.46	0.82	0.21	0.15	16.9	275	330	65
Cape Fairweather1	3741	untreated	margin	3.4	1.86	7.31	7.15	39.6	1.02	17.88	0.88	0.51	6.38	0.78	0.19	0.18	16.2	311	276	114
Cape Fairweather2	3742	untreated	margin	2.4	2.01	7.39	7.71	42.3	0.98	12.66	0.83	0.55	6.29	0.94	0.32	0.34	17.5	318	477	297
								Grasberg formation												
Homestake1	2764	untreated	lower, vein	1.2	1.63	4.77	4.78	25.4	0.71	32.71	1.02	0.28	22.02	0.29	0.15	0.17	6.1	21	126	77
Homestake2	2765	untreated	lower, vein	3.5	1.72	4.52	4.70	24.6	0.77	33.25	0.99	0.25	22.28	0.22	0.12	0.12	6.5	0	94	71
Homestake3	2767	untreated	lower, vein	3.6	1.50	4.67	4.91	25.8	0.85	32.03	0.85	0.28	21.78	0.29	0.13	0.16	6.8	86	143	55
Deadwood	2771	untreated	lower	3.2	2.17	5.70	8.32	44.0	1.13	9.19	1.12	0.62	6.68	0.98	0.30	0.22	19.4	410	521	301
Oostark1	2974	untreated	lower, vein	6.4	1.21	5.03	5.35	25.8	0.85	31.32	1.11	0.34	22.10	0.30	0.08	0.14	6.3	51	170	106
Oostark2	2976	untreated	lower, vein	3.0	1.61	5.02	5.27	28.0	0.82	29.67	1.08	0.31	20.67	0.27	0.09	0.17	7.0	110	165	146
Grasberg1	2990	untreated	upper	9.4	2.28	6.03	8.21	44.4	1.09	8.49	1.88	0.63	5.71	0.97	0.23	0.22	19.6	425	863	448
Grasberg2	2992	untreated	upper	4.6	2.23	5.89	8.07	43.9	1.00	9.76	1.74	0.63	6.73	0.97	0.23	0.22	18.4	372	762	343
Grasberg1	2995	brushed	upper	3.3	2.25	5.30	7.83	45.1	1.14	8.76	2.54	0.67	5.11	0.96	0.25	0.19	19.7	365	923	479
Grasberg1	3001	abraded	upper	3.9	2.57	3.93	7.24	44.0	1.24	10.12	2.74	0.73	5.85	0.92	0.23	0.19	20.0	452	955	524
Grasberg3	3006	abraded	upper	4.1	2.49	3.63	7.36	44.3	1.23	9.75	2.60	0.71	6.02	0.92	0.23	0.19	20.3	444	935	540
Mons Cupri	3022	untreated	upper	3.5	2.22	5.73	8.40	45.3	1.20	8.12	1.71	0.71	5.91	0.97	0.25	0.18	19.2	470	558	286
Gnarlaroo	3332	untreated	lower	10.5	2.11	5.49	8.56	47.2	0.89	6.30	0.98	0.69	5.03	1.07	0.30	0.18	21.1	427	514	268
Platypus	3403	brushed	lower	3.0	2.13	4.43	8.22	46.2	1.00	8.65	1.44	0.78	5.91	1.05	0.27	0.18	19.5	368	764	1004
Monjon Purple	3422	untreated	lower	3.7	2.09	4.24	8.79	47.9	1.05	6.28	1.56	0.83	4.58	1.04	0.26	0.27	20.9	268	877	444
Monjon Grey	3423	untreated	lower	4.6	2.10	4.29	9.02	48.0	0.98	5.86	1.58	0.81	4.47	1.06	0.26	0.58	20.8	412	995	352
Poverty Bush	3427	untreated	lower	6.5	2.01	4.87	7.60	42.6	1.08	13.06	1.68	0.60	7.62	0.90	0.22	0.21	17.4	134	800	685
Wally Wombat	3434	brushed	upper	2.9	2.22	4.37	8.53	45.5	1.06	9.55	1.70	0.79	6.30	0.96	0.25	0.24	18.5	196	553	293
Rosebud Canyon	3734	untreated	upper	9.0	2.17	5.33	8.37	46.0	0.85	7.82	1.59	0.70	5.75	1.03	0.26	0.12	19.8	419	718	559
								Shoemaker formation												
Timmins1	2694	untreated	Tisdale block	2.9	1.84	6.20	8.86	42.6	3.14	8.57	1.23	0.43	7.13	0.99	0.16	0.38	17.6	950	6267	779
Timmins2	2695	untreated	Tisdale block	3.2	2.16	6.04	9.97	46.2	1.22	6.01	0.93	0.50	6.78	1.05	0.27	0.38	18.0	1405	1798	722
Timmins3	2696	untreated	Tisdale block	2.0	2.54	6.19	10.10	45.4	1.20	6.50	1.00	0.53	5.88	1.05	0.23	0.23	18.8	2030	710	377
Shaw1	2699	untreated	Tisdale block	3.0	2.16	6.22	8.56	42.8	2.27	6.81	1.52	0.53	5.61	1.08	0.21	0.54	21.3	852	1813	967
Shaw2	2701	untreated	Tisdale block	2.9	2.12	6.04	8.61	45.2	2.24	5.87	1.21	0.56	5.18	1.10	0.24	0.51	20.7	770	1853	1324

Table 2 (continued). Compositional data for Endeavour Crater rim rocks organized by formation and measurement Sol.

Target	Sol	treatment	unit/identifier	hours	Na_2O wt%	MgO wt%	Al_2O_3 wt%	SiO_2 wt%	P_2O_5 wt%	SO_3 wt%	Cl wt%	K_2O wt%	CaO wt%	TiO_2 wt%	Cr_2O_3 wt%	MnO wt%	FeO wt%	Ni µg/g	Zn µg/g	Br µg/g
								Shoemaker formation												
Shaw3	2702	untreated	Tisdale block	3.2	2.09	5.90	8.16	45.6	2.01	5.89	1.27	0.62	4.83	1.01	0.27	0.46	21.4	1005	2314	1470
Salisbury1	2713	untreated	Chester Lake	13.5	2.43	7.37	9.00	44.5	1.02	6.16	1.31	0.49	6.76	1.00	0.24	0.45	19.2	474	283	78
Salisbury1	2717	brushed	Chester Lake	3.2	2.54	7.52	8.92	43.9	1.04	6.42	1.34	0.48	6.67	0.97	0.25	0.45	19.4	453	313	76
Salisbury1	2722	abraded	Chester Lake	6.0	2.74	8.81	8.82	45.5	1.00	3.09	0.87	0.41	6.77	1.09	0.25	0.48	20.1	482	246	124
Salisbury1	2726	abraded	Chester Lake	3.9	2.47	8.89	8.51	45.4	0.99	3.48	1.03	0.38	6.78	1.04	0.25	0.49	20.2	488	245	108
Geluk	2734	untreated	Chester Lake	2.9	2.69	7.43	10.10	46.1	1.13	4.84	1.04	0.46	7.12	1.15	0.27	0.63	17.0	461	244	68
Transvaal	2787	untreated	Greeley Haven	3.7	2.32	7.47	9.19	45.9	1.04	6.35	0.98	0.49	6.56	1.11	0.28	0.41	17.8	565	294	139
Boesmanskop	2798	untreated	Greeley Haven	5.9	2.37	8.86	9.35	45.5	1.22	5.74	0.99	0.54	5.79	1.05	0.22	0.43	17.8	515	348	150
Brush	2801	brushed	Greeley Haven	2.5	2.39	8.95	9.52	45.6	1.21	5.58	0.99	0.51	5.75	1.03	0.25	0.41	17.6	615	350	153
Komati	2805	untreated	Greeley Haven	8.4	2.37	8.42	9.32	44.7	1.16	5.81	0.92	0.58	6.12	1.08	0.18	0.59	18.7	461	266	229
Amboy1	2819	untreated	Greeley Haven	4.3	2.13	9.11	9.18	45.7	1.06	6.12	0.83	0.41	6.00	1.05	0.17	0.42	17.8	421	285	104
Amboy2	2834	untreated	Greeley Haven	5.5	2.19	9.08	9.17	45.7	1.07	6.10	0.85	0.42	5.89	1.01	0.18	0.44	17.8	524	280	96
Amboy3	2895	untreated	Greeley Haven	4.7	2.15	8.60	9.30	45.7	1.04	6.46	0.90	0.47	5.83	1.00	0.23	0.37	17.9	576	298	134
Amboy4	2920	untreated	Greeley Haven	3.1	2.33	7.53	9.97	46.0	1.11	5.41	0.74	0.50	7.48	1.07	0.19	0.48	17.1	306	194	103
Amboy5	2922	untreated	Greeley Haven	2.4	2.25	7.02	9.23	45.9	0.99	6.47	0.89	0.48	6.96	1.18	0.26	0.58	17.7	249	328	132
Amboy6	2924	untreated	Greeley Haven	2.8	1.77	7.44	9.12	45.9	1.11	6.73	0.94	0.45	6.99	1.03	0.23	0.41	17.7	221	317	177
Amboy7	2927	untreated	Greeley Haven	5.2	2.37	7.27	9.36	45.2	1.07	6.57	0.90	0.46	7.10	1.05	0.25	0.45	17.9	472	244	121
Amboy8	2929	untreated	Greeley Haven	3.6	2.30	7.08	9.48	46.1	0.99	6.09	0.83	0.45	6.95	1.15	0.29	0.39	17.7	447	255	108
Amboy9	2931	untreated	Greeley Haven	2.9	2.34	7.57	9.38	45.8	1.03	6.50	1.04	0.45	6.89	1.12	0.29	0.53	16.9	410	309	90
Amboy10	2935	untreated	Greeley Haven	3.4	2.24	7.37	9.25	45.5	1.03	6.68	0.98	0.47	7.05	1.16	0.26	0.51	17.4	353	295	84
Amboy11	2937	untreated	Greeley Haven	3.7	2.07	7.44	9.24	45.8	1.08	6.58	0.93	0.44	6.97	1.10	0.25	0.38	17.7	376	267	158
Amboy12	2940	untreated	Greeley Haven	7.4	2.23	7.57	9.25	44.9	1.12	6.44	0.90	0.46	6.80	1.12	0.19	0.84	18.0	523	340	119
Onaping1	3158	untreated	Copper Cliff	12.7	2.24	8.21	11.26	47.0	0.99	6.74	1.04	0.27	6.99	0.90	0.28	0.39	13.6	684	212	62
Onaping2	3162	untreated	Copper Cliff	10.5	2.18	8.57	10.83	46.5	1.02	7.27	1.07	0.29	7.00	0.86	0.27	0.42	13.6	808	245	48
Vermillion Cliffs1	3168	untreated	Copper Cliff	7.3	2.25	8.09	10.27	45.0	1.04	8.71	1.27	0.31	7.16	0.83	0.26	0.40	14.2	868	216	312
Vermillion Cliffs1	3171	untreated	Copper Cliff	8.8	2.26	8.18	10.25	45.0	1.05	8.72	1.26	0.30	7.17	0.83	0.23	0.38	14.2	844	211	326
Vermillion Lake1	3174	untreated	Copper Cliff	8.9	2.14	7.23	8.63	44.4	1.12	9.26	1.47	0.51	7.33	1.00	0.26	0.40	16.1	741	577	93
Vermillion Lake2	3177	untreated	Copper Cliff	3.3	1.93	7.28	8.60	44.4	1.14	9.27	1.52	0.50	7.27	1.01	0.29	0.38	16.2	818	600	80
Vermillion Cliffs2a	3179	untreated	Copper Cliff	5.3	2.43	8.51	10.34	46.1	1.13	6.86	1.27	0.33	6.15	0.85	0.26	0.41	15.2	916	188	229
Fecunis Lake	3214	brushed	Copper Cliff	4.5	2.36	8.33	9.91	46.3	0.93	6.77	1.50	0.39	5.90	0.87	0.27	0.33	15.9	938	228	108
Maley	3224	brushed	Copper Cliff	6.1	2.24	8.17	8.94	43.6	0.99	9.79	1.70	0.41	7.02	0.87	0.25	0.36	15.5	863	414	85
Spinifex	3463	brushed	Murray Ridge, north	4.1	2.32	8.85	8.76	45.7	1.18	5.52	0.95	0.70	6.18	1.04	0.22	0.78	17.6	537	460	706
Baobab	3468	untreated	Murray Ridge, north	4.4	2.38	7.38	9.51	46.1	1.03	6.94	0.91	0.44	6.68	1.09	0.28	0.35	16.8	377	353	137
Tangalooma	3498	untreated	Murray Ridge, north	4.9	2.04	8.58	9.43	45.7	1.15	7.82	0.74	0.23	6.29	1.09	0.20	0.36	16.2	523	118	97
MountTempest	3502	untreated	Murray Ridge, north	4.7	2.39	7.48	10.30	46.3	1.18	6.25	0.75	0.30	7.14	1.16	0.21	0.40	16.1	342	87	43
Cape Darby	3522	untreated	Murray Ridge, north	3.6	2.25	6.96	9.39	46.3	0.97	7.20	1.06	0.46	6.67	1.13	0.25	0.31	17.0	394	258	112
Cape Darby2	3535	untreated	Murray Ridge, north	4.1	2.37	7.13	9.23	45.5	0.98	7.66	1.17	0.49	6.47	1.18	0.27	0.35	17.1	394	203	110
Cape Elizabeth	3542	brushed	Murray Ridge, north	2.3	2.54	8.01	9.06	44.7	0.89	9.17	1.12	0.36	5.92	0.96	0.20	0.26	16.7	447	121	78

Table 2 (continued). Compositional data for Endeavour Crater rim rocks organized by formation and measurement Sol.

Target	Sol	treatment	unit/identifier	hours	Na_2O wt%	MgO wt%	Al_2O_3 wt%	SiO_2 wt%	P_2O_5 wt%	SO_3 wt%	Cl wt%	K_2O wt%	CaO wt%	TiO_2 wt%	Cr_2O_3 wt%	MnO wt%	FeO wt%	Ni µg/g	Zn µg/g	Br µg/g
Shoemaker formation																				
Pinnacle Island1	3546	untreated	rock alteration	3.8	1.01	12.06	5.75	28.1	1.57	25.44	0.92	0.32	5.45	0.76	0.21	1.67	16.6	661	185	262
Pinnacle Island2	3548	untreated	rock alteration	4.3	1.02	13.26	4.70	23.8	2.18	28.81	0.95	0.17	6.08	0.62	0.12	2.12	16.0	884	130	476
Pinnacle Island3	3551	untreated	rock alteration	3.8	0.86	13.00	3.48	18.1	2.37	34.51	0.66	0.14	7.66	0.44	0.10	3.48	15.1	1001	155	334
Pinnacle Island4	3560	untreated	rock alteration	3.0	1.57	9.43	7.57	36.2	1.33	16.44	0.91	0.41	5.69	0.91	0.22	1.30	17.9	354	204	144
Pinnacle Island5	3564	untreated	rock alteration	3.1	0.84	11.50	3.68	20.1	2.44	32.70	0.65	0.13	8.26	0.58	0.10	3.35	15.5	736	116	269
Green Island	3569	brushed	Murray Ridge, north	4.0	2.53	7.31	8.89	43.3	0.99	10.48	1.54	0.37	6.38	1.02	0.19	0.27	16.7	376	152	65
Stuart Island1	3573	untreated	rock alteration	4.6	0.93	12.31	5.67	27.3	1.08	28.20	0.22	0.18	5.36	0.78	0.13	1.57	16.2	547	82	40
Stuart Island2	3574	untreated	rock alteration	3.1	0.82	14.49	4.38	22.5	0.91	33.31	0.26	0.12	3.75	0.65	0.17	2.01	16.5	715	111	88
Stuart Island3	3575	untreated	rock alteration	3.3	0.53	15.58	3.60	16.1	0.98	38.21	0.21	0.09	4.05	0.57	0.14	2.85	17.0	1024	175	77
Stuart Island4	3577	untreated	rock alteration	3.8	0.86	11.65	4.87	25.6	1.40	28.95	0.33	0.28	4.85	0.65	0.16	3.37	16.8	1022	231	77
Sledge Island1	3587	untreated	Murray Ridge, north	4.1	2.48	6.35	10.44	47.6	0.82	7.74	0.65	0.28	9.65	0.63	0.21	0.30	12.8	123	138	94
Turnagain Arm	3598	brushed	Murray Ridge, north	1.7	2.32	8.05	9.10	44.5	0.95	9.37	1.36	0.36	5.98	1.04	0.20	0.28	16.4	453	114	167
Ash Meadows	3657	untreated	Murray Ridge, central	9.0	2.34	7.25	9.43	45.3	1.07	7.38	0.92	0.45	6.85	1.05	0.23	0.29	17.4	364	148	273
Bristol Well1	3664	untreated	Murray Ridge, central	9.0	2.15	6.98	8.50	42.8	1.01	11.00	0.95	0.49	9.42	0.94	0.27	0.34	15.1	312	321	75
Bristol Well2	3666	untreated	Murray Ridge, central	9.0	2.03	6.86	8.25	41.9	1.06	12.04	0.97	0.45	10.00	0.92	0.26	0.33	14.8	269	302	81
Bristol Well3	3667	untreated	Murray Ridge, central	3.7	2.03	7.14	8.89	45.4	1.00	7.36	1.05	0.50	7.17	1.15	0.27	0.36	17.6	365	361	102
Sarcobatus Flat	3671	brushed	Murray Ridge, central	5.0	2.30	7.78	8.84	44.9	1.17	7.10	1.92	0.48	6.38	0.98	0.23	0.24	17.6	293	162	98
Sarcobatus Clast1	3675	untreated	Murray Ridge, central	2.7	1.90	6.98	9.89	46.0	1.09	6.40	1.06	0.51	7.72	1.15	0.20	0.51	16.5	193	295	69
Sarcobatus Clast2	3676	untreated	Murray Ridge, central	9.0	2.00	6.21	11.23	46.2	1.61	6.12	0.83	0.44	8.17	1.41	0.14	0.27	15.3	292	151	69
Landshut	3679	untreated	Murray Ridge, central	9.0	2.21	7.14	9.08	45.0	1.00	6.88	0.88	0.52	7.24	1.09	0.34	0.36	18.2	352	331	95
Mayfield	3700	untreated	Murray Ridge, central	3.2	2.24	7.42	9.07	45.0	1.10	7.21	1.23	0.50	7.16	1.02	0.27	0.27	17.4	415	273	96
Sodaville	3707	untreated	Murray Ridge, central	12.0	2.29	7.42	9.18	45.4	1.01	6.69	1.12	0.55	6.56	1.11	0.28	0.25	18.0	391	372	71
Tuscaloosa	3708	untreated	Murray Ridge, central	3.9	2.13	8.20	9.10	45.9	1.11	7.18	1.19	0.41	6.20	1.05	0.19	0.14	17.1	371	132	117
Sodaville2	3709	untreated	Murray Ridge, central	12.0	2.22	7.34	9.25	45.6	1.07	6.56	1.24	0.52	6.75	1.12	0.24	0.23	17.7	305	325	87
Cottondale1	3848	untreated	vein	2.6	1.88	6.03	7.18	36.1	1.02	19.15	0.85	0.39	13.24	0.72	0.25	0.27	12.9	199	192	102
Cottondale2	3849	untreated	vein	2.7	1.90	6.27	7.87	39.3	1.11	15.17	0.87	0.44	10.70	0.91	0.20	0.34	14.9	254	171	98
Calera1	3851	brushed	Hueytown	9.0	2.30	7.02	8.73	43.2	1.19	10.69	0.99	0.43	6.56	1.10	0.20	0.46	17.1	483	163	78
Calera2	3853	brushed	Hueytown	2.9	2.08	6.90	8.72	43.6	1.18	10.76	0.89	0.46	6.47	1.08	0.20	0.50	17.1	420	133	86
Locust Fork	3856	brushed	Hueytown	2.3	2.32	6.88	8.93	43.4	1.19	11.04	1.11	0.42	6.28	1.10	0.20	0.50	16.6	332	161	60
Matijevic formation																				
Kirkwood	3064	untreated	spherule-rich	12.0	2.28	8.30	9.88	49.4	0.75	4.57	1.04	0.50	5.11	0.83	0.29	0.23	16.7	817	131	100
Kirkwood1	3067	brushed	spherule-rich	13.2	2.44	8.47	9.91	49.1	0.74	4.50	1.08	0.49	5.03	0.79	0.30	0.22	16.7	881	134	112
Azilda	3073	untreated	matrix	11.8	2.39	7.19	9.72	46.6	1.13	6.51	0.90	0.43	6.60	0.97	0.27	0.37	16.8	1004	207	158
Azilda1	3076	brushed	matrix	12.3	2.56	7.74	10.64	48.7	1.41	4.05	0.78	0.34	6.30	0.90	0.26	0.35	15.8	1033	151	155
Azilda2	3078	brushed	matrix	13.8	2.48	7.40	10.48	50.3	1.39	3.78	0.73	0.30	6.07	0.90	0.24	0.35	15.4	898	153	128
Azilda3	3080	brushed	matrix	10.7	2.57	7.98	10.36	47.7	1.37	4.46	0.87	0.37	6.13	0.93	0.26	0.45	16.4	976	168	112
Azilda2	3085	abraded	matrix	14.8	2.75	7.67	10.84	50.6	1.44	2.35	0.52	0.28	6.06	0.91	0.24	0.37	15.8	951	128	43
Azilda2	3087	abraded, brushed	matrix	20.9	2.55	7.91	10.60	51.2	1.50	2.47	0.53	0.28	5.98	0.87	0.24	0.36	15.4	922	134	48

Table 2 (continued). Compositional data for Endeavour Crater rim rocks organized by formation and measurement Sol.

Target	Sol	treatment	unit/identifier	hours	Na_2O wt%	MgO wt%	Al_2O_3 wt%	SiO_2 wt%	P_2O_5 wt%	SO_3 wt%	Cl wt%	K_2O wt%	CaO wt%	TiO_2 wt%	Cr_2O_3 wt%	MnO wt%	FeO wt%	Ni µg/g	Zn µg/g	Br µg/g
Matijevic formation																				
Chelmsford2	3094	brushed	veneer-rich	12.5	2.46	7.58	9.46	46.4	1.25	6.64	1.36	0.35	6.79	0.93	0.24	0.61	15.8	813	261	172
Chelmsford3	3096	brushed	veneer-rich	19.5	2.42	7.60	8.98	45.1	1.28	7.62	1.63	0.37	7.15	0.92	0.25	0.53	16.0	815	331	154
Sandcherry	3138	untreated	veneer-rich	2.8	2.24	7.59	8.33	43.5	1.24	9.06	1.76	0.42	7.58	0.88	0.23	0.36	16.6	762	445	318
Sandcherry	3144	brushed	veneer-rich	10.1	2.32	7.79	8.23	43.3	1.29	8.86	1.98	0.40	7.64	0.92	0.22	0.38	16.4	888	453	348
Sandcherry	3146	abraded	veneer-rich	18.7	2.83	8.64	9.02	44.7	1.33	6.42	1.75	0.31	7.05	0.86	0.24	0.39	16.3	914	373	332
Ortiz1	3190	untreated	vein-rich	9.0	2.21	6.44	8.69	42.6	1.17	12.14	0.90	0.33	9.81	0.78	0.25	0.54	14.0	694	167	227
Ortiz2	3192	untreated	vein-rich	9.0	2.21	6.58	9.62	46.5	1.23	7.87	0.92	0.32	7.91	0.92	0.23	0.47	15.1	723	193	157
Ortiz3	3194	untreated	vein-rich	18.0	2.18	6.60	9.14	45.3	1.14	9.43	0.84	0.35	8.47	0.89	0.27	0.48	14.8	668	198	208
Ortiz2B	3200	untreated	vein-rich	11.4	2.09	6.28	8.57	42.0	1.17	13.51	0.95	0.27	10.35	0.78	0.22	0.47	13.2	670	144	208
Fullerton	3207	untreated	spherule-rich	17.9	2.31	7.41	10.37	48.0	1.62	5.39	0.96	0.36	5.51	0.96	0.22	0.29	16.4	935	194	54
Fullerton2	3208	untreated	spherule-rich	3.1	2.21	7.99	10.51	50.3	0.87	4.54	0.84	0.35	5.96	0.98	0.26	0.28	14.8	741	199	182
Fullerton3	3209	brushed	spherule-rich	7.4	2.25	8.22	10.47	50.1	0.89	4.64	0.85	0.33	5.81	0.96	0.29	0.28	14.7	738	176	159
Lihir	3239	untreated	boxwork vein	2.9	1.66	5.89	12.92	58.4	1.19	6.25	1.58	0.37	4.03	1.16	0.32	0.16	5.8	644	304	114
Sturgeon River1	3247	untreated	spherule-rich	12.0	2.17	7.76	9.65	48.9	0.80	5.22	1.04	0.46	5.50	0.87	0.29	0.29	17.0	691	199	88
Sturgeon River2	3248	untreated	spherule-rich	10.5	2.41	8.14	10.06	48.8	0.88	4.78	0.99	0.30	5.46	0.81	0.28	0.25	16.7	724	159	53
Sturgeon River1a	3249	untreated	spherule-rich	4.9	2.15	8.24	9.87	49.4	0.74	4.67	0.88	0.41	5.17	0.81	0.32	0.24	17.0	806	155	48
Sturgeon River3	3252	abraded	spherule-rich	4.5	2.13	8.71	9.92	50.1	0.66	4.08	0.76	0.33	5.11	0.81	0.30	0.28	16.6	798	122	52
Sturgeon River3	3253	second abrasion	spherule-rich	3.1	2.21	9.29	9.61	49.5	0.59	3.32	0.47	0.36	5.11	0.81	0.36	0.29	17.9	1165	132	57
Espérance	3262	untreated	boxwork vein	13.0	2.28	6.19	11.47	53.3	1.30	7.88	2.53	0.39	5.05	1.02	0.30	0.28	7.8	606	377	213
Espérance2	3264	untreated	boxwork vein	14.5	2.16	6.49	10.36	50.6	1.26	8.93	2.61	0.45	5.80	0.99	0.28	0.27	9.6	707	484	233
Espérance3	3267	untreated	boxwork vein	24.3	2.25	6.13	11.36	53.9	1.23	7.88	2.95	0.42	4.56	1.01	0.30	0.23	7.6	670	413	142
Espérance4	3298	untreated	boxwork vein	4.9	2.28	6.12	11.72	55.5	1.15	7.28	2.97	0.39	3.93	1.04	0.28	0.23	6.9	728	361	144
Espérance5	3301	abraded	boxwork vein	11.8	2.54	4.79	14.61	61.0	1.19	3.98	2.80	0.25	2.49	0.95	0.34	0.19	4.6	633	253	58
Espérance6	3305	abraded	boxwork vein	8.9	2.25	4.73	15.37	62.5	1.14	3.28	2.32	0.24	2.14	0.93	0.34	0.19	4.4	622	238	35
dark-rock float/ejecta																				
Tick Bush	3392	untreated	dark-rock float	6.7	2.89	5.65	12.47	48.2	1.21	4.49	0.98	0.57	7.16	1.08	0.11	1.00	14.0	913	696	51
Tick Bush2	3396	untreated	dark-rock float	5.0	3.10	4.90	13.97	49.8	1.27	2.67	0.67	0.49	7.29	1.17	0.10	1.20	13.2	985	670	40
Augustine	3603	untreated	dark-rock float	4.2	2.15	7.95	11.00	46.7	0.98	4.66	0.53	0.32	7.09	1.20	0.21	0.29	16.9	449	101	15
Point Bede	3616	untreated	dark-rock float	10.5	2.19	7.77	11.01	46.1	0.65	5.35	0.61	0.28	6.77	1.23	0.20	0.31	17.5	438	107	58
Mount Edgecumbe	3753	untreated	dark-rock ejecta/float	10.5	2.67	6.71	11.42	46.7	1.16	4.66	0.68	0.45	7.63	1.33	0.21	0.34	15.9	794	252	56
Hoover	3796	brushed	dark-rock ejecta/float	9.0	2.04	6.54	7.56	42.2	1.19	9.71	1.61	0.54	7.72	0.97	0.22	0.34	19.2	549	666	44
Lipscomb-Victory1	3800	untreated	dark-rock ejecta/float	7.5	2.65	6.15	11.99	47.7	1.29	4.02	0.64	0.41	7.53	1.21	0.19	0.30	15.9	116	112	20
Lipscomb-Victory2	3802	untreated	dark-rock ejecta/float	9.0	2.72	6.09	12.30	47.8	1.31	3.73	0.61	0.38	7.46	1.31	0.17	0.30	15.8	152	124	31
Lipscomb-Margaret	3809	untreated	dark-rock ejecta/float	7.5	2.82	6.05	12.56	48.2	1.17	4.02	0.46	0.39	7.32	1.21	0.17	0.35	15.2	303	103	17
Lipscomb-Margaret	3812	brushed	dark-rock ejecta/float	2.5	2.75	6.23	12.56	48.4	1.20	3.72	0.42	0.36	7.35	1.23	0.18	0.36	15.2	289	111	20
Birmingham	3819	untreated	dark-rock ejecta/float	7.5	2.46	6.47	11.23	46.7	1.28	4.93	0.98	0.47	7.56	1.15	0.15	0.34	16.1	452	262	153

Table 3. Average compositions of Grasberg formation lower and upper units and vein targets, plus the ratio of upper unit to lower unit.

		lower unit		upper unit		vein		upper/lower	
		ave	std	ave	std	ave	std	ratio	±
number		5		5		5			
Na_2O	wt%	2.10	0.06	2.23	0.03	1.53	0.20	1.058	0.034
MgO	wt%	4.95	0.64	5.44	0.60	4.80	0.22	1.106	0.196
Al_2O_3	wt%	8.30	0.45	8.24	0.25	5.00	0.29	1.002	0.058
SiO_2	wt%	45.6	2.2	45.0	0.8	25.9	1.3	0.988	0.052
P_2O_5	wt%	1.03	0.09	1.06	0.12	0.80	0.06	1.011	0.153
SO_3	wt%	8.69	2.78	8.75	0.77	31.8	1.4	1.006	0.337
Cl	wt%	1.35	0.29	1.86	0.35	1.01	0.10	1.273	0.287
K_2O	wt%	0.70	0.10	0.69	0.06	0.29	0.03	0.985	0.168
CaO	wt%	5.96	1.23	5.92	0.55	21.8	0.6	1.020	0.222
TiO_2	wt%	1.01	0.07	0.98	0.03	0.28	0.03	0.972	0.073
Cr_2O_3	wt%	0.27	0.03	0.25	0.01	0.11	0.03	0.910	0.113
MnO	wt%	0.21	0.03	0.20	0.04	0.15	0.02	0.922	0.265
FeO	wt%	19.7	1.5	19.2	0.6	6.53	0.37	0.970	0.080
Ni	µg/g	321	122	375	95	53	45	1.172	0.553
Zn	µg/g	695	167	729	153	140	31	0.994	0.308
Br	µg/g	541	307	401	111	91	36	0.714	0.459

Table 4. Average or representative compositions of Matijevic formation lithologies.

		Azilda matrix		Sturgeon River3 spherule-rich		Sandcherry veneer-rich		Chelmsford veneer-rich		veneer calc.*	Ortiz2B vein-rich	
		ave	std	meas.	±	meas.	±	ave	±		meas.	±
number		5						2				
Na_2O	wt%	2.58	0.08	2.21	0.25	2.32	0.21	2.44	0.12	1.98	2.09	0.19
MgO	wt%	7.75	0.04	9.29	0.15	7.79	0.10	7.59	0.05	10.15	6.28	0.08
Al_2O_3	wt%	10.6	0.1	9.61	0.16	8.23	0.10	9.19	0.06	—	8.57	0.11
SiO_2	wt%	49.5	0.2	49.5	0.5	43.3	0.4	45.7	0.2	25.8	42.0	0.4
P_2O_5	wt%	1.42	0.03	0.59	0.08	1.29	0.08	1.27	0.05	1.49	1.17	0.08
SO_3	wt%	3.09	0.02	3.32	0.08	8.86	0.10	7.13	0.05	20.70	13.5	0.1
Cl	wt%	0.64	0.01	0.47	0.02	1.98	0.03	1.49	0.01	3.21	0.95	0.02
K_2O	wt%	0.31	0.02	0.36	0.06	0.40	0.06	0.36	0.04	0.89	0.27	0.06
CaO	wt%	6.10	0.02	5.11	0.06	7.64	0.06	6.98	0.03	13.4	10.3	0.1
TiO_2	wt%	0.90	0.03	0.81	0.09	0.92	0.07	0.93	0.04	1.12	0.78	0.06
Cr_2O_3	wt%	0.25	0.01	0.36	0.04	0.22	0.03	0.25	0.02	0.17	0.22	0.03
MnO	wt%	0.37	0.01	0.29	0.02	0.38	0.01	0.56	0.01	0.44	0.47	0.01
FeO	wt%	15.8	0.1	17.9	0.2	16.4	0.1	15.9	0.1	20.3	13.2	0.1
Ni	µg/g	952	20	1165	76	888	50	814	30	884	670	44
Zn	µg/g	144	4	132	20	453	16	300	7	995	144	10
Br	µg/g	92	7	57	19	348	19	162	11	644	208	17

*From *Clark et al*. [2016].

Table 5. Average compositions of Shoemaker formation units and the formational average.

		Copper Cliff		Chester Lake		Tisdale		Greeley Haven		Murray Ridge, north[1]		Murray Ridge, central		Hueytown		Shoemaker[2]	
		ave	std	ave	std	ave	std	ave	std	ave	std	ave	std	ave	std	ave	std
number		9		5		6		16		8		10		3		51	
Na_2O	wt%	2.22	0.14	2.57	0.13	2.15	0.23	2.24	0.16	2.35	0.16	2.17	0.15	2.23	0.13	2.27	0.18
MgO	wt%	8.06	0.49	8.00	0.78	6.10	0.13	7.92	0.76	7.61	0.55	7.29	0.52	6.93	0.07	7.72	0.69
Al_2O_3	wt%	9.89	0.96	9.07	0.60	9.04	0.80	9.33	0.20	9.36	0.43	9.40	0.71	8.79	0.12	9.39	0.62
SiO_2	wt%	45.4	1.1	45.1	0.9	44.6	1.5	45.6	0.4	45.3	1.1	45.5	0.4	43.4	0.2	45.3	0.9
P_2O_5	wt%	1.05	0.07	1.04	0.06	2.01	0.73	1.08	0.07	1.02	0.10	1.12	0.18	1.19	0.01	1.08	0.11
SO_3	wt%	8.16	1.23	4.80	1.51	6.61	1.03	6.23	0.41	8.11	1.43	6.89	0.43	10.83	0.18	7.12	1.67
Cl	wt%	1.34	0.22	1.12	0.20	1.19	0.21	0.91	0.08	1.08	0.28	1.15	0.31	1.00	0.11	1.09	0.25
K_2O	wt%	0.37	0.09	0.44	0.05	0.53	0.06	0.47	0.04	0.38	0.09	0.49	0.04	0.43	0.02	0.44	0.08
CaO	wt%	6.89	0.50	6.82	0.18	5.90	0.90	6.57	0.57	6.44	0.40	7.02	0.61	6.44	0.14	6.71	0.53
TiO_2	wt%	0.89	0.07	1.05	0.07	1.05	0.04	1.08	0.06	1.08	0.07	1.11	0.12	1.10	0.01	1.05	0.11
Cr_2O_3	wt%	0.26	0.02	0.25	0.01	0.23	0.04	0.23	0.04	0.22	0.04	0.24	0.06	0.20	0.01	0.24	0.04
MnO	wt%	0.39	0.03	0.50	0.07	0.41	0.11	0.48	0.12	0.32	0.05	0.29	0.10	0.49	0.02	0.40	0.12
FeO	wt%	15.0	1.1	19.2	1.3	19.6	1.7	17.7	0.4	16.6	0.4	17.3	0.8	16.9	0.3	17.1	1.4
Ni	µg/g	831	80	471	15	1169	476	440	116	413	58	334	65	412	76	485	186
Zn	µg/g	321	166	266	31	2459	1939	292	41	176	90	255	96	152	16	261	103
Br	µg/g	149	109	91	24	940	405	131	37	101	40	108	60	75	13	118	61

[1]Excluding anomalous targets Spinifex and Sledge Island.

[2]Excluding anomalous targets Spinifex and Sledge Island, and the Tisdale block.

Figure captions

Figure 1: HiRISE-based mosaic showing Endeavour Crater (upper right). Locator images showing rover track (courtesy of T. Parker), APXS target sites and geographic names used in the text. Close up images cropped from HiRISE image file ESP_018846_1775_RED.

Figure 2: Portion of the geologic map (a) and cross section (b) of the Meridiani Planum region surrounding the Mars Exploration Rover *Opportunity* area of investigation [*Hynek and Di Achille*, 2017], and the schematic stratigraphy of the region explored by *Opportunity* (c) (modified after [*Crumpler et al*., [2015a]). Unit key only covers those discussed in the text. Cross section vertical exaggeration is ~78×. White dotted circle – approximate location of Miyamoto Crater rim; yellow dotted arcs – approximate inner rim crest and first ring of multiring basin that underlies Meridiani Planum [after *Newsom et al*., 2003].

Figure 3: a. Portion of the sols 3387-3389 site 179/position 0 Navcam mosaic showing dark-rock float on Solander Point; Murray Ridge in the background. Tick Bush is ~20 cm across. b. Portion of the Sol 3609 Pancam L257 false-color mosaic showing dark-rock float on the McClure-Beverlin Escarpment of Murray Ridge. Labeled boulders A and are 16 and 18 cm across at their bases. c. Portion of the Sol 3750 L257 Pancam false-color mosaic showing the dark cap-rock on the northeast tip of Wdowiak Ridge. (The left Pancam filters numbers 2, 5 and 7 are centered on 753, 535 and 432 nm. Unless otherwise noted, all Pancam false-color images used are based on these filters.)

Figure 4: Pancam false-color images showing examples of macrotextures of Grasberg formation targets: a. Grasberg, upper unit (portion of Sol 3000 image), Pancam left filters 4, 5 and 6 centered on 601, 535 and 482 nm. Arrows indicate possible fine Ca-sulfate veins; b. Rosebud Canyon, upper unit (Sol 3734); c. Monjon (Sol 3425), lower unit. Boxes indicate the locations of MI frames for the purple (upper box) and grey (lower box) targets discussed in the text; d. Homestake (Sol 2769), vein in lower unit; e. Poverty Bush, lower unit, showing fine-scale laminations (arrows) (Sol 3426).

Figure 5: Microscopic Imager mosaics showing examples of microtextures of Grasberg formation targets: a. Grasberg, upper unit (Sol 3006, abraded, illuminated from upper right); b. Wally Wombat, upper unit (Sol 3434, brushed, fully shadowed); c. Monjon Purple, lower unit (Sol 3422, untreated, illuminated from upper right); d. Poverty Bush, lower unit (Sol 3427, untreated, fully shadowed). Scale bars are 1 cm.

Figure 6: Pancam false-color images showing examples of macrotextures of Matijevic formation outcrops: a. Fine-grained bright lithology showing matrix (M), patches of dark veneer (Vr), bright veins (Vn) locally traceable below the veneer (white arrows, inset), and rare spherules (S) (Sol 3203); b. Outcrop of ledge-forming spherule-rich lithology (portion of Sol 3062 mosaic).

Figure 7: Microscopic Imager mosaics showing examples of microtextures of Matijevic formation targets: a. Fullerton3 showing matrix, scattered spherules and bright veins in the top right (Sol 3209, brushed, illuminated from upper left); b. Ortiz2B with the highest vein concentration targeted (center of circles) (Sol 3200, untreated, fully shadowed); c. Chelmsford3 showing dark veneer on top of bright matrix (Sol 3096, brushed, illuminated from upper left); d.

Spherule-rich target Sturgeon River3 (Sol 3251, very light abrasion – arrows, illuminated from upper left). Scale bars are 1 cm. On a-c, solid circles are the 3.8 cm inside diameter of the APXS; dotted circles are the approximate regions from which 75% of the APXS response signal is derived.

Figure 8: Pancam false-color images showing examples of macrotextures of Shoemaker formation outcrops: a. Vermilion on Matijevic Hill, Copper Cliff member (Sol 3156), arrows mark several clasts standing in relief above the surface; b. Mpangeni on Shoemaker Ridge, Greeley Haven member (Sol 2786), Pancam left filters 2, 4 and 6 centered on 753, 601, and 482 nm; c. Kangaroo Paw on Murray Ridge (Sol 3466); d. Bristol Well at Pillinger Point on Murray Ridge showing bright $CaSO_4$ vein (Sol 3669); e. Sarcobatus at Pillinger Point on Murray Ridge showing targets Flat (brushed), Clast1 and Clast2 (Sol 3676); f. Hueytown on Cape Tribulation showing brushed outcrop targets Calera and Locust Fork, and vein target Cottondale (Sol 3868).

Figure 9: Microscopic Imager mosaics (except c) showing examples of microtextures of Shoemaker formation targets: a. Onaping from the Copper Cliff outcrop, Matijevic Hill (Sol 3158, untreated, illuminated from top); b. Green Island from Cook Haven on Murray Ridge (Sol 3569, brushed, illuminated from bottom); c. Portion of Mount Tempest image showing large clast with texture suggesting bright clasts (arrows) in dark matrix, from the Moreton Island outcrop, Murray Ridge (Sol 3502, untreated, fully shadowed); d. Cottondale $CaSO_4$ vein at Hueytown (between arrows) on Cape Tribulation (Sol 3848, untreated, illuminated from left). Bright vertical streaks in lower right of a are artifacts caused by saturation of specular reflections. Scale bars are 1 cm.

Figure 10: Pancam false-color images of dark rocks: a. Tick Bush from Solander Point (Sol 3391); b. Concentration of dark-rock float between Cook Haven and the McClure-Beverlin Escarpment, A - Augustine and, c - possible columnar-jointed (hexagonal prism) block (Sol 3601); c. Dark-rock ejecta from Ulysses crater, Wdowiak Ridge, H – Hoover and, f - dark flakes commonly observed on local rocks (Sol 3793); d. Birmingham from Wdowiak Ridge in the Ulysses crater ejecta field (Sol 3814).

Figure 11: Microscopic Imager mosaics showing examples of microtextures of dark rocks: a. Tick Bush from Solander Point (Sol 3392, untreated, fully shadowed); b. Point Bede from near Cook Haven (Sol 3616, untreated, illuminated from upper right); c. Hoover from Wdowiak Ridge (Sol 3795, brushed, illuminated from upper right); d. Crimson Tide target on rock Birmingham from Wdowiak Ridge, arrows indicate grains or clasts (Sol 3819, untreated, illuminated from right). Scale bars are 1 cm.

Figure 12: Compositional data for Grasberg formation targets compared to Burns formation, dark sands and bright soils. “Burns; margin” refers to targets from near the contact with the Grasberg formation; see text. Symbols with “×” were brushed; those with “•” were abraded. Arrow shows progression of analyses of untreated, brushed and abraded Grasberg1. Panel b expands the ordinate of a to show details of the non-vein targets. Compositionally anomalous Grasberg (red) and Burns margin (black) targets are labeled; G and P refer to Monjon Grey and Purple. Circled abraded Burns formation analyses are for Guadalupe and Lion Stone (see discussion in Section 6.6).

Figure 13: Element ratio diagram for Grasberg1 untreated and brushed targets normalized to the abraded target; u – untreated, b – brushed, a – abraded. Y-axis is log scale.

Figure 14: Element ratio diagrams for Matijevic formation veneer-rich (a) and spherule-rich (b) targets relative to matrix composition (average Azilda, Table 4). In a, coating is the calculated veneer composition from *Clark et al*. [2016]. In b, Fullerton3 is a different matrix target. Y-axis is log scale.

Figure 15: Compositional data for Matijevic formation targets compared to Burns and Grasberg (G) formation targets, abraded Adirondack-class (A) basalts from Gusev Crater, dark sands and bright soils. Stars are the best representations of the Matijevic matrix composition (Table 4); arrows point towards veneer-rich targets.

Figure 16: Results of Agglomerative Hierarchical Cluster Analysis on Matijevic, Burns and Grasberg formation targets, dark sands and bright soils for all elements (a, b) and excluding S, Cl, Zn and Br (c, d). Panels b and d show details of cluster 4.

Figure 17: Compositional data for Shoemaker formation targets compared to Burns formation targets, fields Grasberg (G) and Matijevic (M) formations, dark sands and bright soils.

Figure 18: Element ratio diagrams for clast/host pairs; u = untreated, b = brushed, a = abraded. Dashed lines in panel b show the maximum and minimum measurements on the Amboy outcrop ratioed to the median values. Ratios >1 are elements with *lower* concentrations in the host targets. The Y axis are log scales and are the same on all panels.

Figure 19: Compositional data for Shoemaker formation clast and bulk rock targets compared to Transvaal, multiple analyses of Greeley Haven target Amboy, fields for Matijevic formation matrix (M_m) and spherule-rich (M_s) targets, abraded Adirondack-class basalt targets (A), dark sands, and bright soils. Symbols with "×" were brushed; those with "•" were abraded. Dotted envelope – cluster 1 rocks; solid envelope – cluster 2 rocks (see text). Sarcobatus Clast1 and Clast2 are labeled.

Figure 20: a. Results of Agglomerative Hierarchical Cluster Analysis on Greeley Haven member targets, dark sand and bright soil using all elements. b. Target locations color coded by cluster on a portion of the Greeley Haven Pancam mosaic (Sol 2803); locations of images shown in panels c - e are indicated. Microscopic Imager images of: c. Boesmanskop (Sol 2800, untreated, fully shadowed); d. Amboy 4 (Sol 2921, untreated, illuminated from top); e. Amboy 12 (Sol 2940, untreated, illuminated from top). Scale bar in d is 0.5 cm and also applies to c and e.

Figure 21: CaO vs. SO_3 for vein-rich targets compared to fields for host lithologies for (a) the Grasberg formation, (b) the Murray Ridge, Bristol Well targets, (c) Hueytown fracture zone, and (d) the Matijevic formation. Labeled fields are: G_L – Grasberg formation, lower unit; H – Shoemaker formation, Hueytown; M_m – Matijevic formation matrix; MR – Shoemaker formation, Murray Ridge. Dark sands and bright soils are shown for comparison. Solid lines are mixing lines between outcrop host and pure $CaSO_4$ veins (see text). Star in panel c is a mixture of Hueytown outcrop and dark sand, and the dotted line is a mixing line between this composition and $CaSO_4$; see text. Dotted line in d is a regression through the Matijevic formation vein-rich targets (see text).

Figure 22: Bristol Well targets on: a. Pancam false-color image (Sol 3669); and b. MI mosaic (Sol 3664, untreated, fully shadowed). Approximate centers and APXS fields of view of the three Bristol Well targets are shown in b.

Figure 23: Compositional data for dark-rock Wdowiak Ridge and float targets compared to Gusev Crater basalts, dark sands, bright soils and fields for Endeavour rim lithologies. Abbreviations are: G – Grasberg formation; M – Matijevic formation; S_Y – Shoemaker formation on Cape York; S_T – Shoemaker formation, Tisdale block; S_M – Shoemaker formation on Murray Ridge (individual labeled point is the anomalous Sledge Island target); T – Tick Bush, H – Hoover. Dashed arrows: Lipscomb-Margaret (rock) to Lipscomb-Victory (flake) targets; see text.

Figure 24: FeO vs. MnO for clasts, anomalous or altered targets compared to fields for host lithologies and abraded Adirondack-class basalts. Panel b expands the x axis to highlight details of low-MnO targets. Abbreviations in a are: CY – Shoemaker formation, Cape York; G – Grasberg formation; M – Matijevic formation; MR – Shoemaker formation on Murray Ridge. Abbreviations in b are: A – Adirondack-class basalts; M_m – Matijevic formation matrix; M_s – Matijevic formation spherule-rich; S_{CC} – Shoemaker formation, Copper Cliff member; S_{CL} – Shoemaker formation Chester Lake member; S_{GH} – Shoemaker formation Greeley Haven member; S_T – Shoemaker formation, Tisdale block. Line labeled Mars is average Fe/Mn of abraded Adirondack-class basalts; dotted lines in b are ±10% on the average, and are merely meant to aid in visualizing the scale of departure of the Endeavour Crater rim rocks from the average. Some symbols from panel a legend carry over to panel b.

Figure 25: S vs. Fe/Mn for select lithologies. Blue arrows show trends from host towards $CaSO_4$ veins; see text. Dashed lines show trends of higher Fe/Mn with slight S increase in some outcrop lithologies (Matijevic spherule-rich; Grasberg) and lower Fe/Mn with large S increase in some vein-rich and altered targets. Abbreviations in a are: Dw – Deadwood outcrop target; G – Grasberg formation; Hs – Homestake vein target. Abbreviations in b are: A – abraded Adirondack-class basalts; H – Shoemaker formation, Hueytown; m – martian meteorites; M_m – Matijevic formation matrix; M_s – Matijevic formation spherule-rich; MR – Shoemaker formation, Murray Ridge; S_{CC} – Shoemaker formation, Copper Cliff member; S_{CL} – Shoemaker formation Chester Lake member; S_{GH} – Shoemaker formation Greeley Haven member; S_T – Shoemaker formation, Tisdale block. Line labeled Mars is average Fe/Mn of abraded Adirondack-class basalts.

Figure 26: Element/Si vs. Ca/Si mole-ratio diagrams for $CaSO_4$ vein-rich targets compared to host outcrop and unit fields. Abbreviations in a are: G_L – Grasberg formation, lower unit; H – Shoemaker formation, Hueytown; M_m – Matijevic formation matrix; MR – Shoemaker formation, Murray Ridge. Symbols for host outcrop are Deadwood target (Grasberg), average Matijevic matrix (Table 4), Bristol Well on Murray Ridge, and mixed Hueytown outcrop and dark sand.

Figure 1.

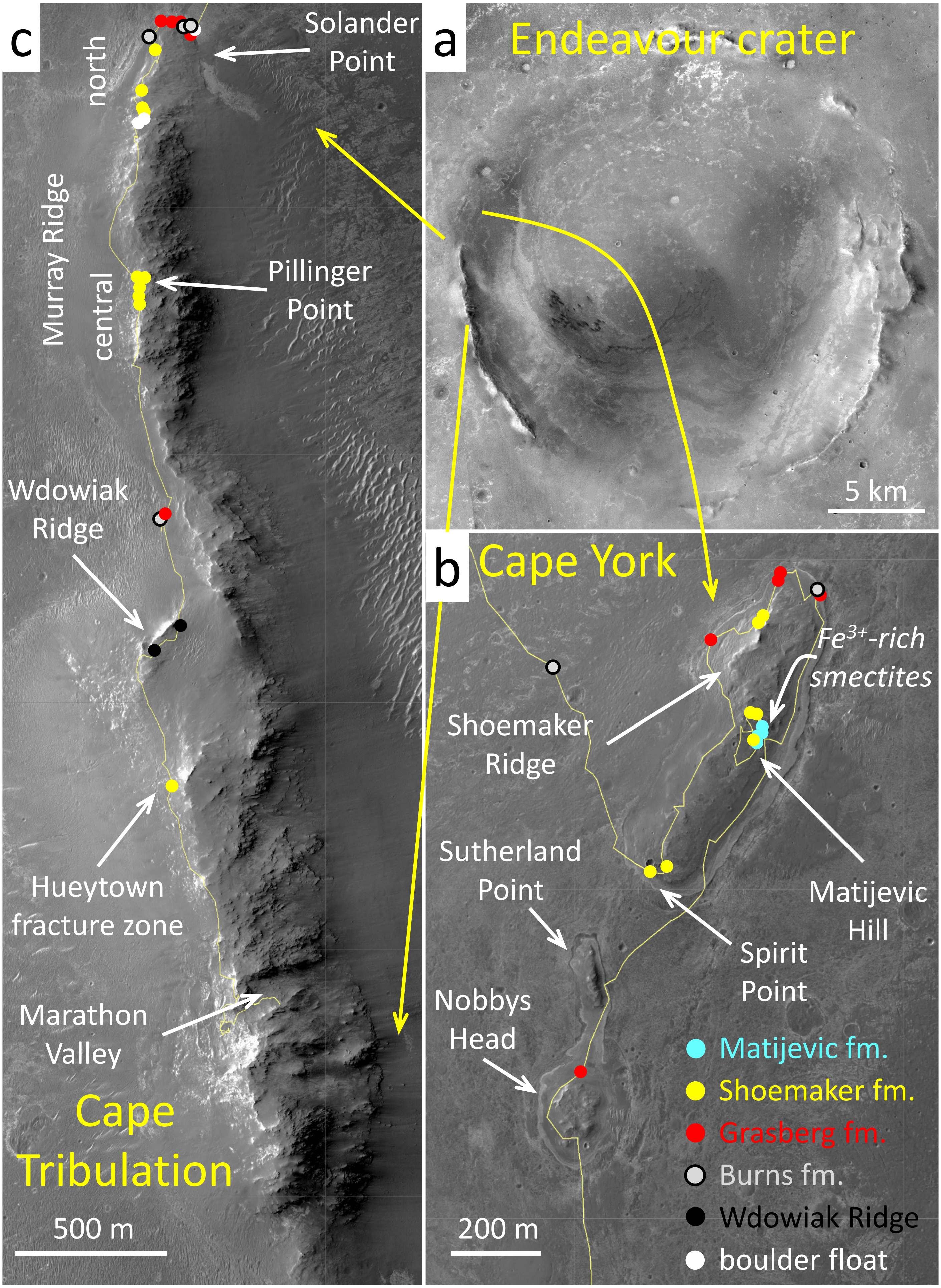
c
north
Solander
Point
Murray Ridge
central
Pillinger
Point
Wdowiak
Ridge
Hueytown
fracture zone
Marathon
Valley
Cape
Tribulation
500 m
a
Endeavour crater
5 km
b
Cape York
Fe3+-rich
smectites
Shoemaker
Ridge
Sutherland
Point
Matijevic
Hill
Spirit
Point
Nobbys
Head
Matijevic fm.
Shoemaker fm.
Grasberg fm.
Burns fm.
Wdowiak Ridge
boulder float
200 m

Figure 2.

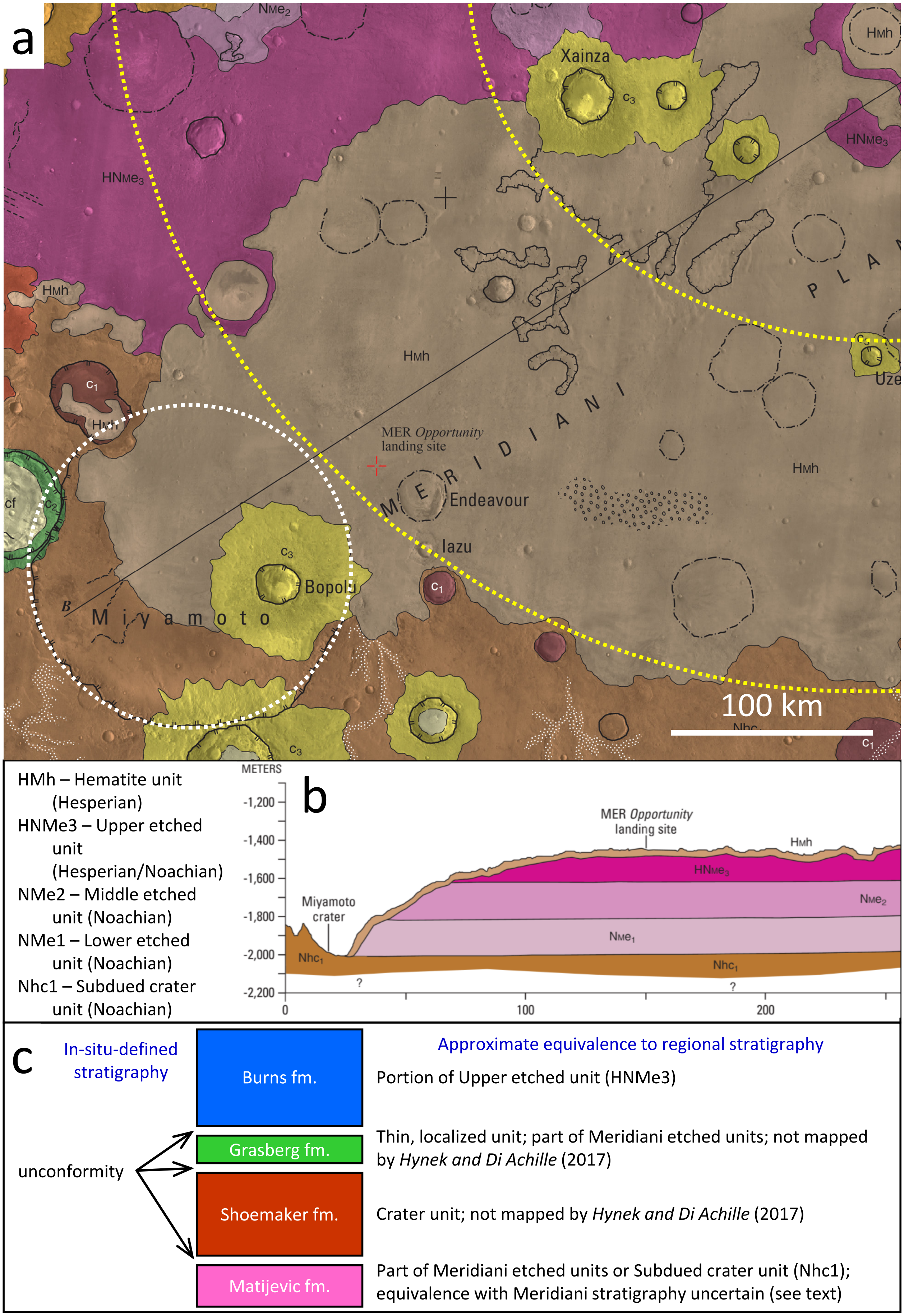
a
NMe2
Xainza
c3
HMh
HNMe3
HNMe3
PLA
HMh
HMh
c1
HMh
Uze
MER Opportunity
landing site
MERIDIANI
Endeavour
HMh
cf
c2
Iazu
c3
Bopolu
c1
B
Miyamoto
100 km
c3
c1
HMh – Hematite unit (Hesperian)
HNMe3 – Upper etched unit (Hesperian/Noachian)
NMe2 – Middle etched unit (Noachian)
NMe1 – Lower etched unit (Noachian)
Nhc1 – Subdued crater unit (Noachian)
b
METERS
-1,200
-1,400
-1,600
-1,800
-2,000
-2,200
0
100
200
MER Opportunity
landing site
HMh
HNMe3
NMe2
NMe1
Nhc1
Miyamoto
crater
Nhc1
?
?
c
In-situ-defined stratigraphy
Approximate equivalence to regional stratigraphy
Burns fm.
Portion of Upper etched unit (HNMe3)
Grasberg fm.
Thin, localized unit; part of Meridiani etched units; not mapped by Hynek and Di Achille (2017)
unconformity
Shoemaker fm.
Crater unit; not mapped by Hynek and Di Achille (2017)
Matijevic fm.
Part of Meridiani etched units or Subdued crater unit (Nhc1); equivalence with Meridiani stratigraphy uncertain (see text)

Figure 3.

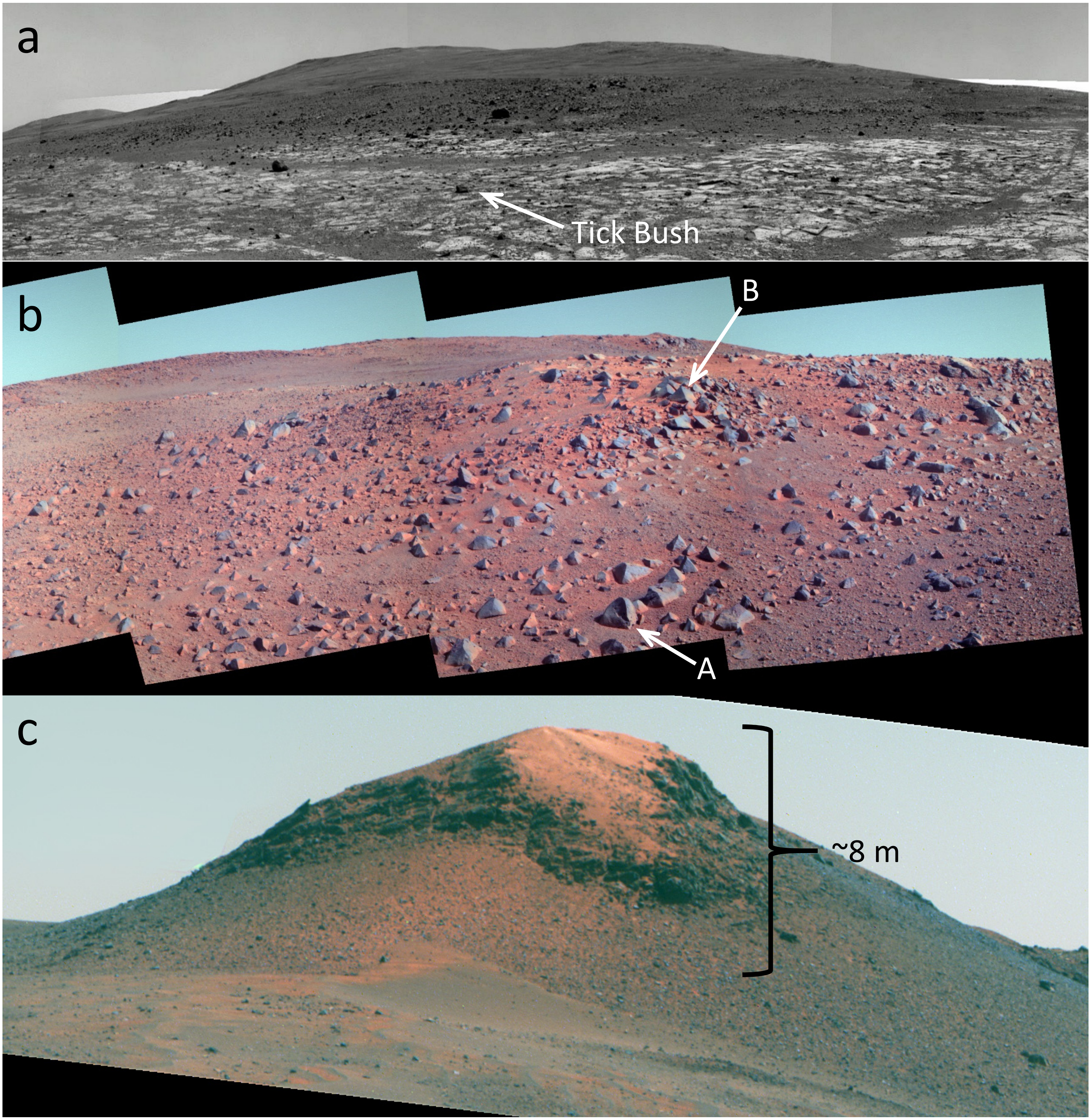
a
Tick Bush
b
B
A
c
~8 m

Figure 4.

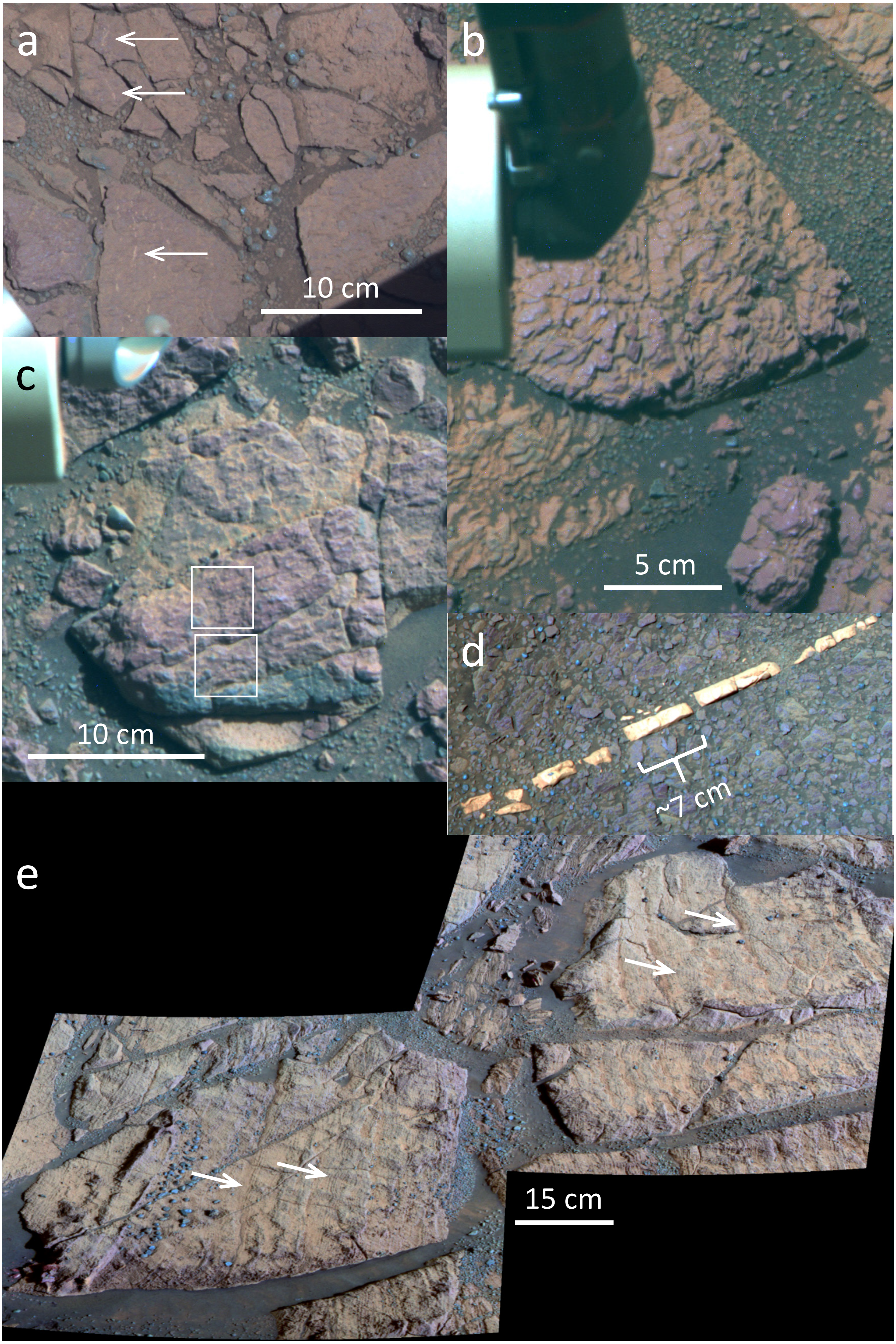
a
10 cm
b
5 cm
c
10 cm
d
~7 cm
e
15 cm

Figure 5.

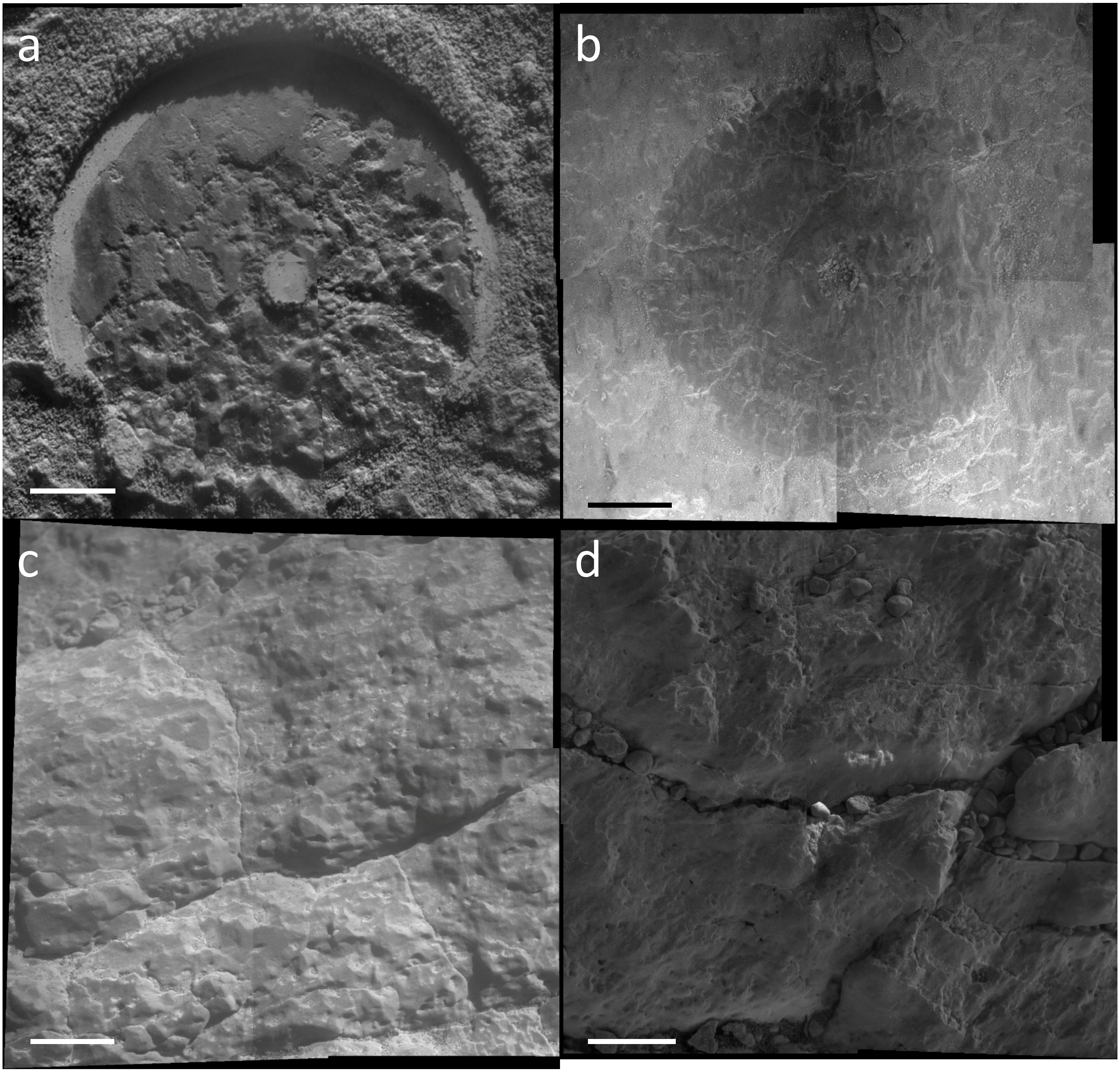

a
b
c
d

Figure 6.

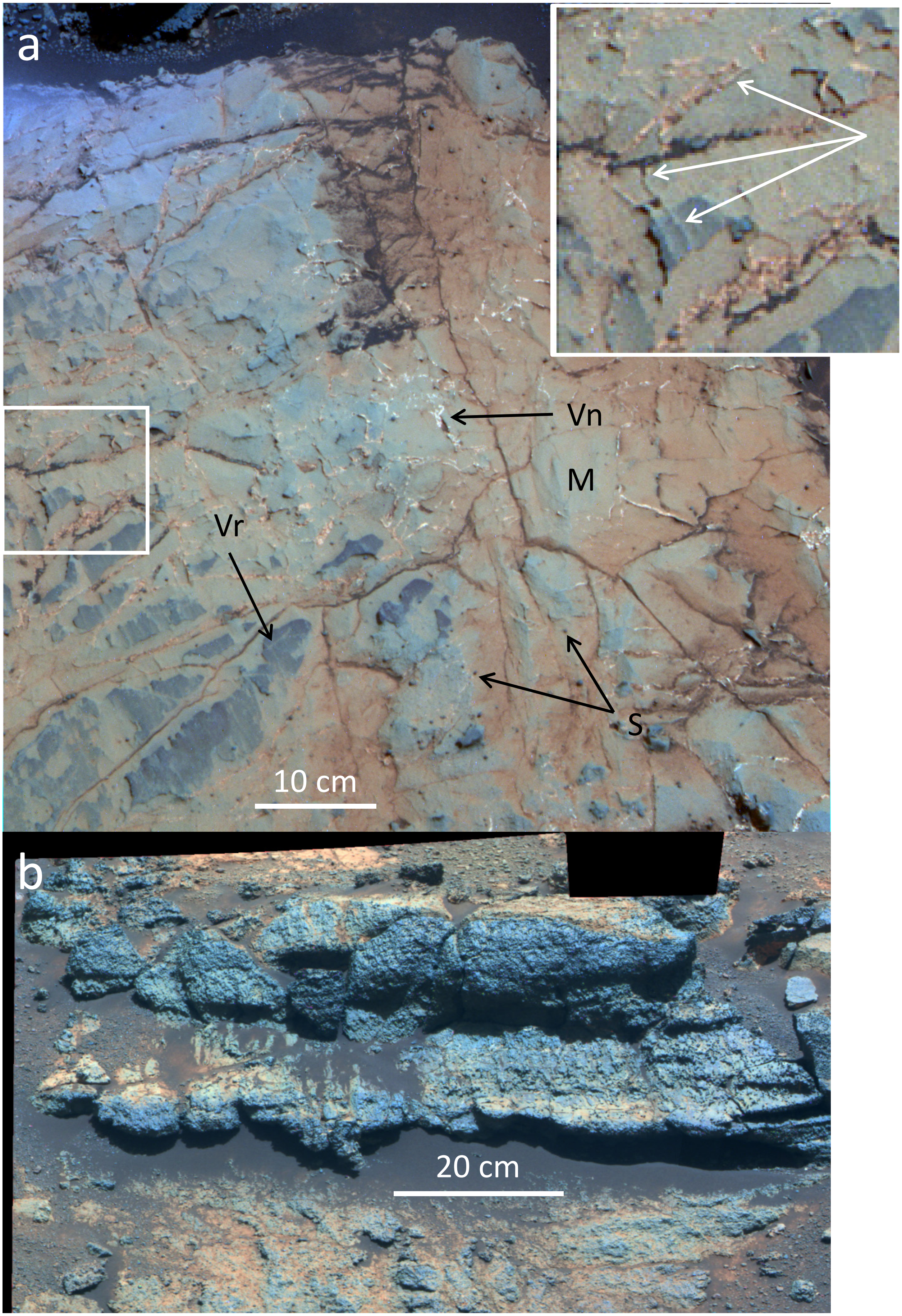

a
Vn
M
Vr
S
10 cm
b
20 cm

Figure 7.

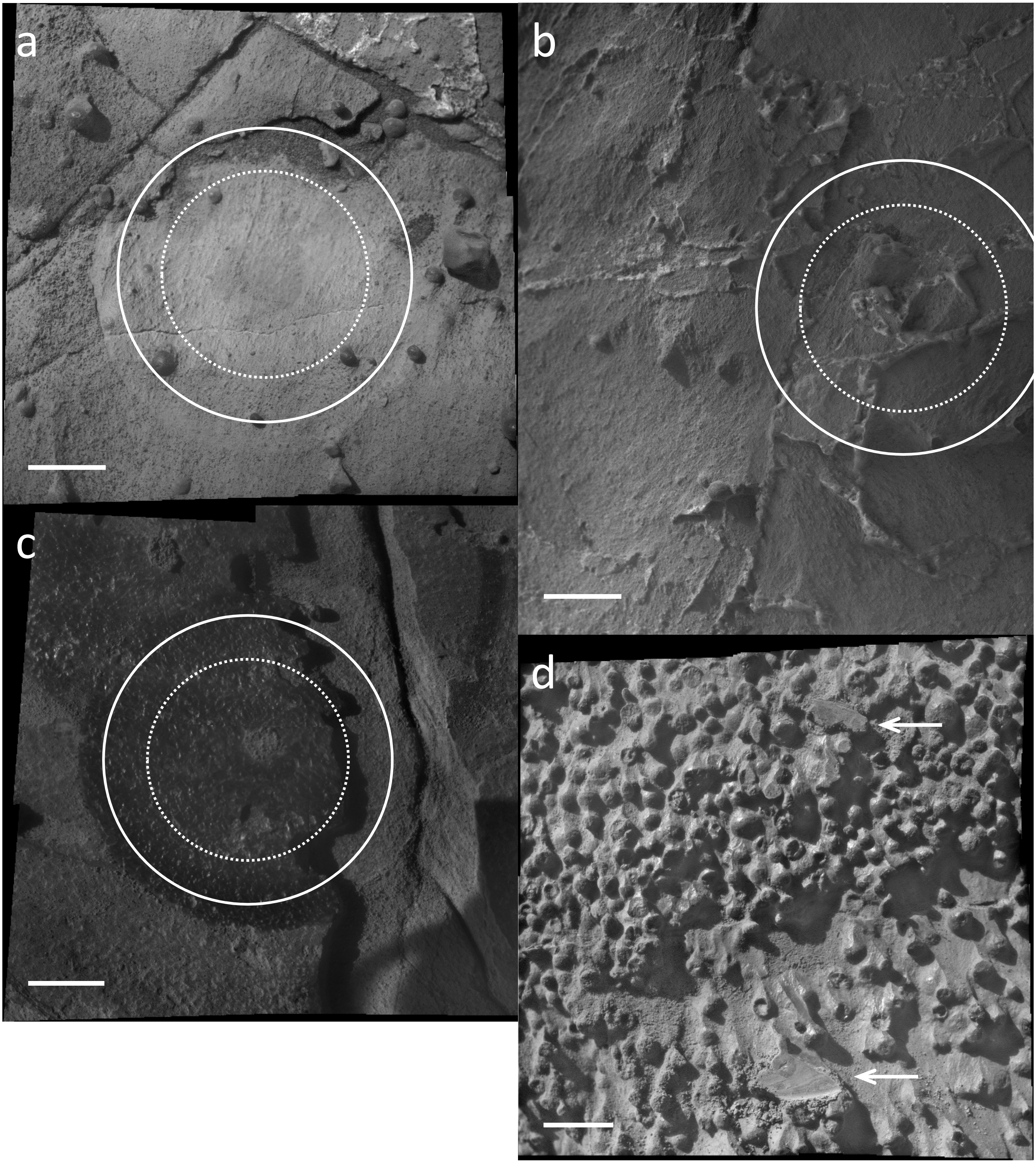
a
b
c
d

Figure 8.

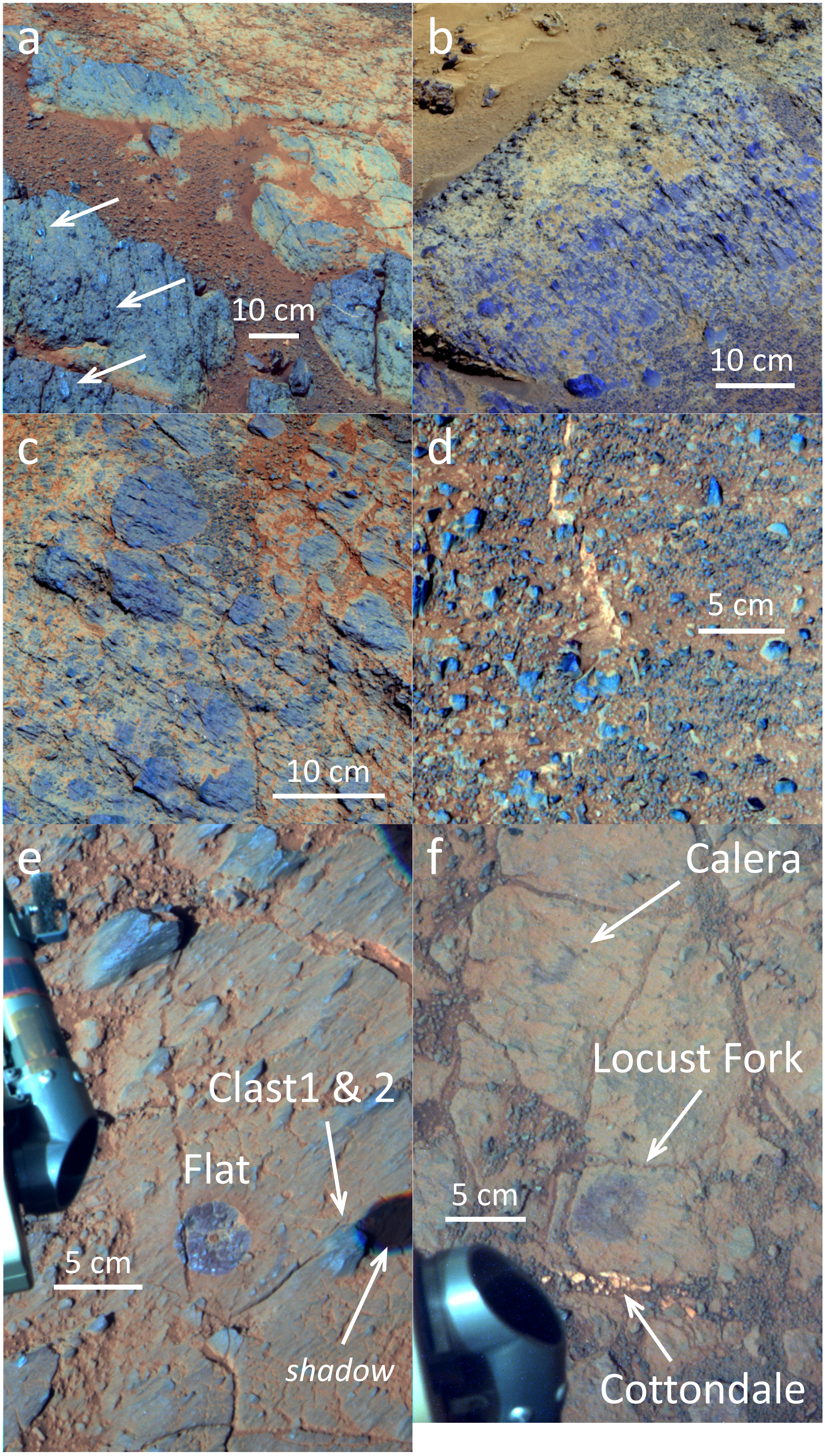
a
10 cm
b
10 cm
c
10 cm
d
5 cm
e
Clast1 & 2
Flat
5 cm
shadow
f
Calera
Locust Fork
5 cm
Cottondale

Figure 9.

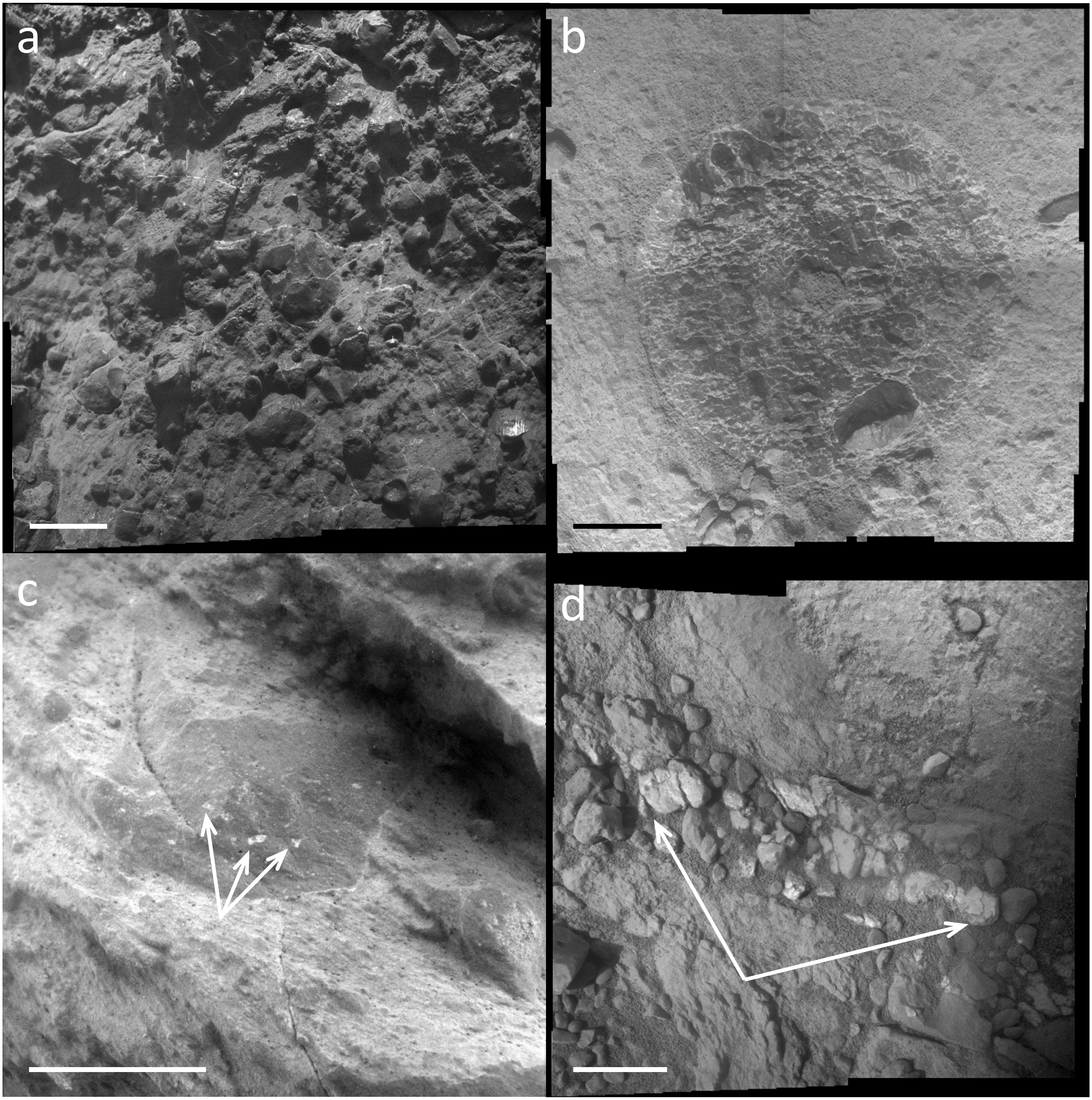
a
b
c
d

Figure 10.

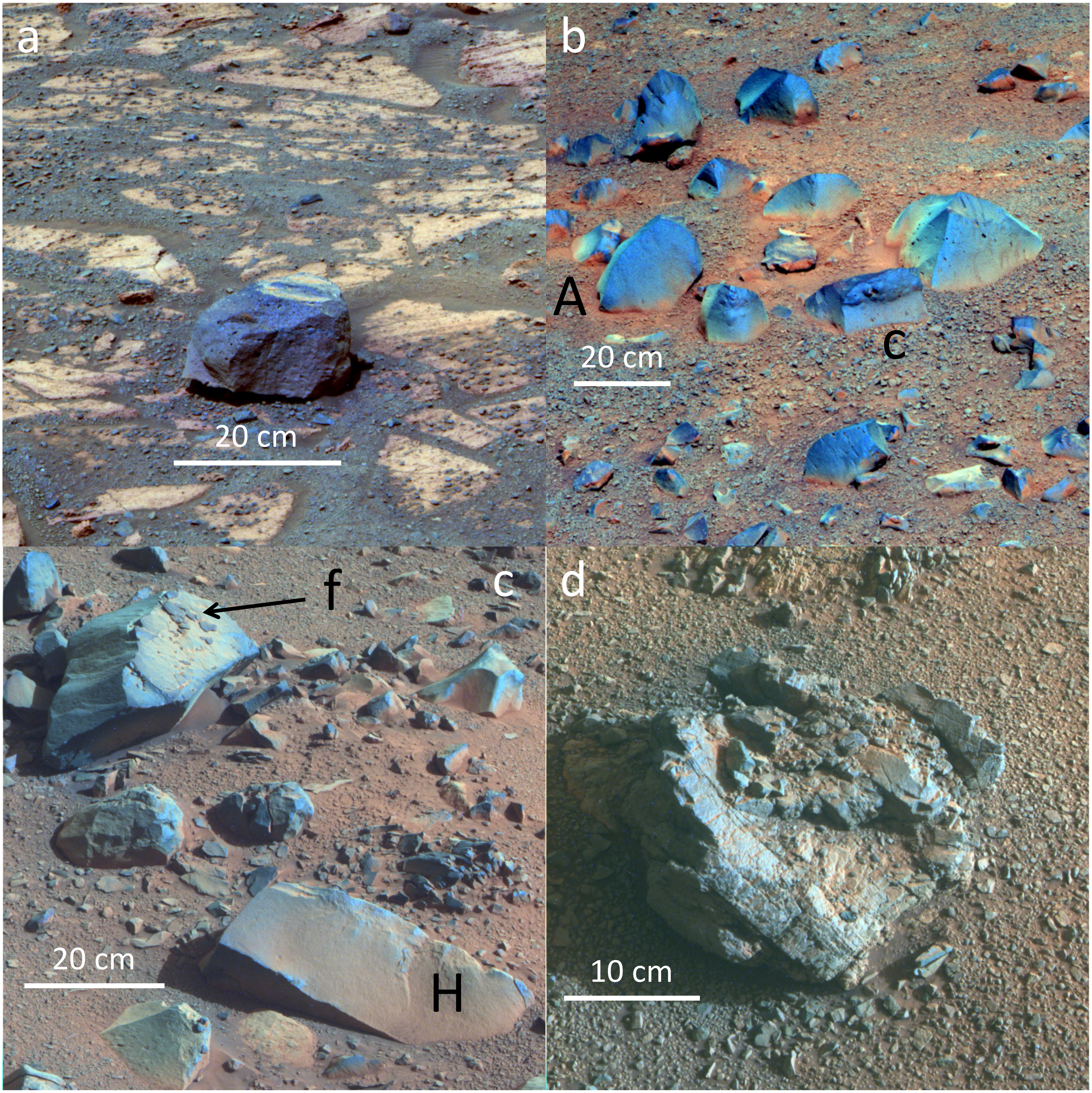
a
20 cm
b
A
c
20 cm
f
c
20 cm
H
d
10 cm

Figure 11.

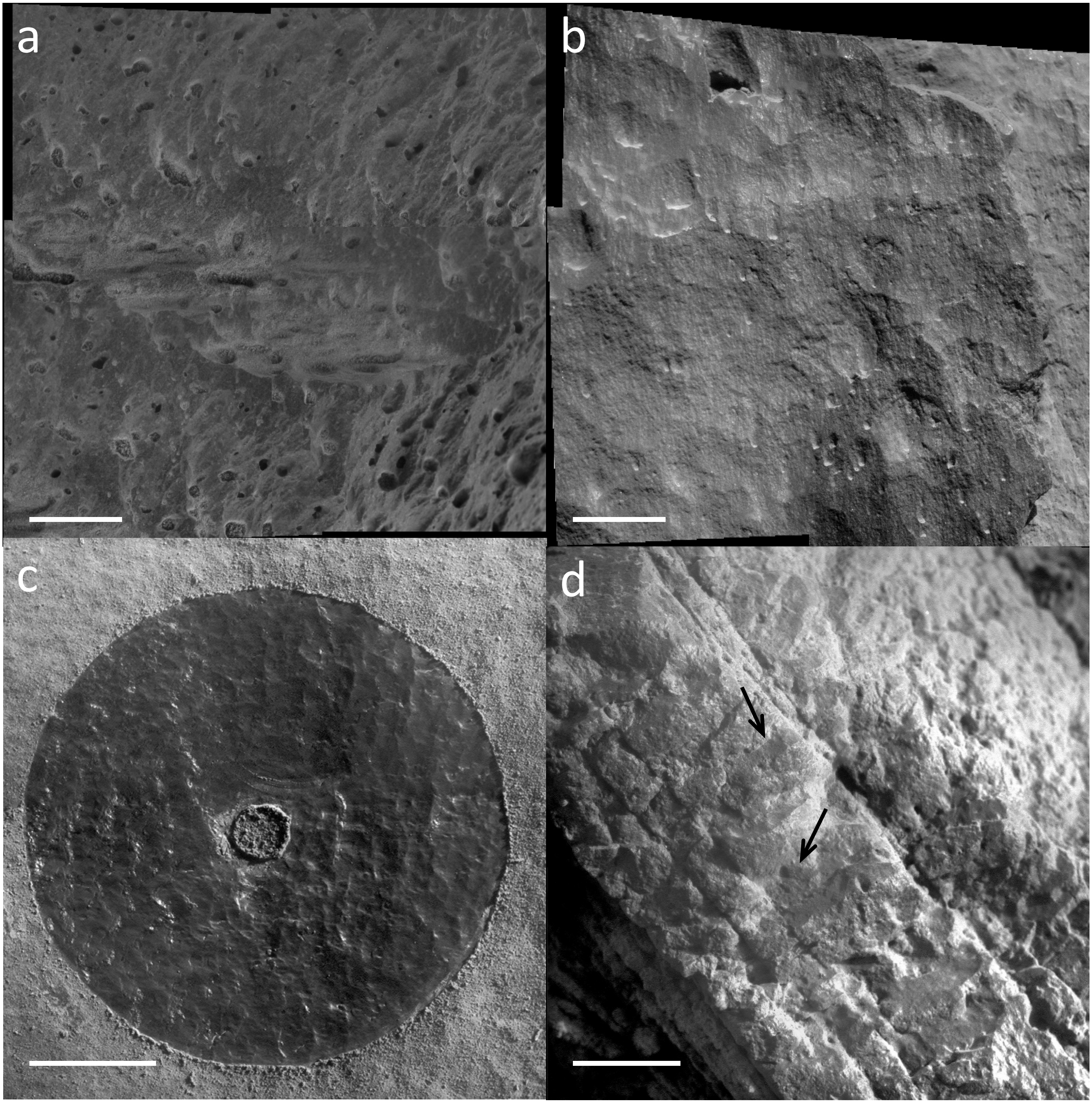
a
b
c
d

Figure 12.

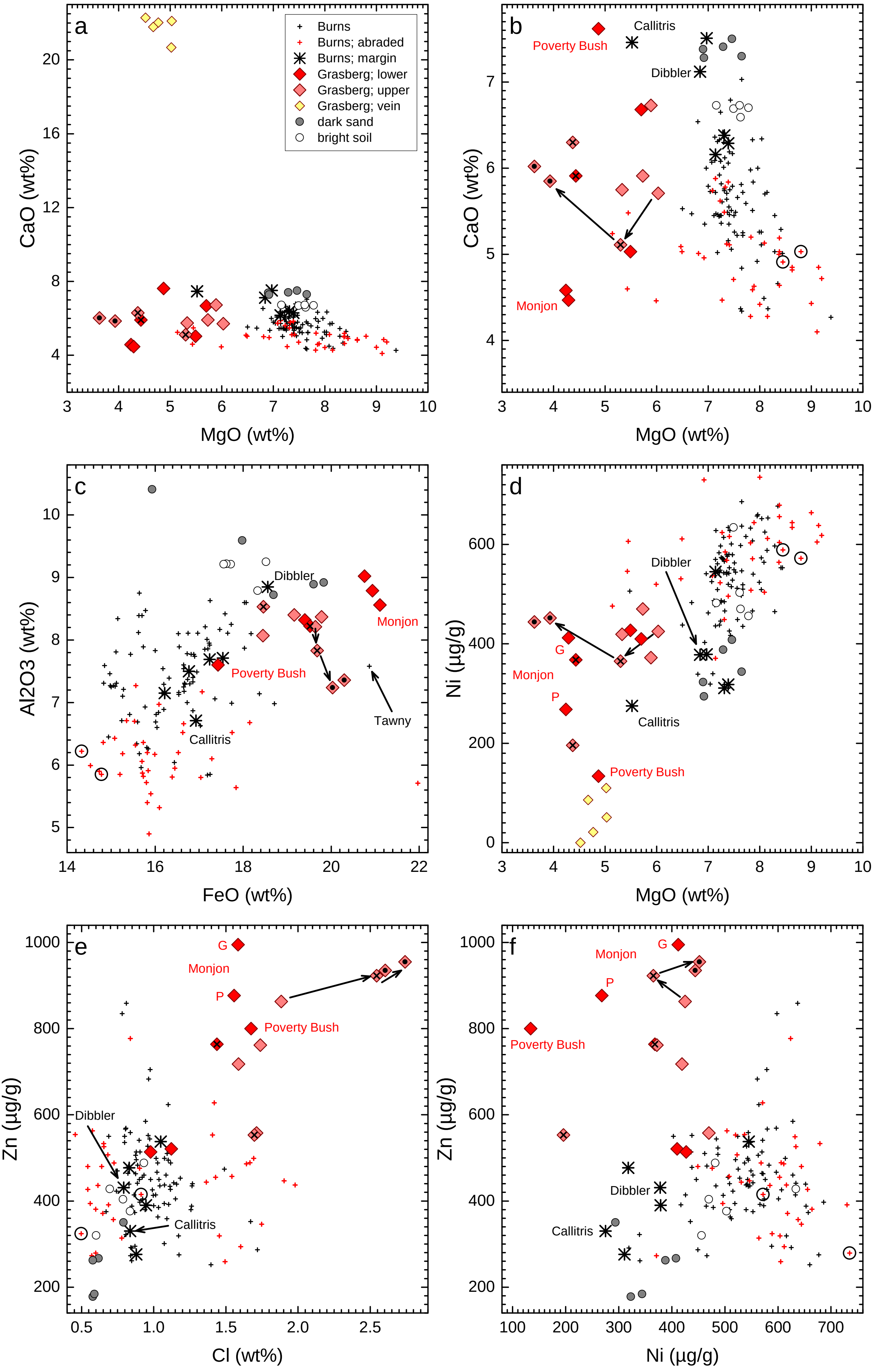

a
Burns
Burns; abraded
Burns; margin
Grasberg; lower
Grasberg; upper
Grasberg; vein
dark sand
bright soil
CaO (wt%)
MgO (wt%)
b
Callitris
Poverty Bush
Dibbler
Monjon
CaO (wt%)
MgO (wt%)
c
Dibbler
Monjon
Poverty Bush
Callitris
Tawny
Al2O3 (wt%)
FeO (wt%)
d
Dibbler
G
Monjon
P
Callitris
Poverty Bush
Ni (µg/g)
MgO (wt%)
e
G
Monjon
P
Poverty Bush
Dibbler
Callitris
Zn (µg/g)
Cl (wt%)
f
Monjon
G
P
Poverty Bush
Dibbler
Callitris
Zn (µg/g)
Ni (µg/g)

Figure 13.

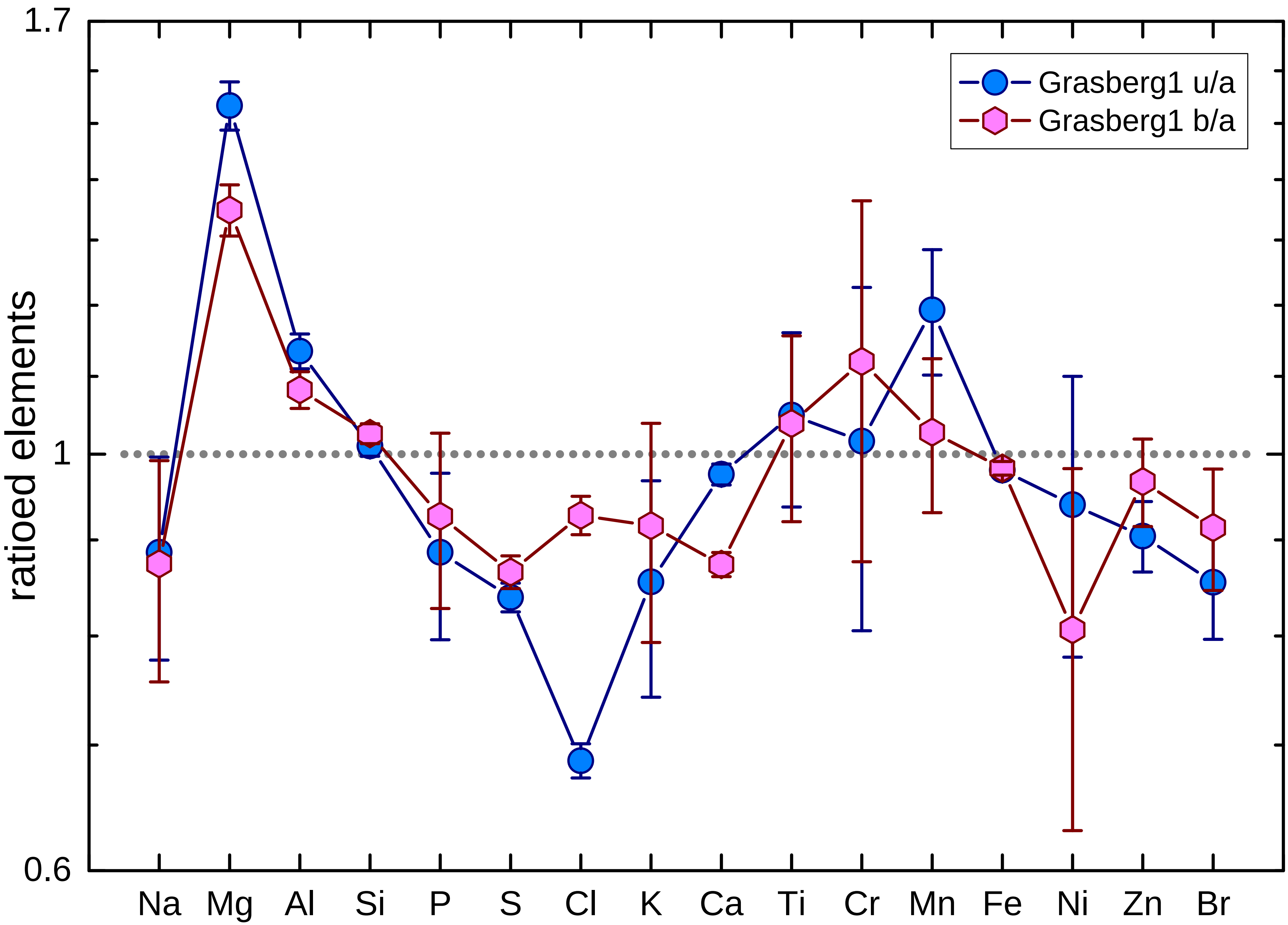
1.7
1
0.6
ratioed elements
Na
Mg
Al
Si
P
S
Cl
K
Ca
Ti
Cr
Mn
Fe
Ni
Zn
Br
Grasberg1 u/a
Grasberg1 b/a

Figure 14.

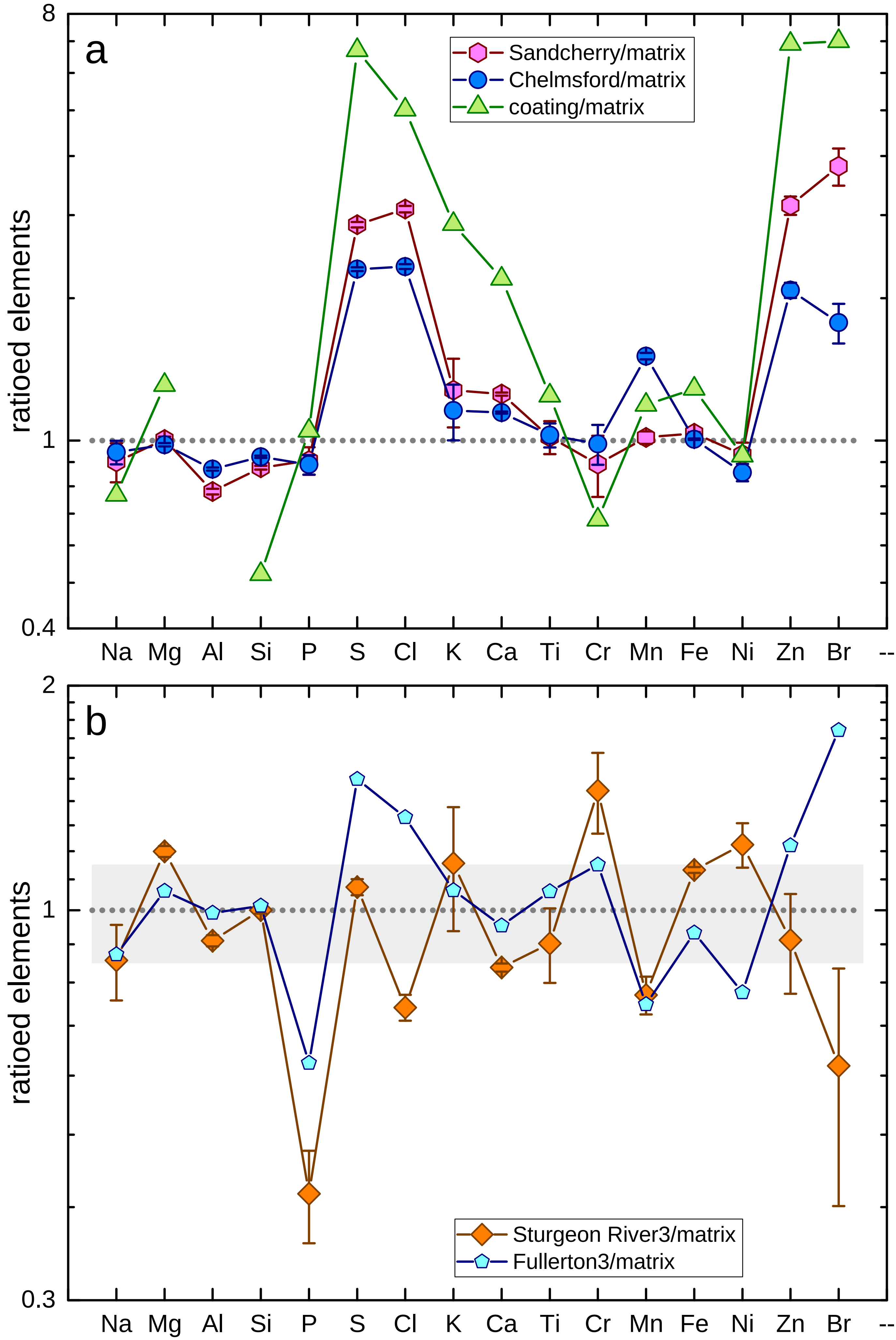

a
b
8
1
0.4
2
0.3
ratioed elements
Sandcherry/matrix
Chelmsford/matrix
coating/matrix
Sturgeon River3/matrix
Fullerton3/matrix
Na Mg Al Si P S Cl K Ca Ti Cr Mn Fe Ni Zn Br --

Figure 15.

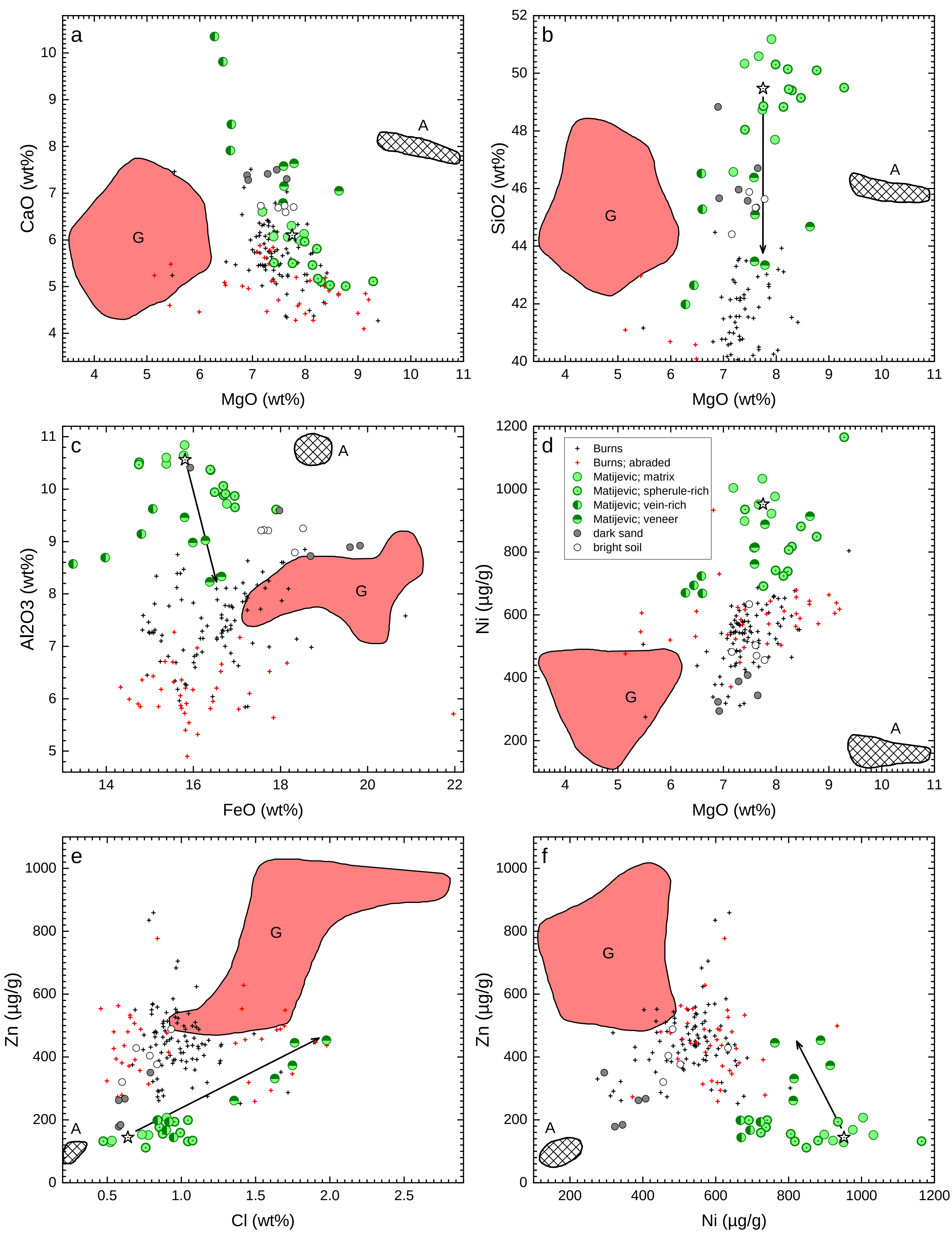

a
b
c
d
e
f
CaO (wt%)
MgO (wt%)
SiO2 (wt%)
Al2O3 (wt%)
FeO (wt%)
Ni (µg/g)
Zn (µg/g)
Cl (wt%)
G
A
Burns
Burns; abraded
Matijevic; matrix
Matijevic; spherule-rich
Matijevic; vein-rich
Matijevic; veneer
dark sand
bright soil

Figure 16.

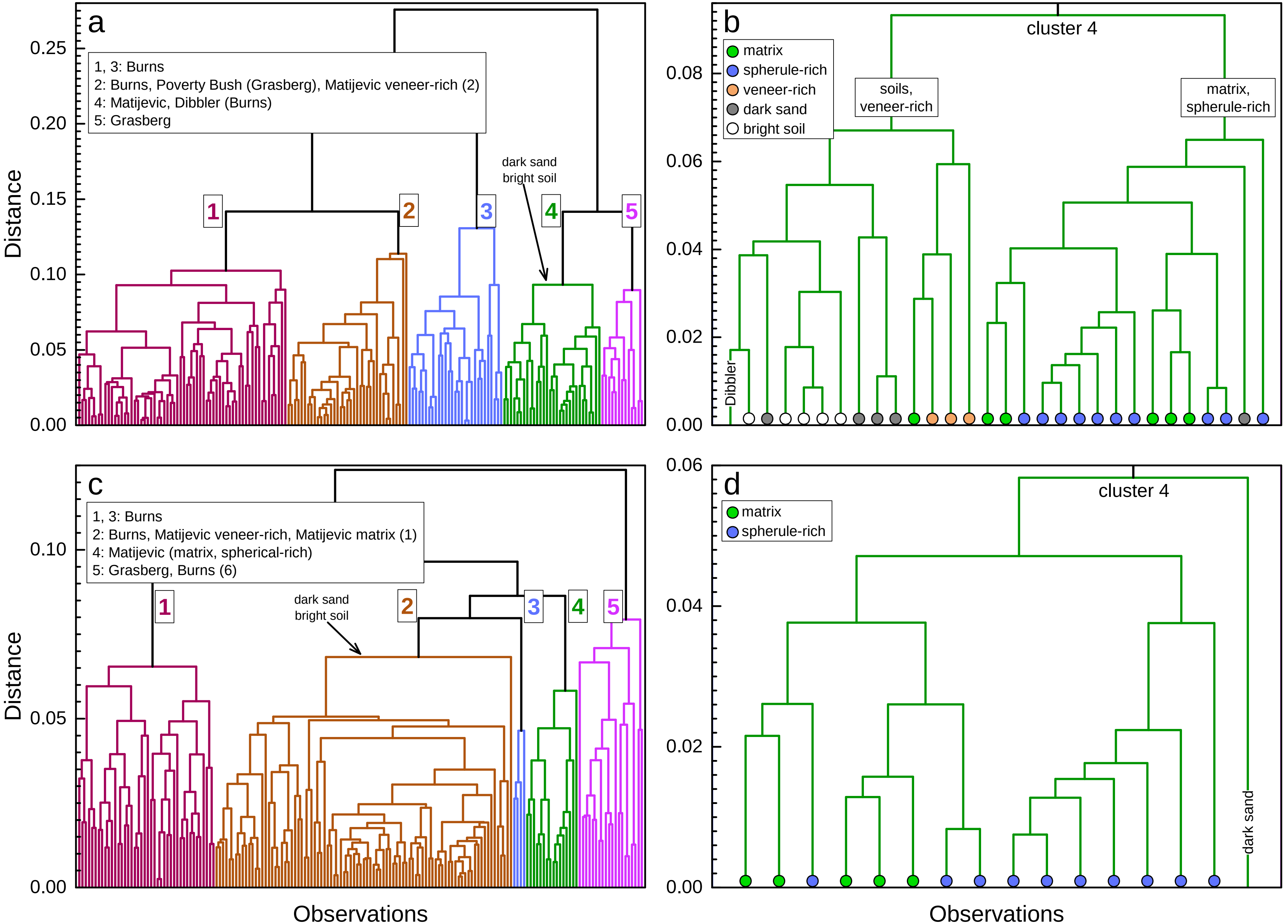
a
1, 3: Burns
2: Burns, Poverty Bush (Grasberg), Matijevic veneer-rich (2)
4: Matijevic, Dibbler (Burns)
5: Grasberg
dark sand
bright soil
1
2
3
4
5
Distance
0.00
0.05
0.10
0.15
0.20
0.25
b
cluster 4
matrix
spherule-rich
veneer-rich
dark sand
bright soil
soils, veneer-rich
matrix, spherule-rich
Dibbler
0.00
0.02
0.04
0.06
0.08
c
1, 3: Burns
2: Burns, Matijevic veneer-rich, Matijevic matrix (1)
4: Matijevic (matrix, spherical-rich)
5: Grasberg, Burns (6)
dark sand
bright soil
1
2
3
4
5
Distance
0.00
0.05
0.10
Observations
d
cluster 4
matrix
spherule-rich
dark sand
0.00
0.02
0.04
0.06
Observations

Figure 17.

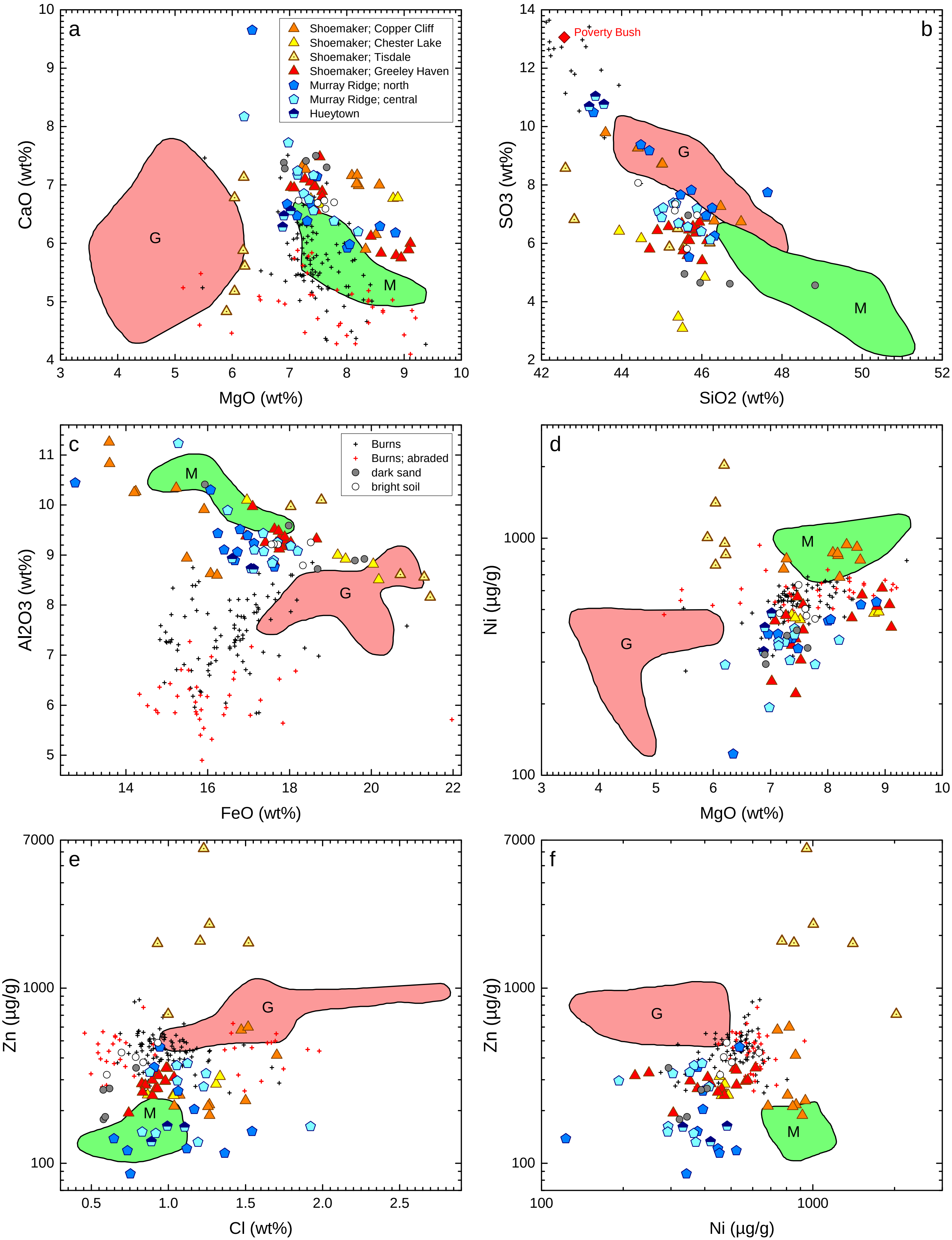
a
Shoemaker; Copper Cliff
Shoemaker; Chester Lake
Shoemaker; Tisdale
Shoemaker; Greeley Haven
Murray Ridge; north
Murray Ridge; central
Hueytown
G
M
CaO (wt%)
MgO (wt%)
b
Poverty Bush
SO3 (wt%)
SiO2 (wt%)
c
Burns
Burns; abraded
dark sand
bright soil
Al2O3 (wt%)
FeO (wt%)
d
Ni (µg/g)
MgO (wt%)
e
Zn (µg/g)
Cl (wt%)
f
Zn (µg/g)
Ni (µg/g)

Figure 18.

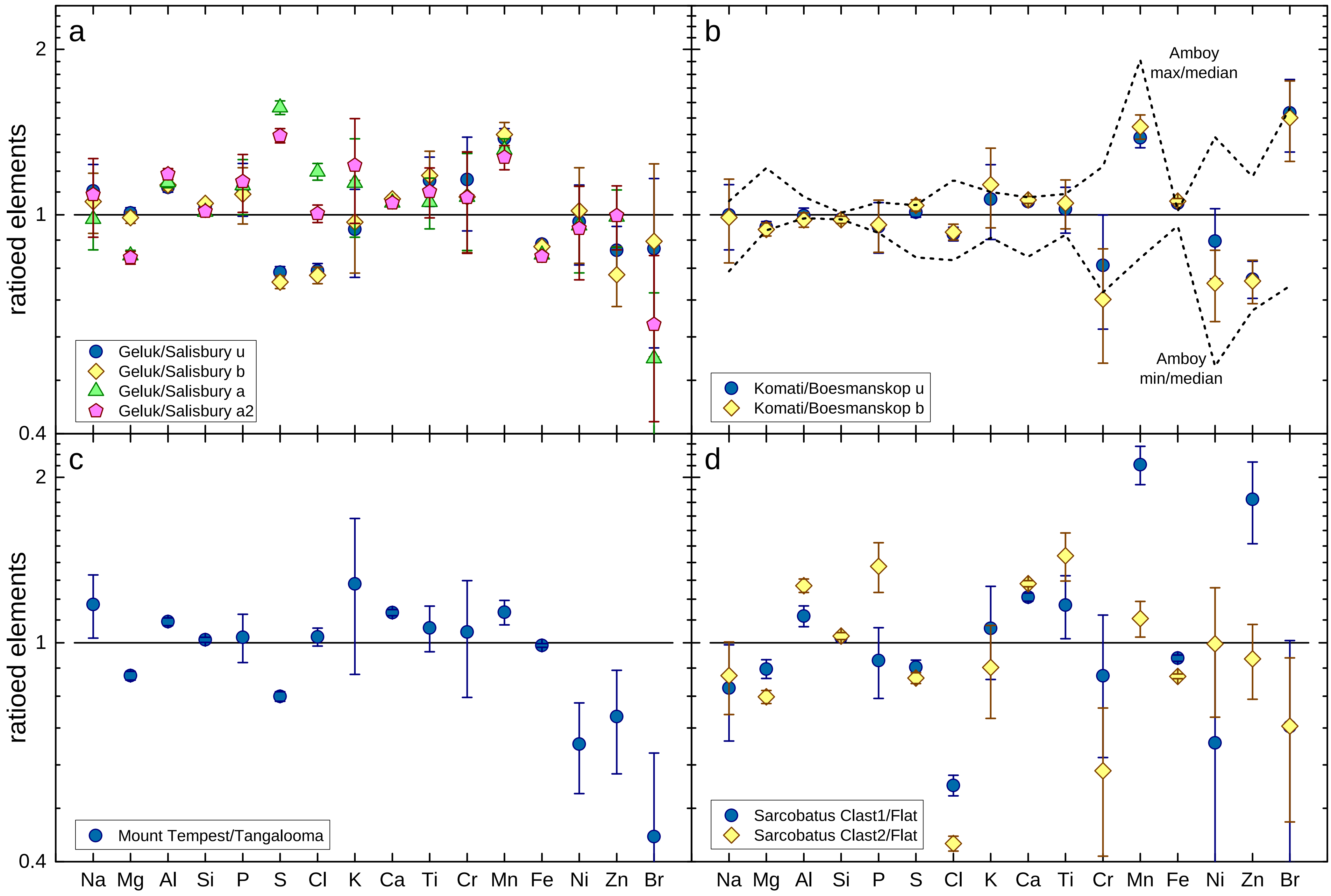

a
b
c
d
ratioed elements
ratioed elements
2
1
0.4
2
1
0.4
Geluk/Salisbury u
Geluk/Salisbury b
Geluk/Salisbury a
Geluk/Salisbury a2
Komati/Boesmanskop u
Komati/Boesmanskop b
Amboy
max/median
Amboy
min/median
Mount Tempest/Tangalooma
Sarcobatus Clast1/Flat
Sarcobatus Clast2/Flat
Na Mg Al Si P S Cl K Ca Ti Cr Mn Fe Ni Zn Br
Na Mg Al Si P S Cl K Ca Ti Cr Mn Fe Ni Zn Br

Figure 19.

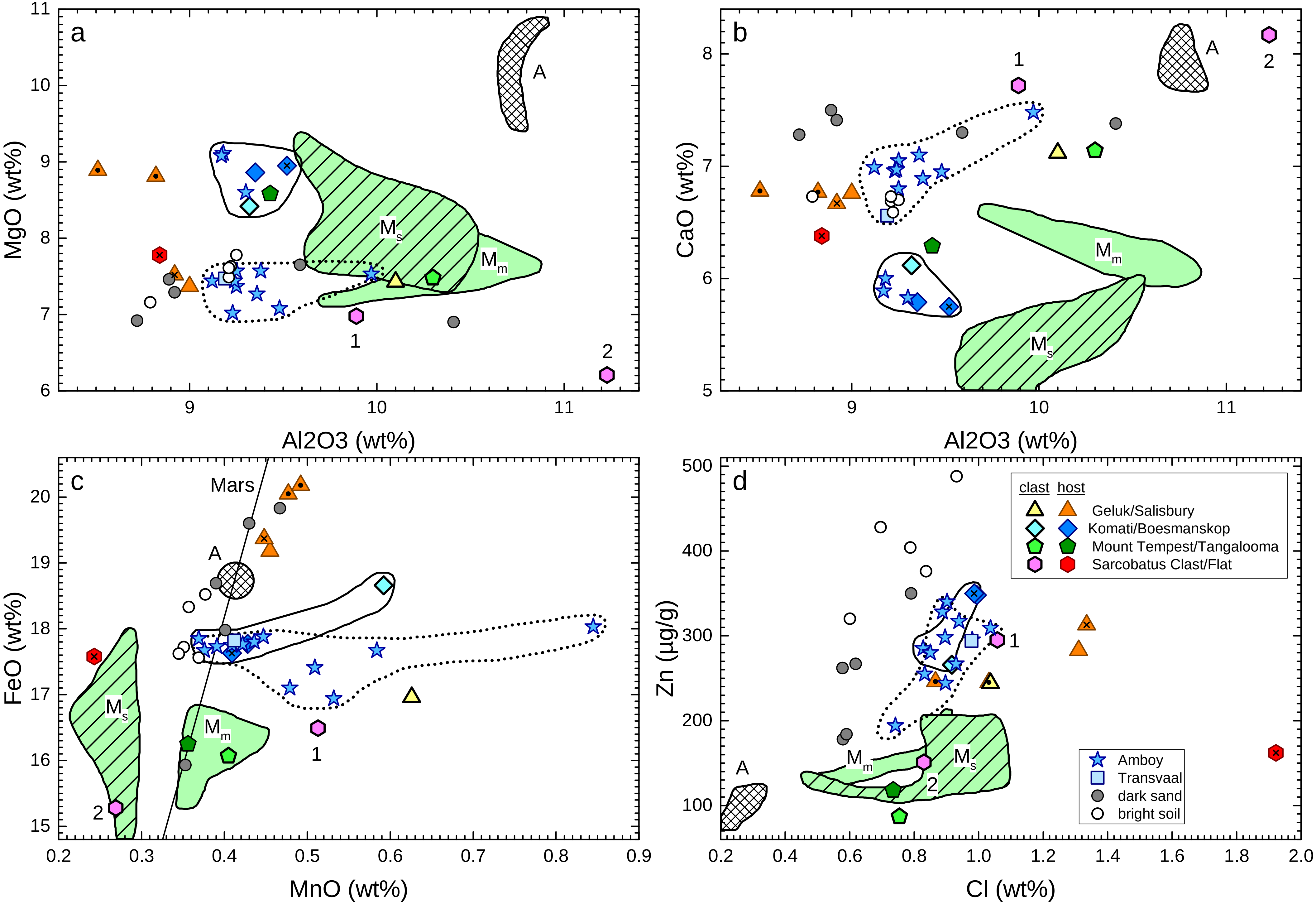
a
b
c
d
MgO (wt%)
CaO (wt%)
FeO (wt%)
Zn (µg/g)
Al2O3 (wt%)
MnO (wt%)
Cl (wt%)
A
Ms
Mm
Mars
1
2
clast host
Geluk/Salisbury
Komati/Boesmanskop
Mount Tempest/Tangalooma
Sarcobatus Clast/Flat
Amboy
Transvaal
dark sand
bright soil

Figure 20.

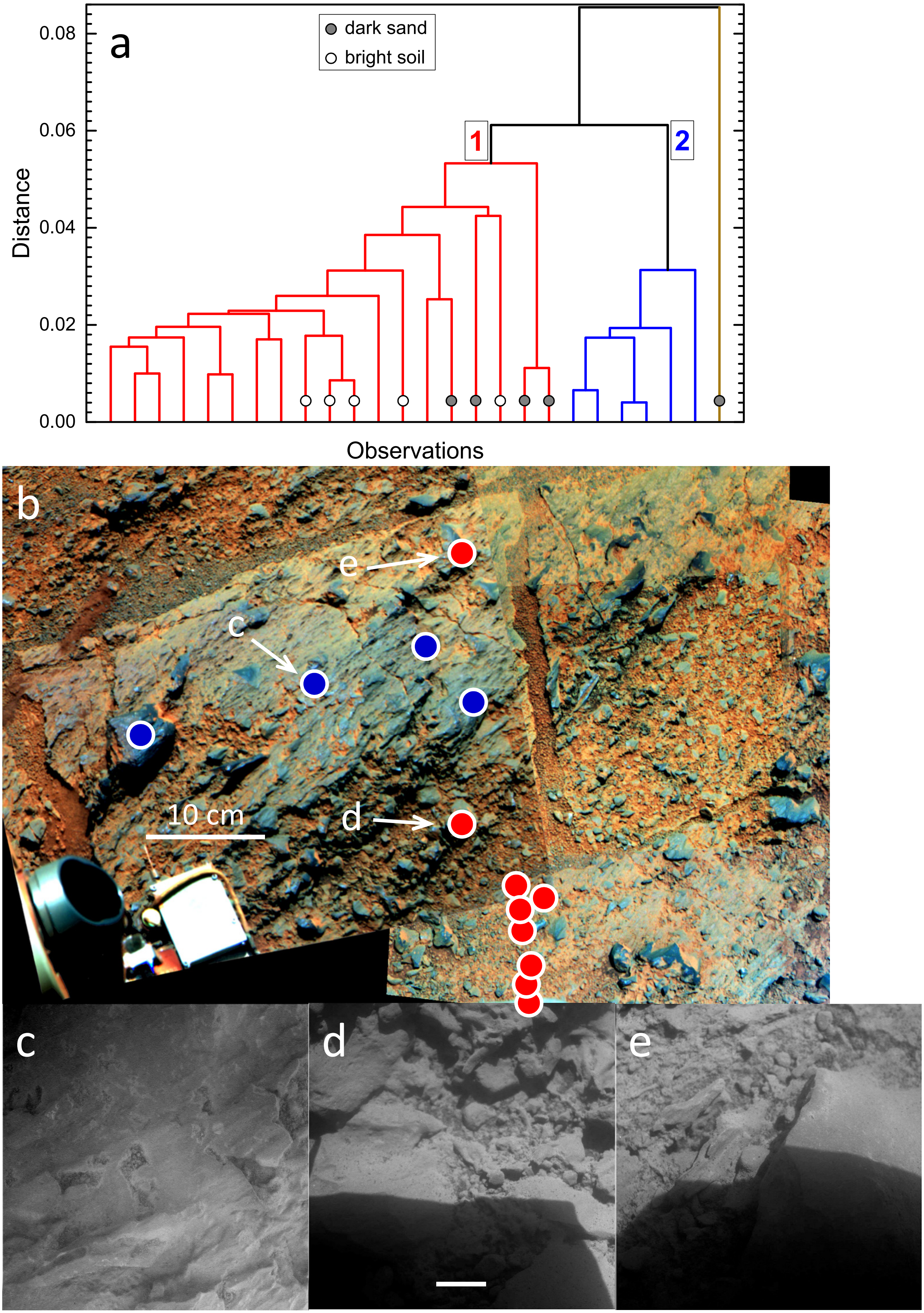

a
dark sand
bright soil
1
2
Distance
0.08
0.06
0.04
0.02
0.00
Observations
b
e
c
d
10 cm
c
d
e

Figure 21.

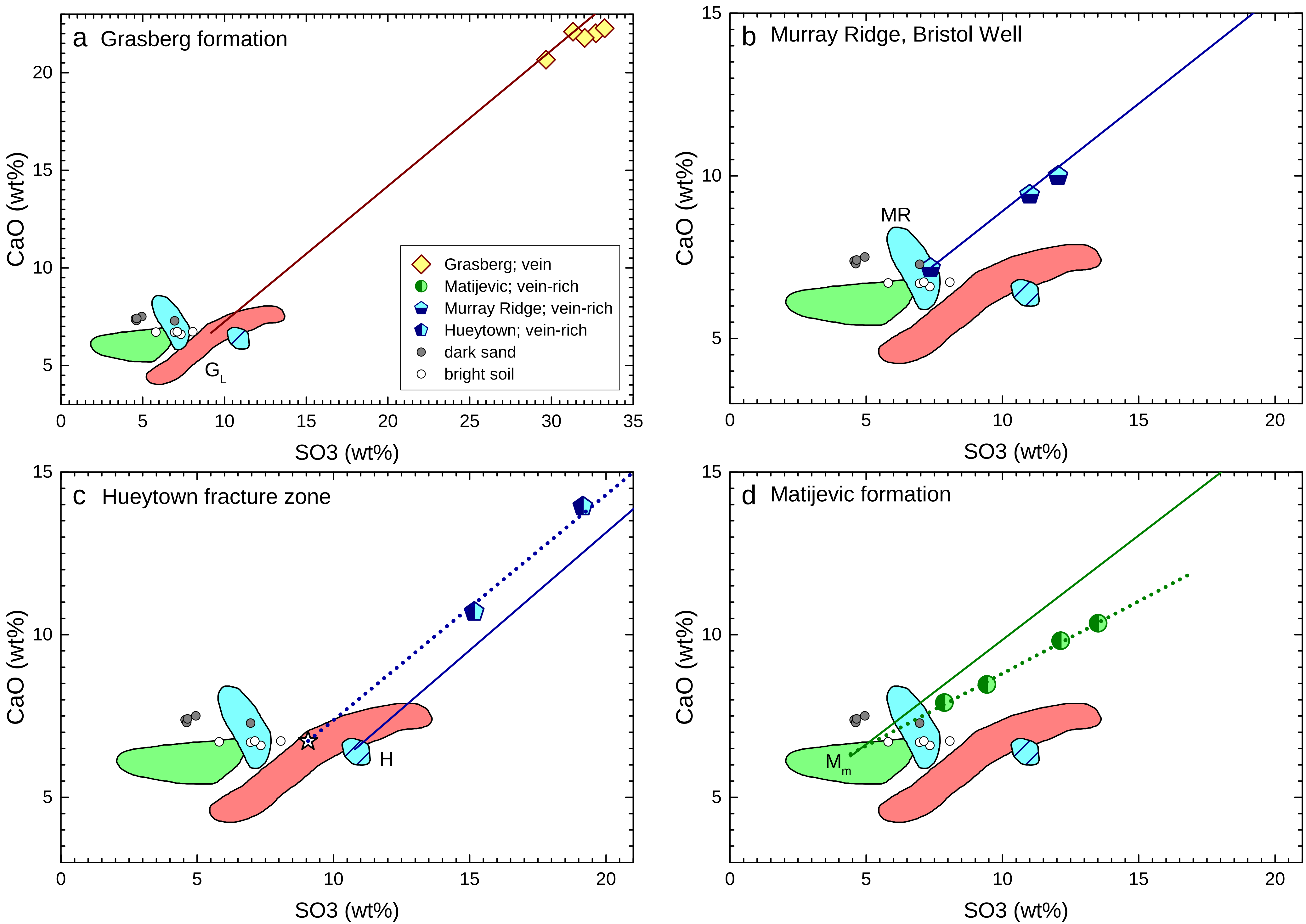

a Grasberg formation
Grasberg; vein
Matijevic; vein-rich
Murray Ridge; vein-rich
Hueytown; vein-rich
dark sand
bright soil
G_L
CaO (wt%)
SO3 (wt%)
b Murray Ridge, Bristol Well
MR
c Hueytown fracture zone
H
d Matijevic formation
M_m

Figure 22.

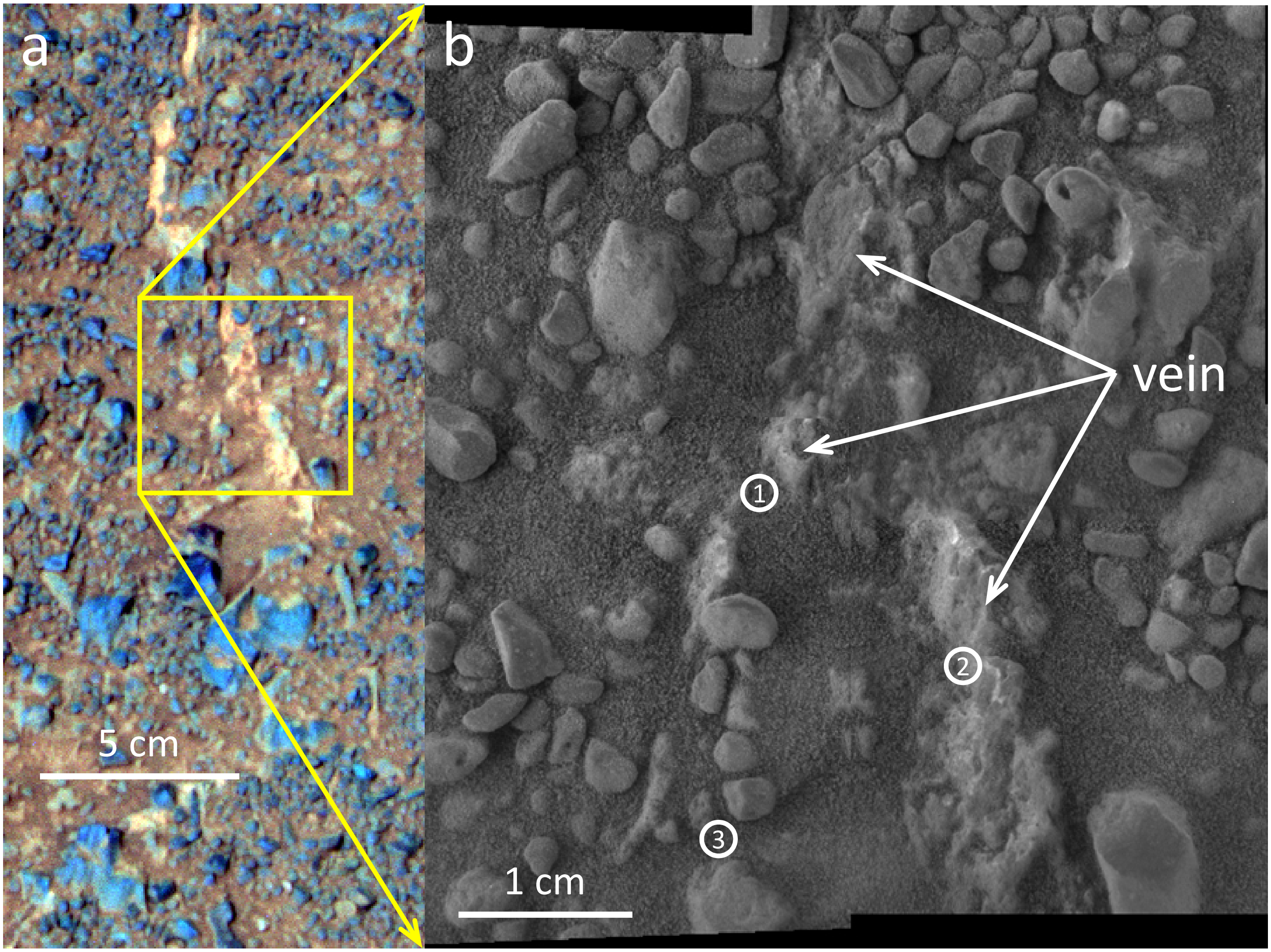
a
5 cm
b
vein
1
2
3
1 cm

Figure 23.

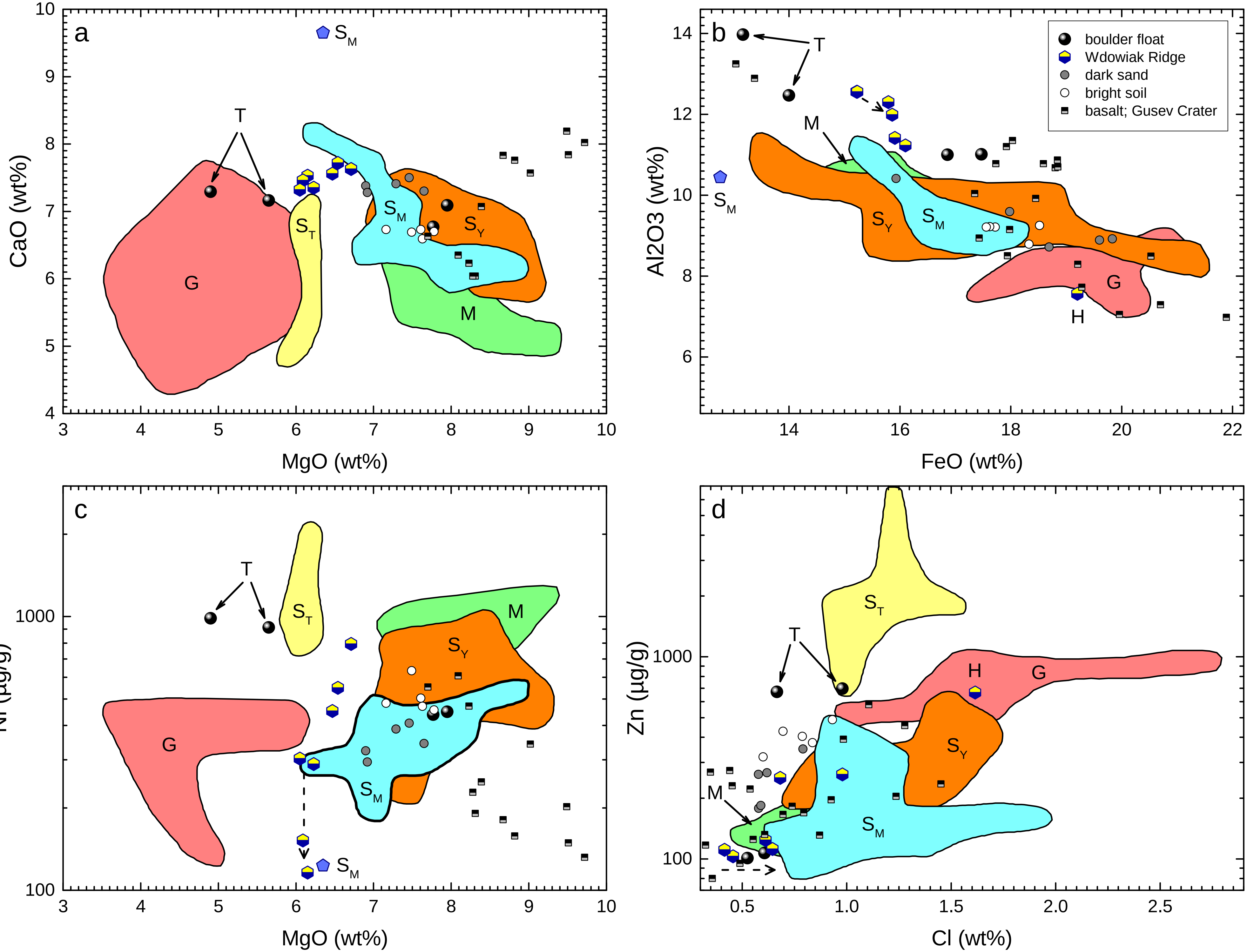

a
b
c
d
boulder float
Wdowiak Ridge
dark sand
bright soil
basalt; Gusev Crater
T
G
M
H
S_M
S_T
S_Y
CaO (wt%)
MgO (wt%)
Al2O3 (wt%)
FeO (wt%)
Ni (µg/g)
Zn (µg/g)
Cl (wt%)

Figure 24.

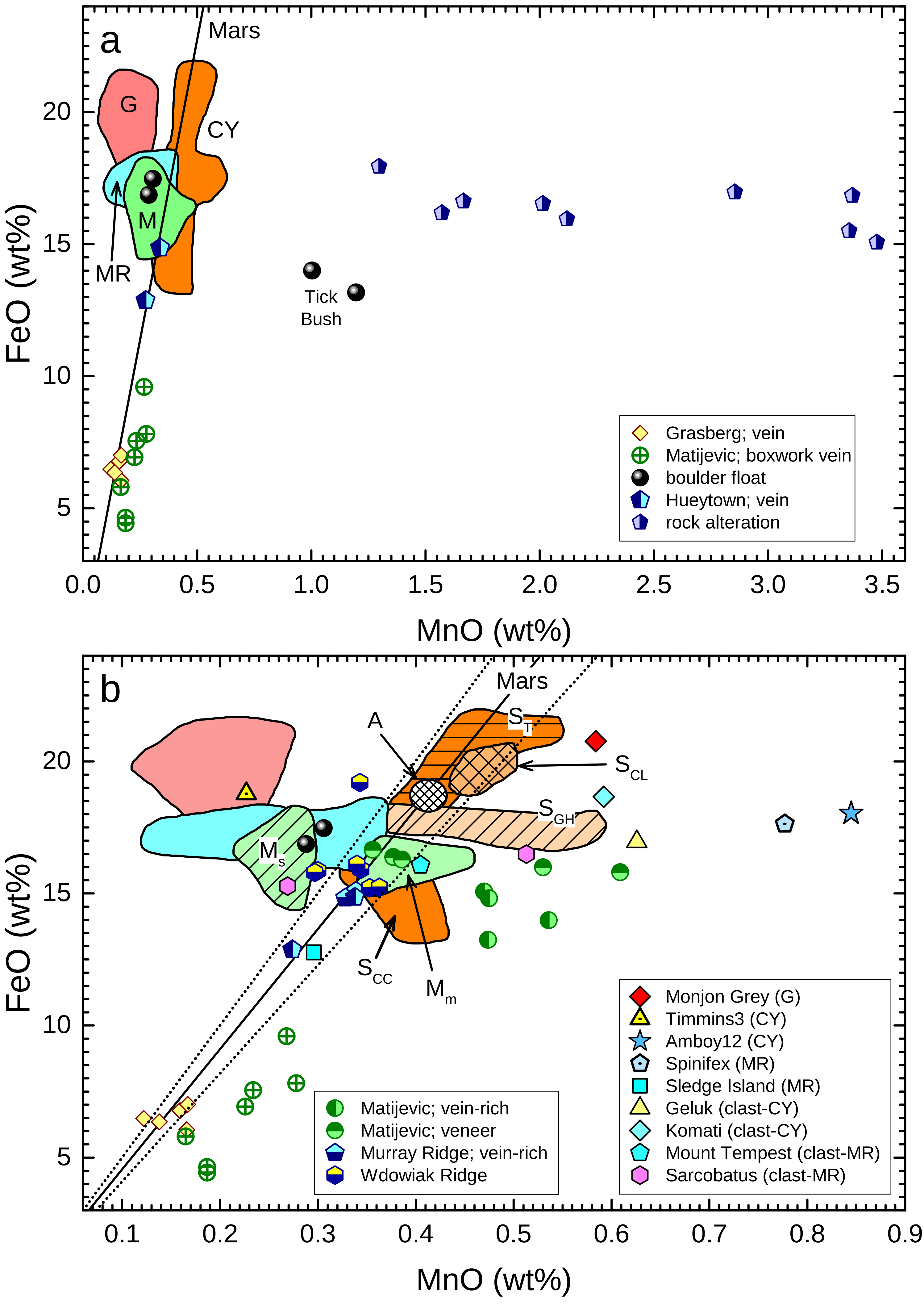
a
Mars
G
CY
M
MR
Tick
Bush
FeO (wt%)
MnO (wt%)
Grasberg; vein
Matijevic; boxwork vein
boulder float
Hueytown; vein
rock alteration
b
Mars
A
S$_T$
S$_{CL}$
S$_{GH}$
M$_s$
S$_{CC}$
M$_m$
Monjon Grey (G)
Timmins3 (CY)
Amboy12 (CY)
Spinifex (MR)
Sledge Island (MR)
Geluk (clast-CY)
Komati (clast-CY)
Mount Tempest (clast-MR)
Sarcobatus (clast-MR)
Matijevic; vein-rich
Matijevic; veneer
Murray Ridge; vein-rich
Wdowiak Ridge

Figure 25.

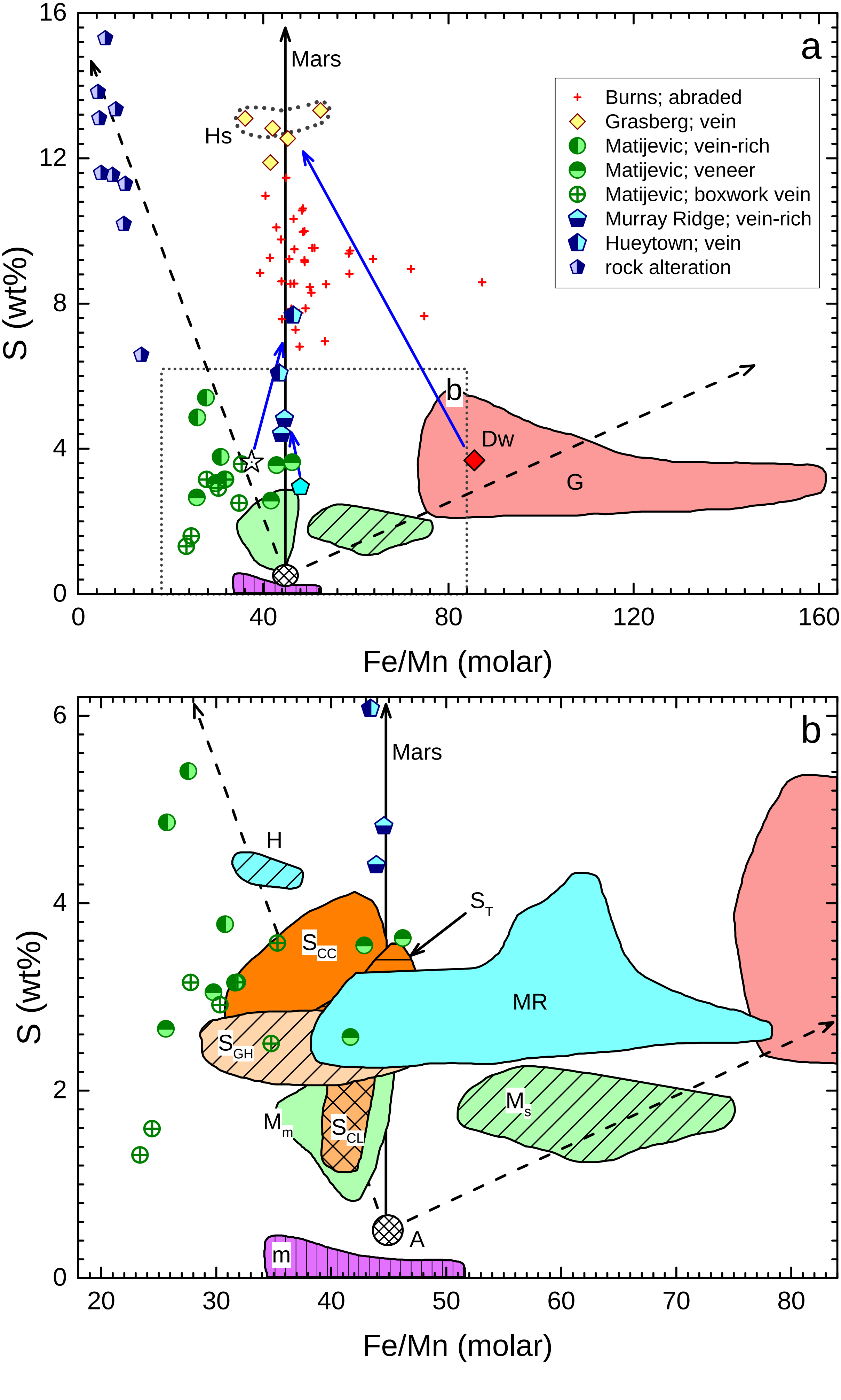

a
b
S (wt%)
Fe/Mn (molar)
Mars
Hs
Dw
G
Burns; abraded
Grasberg; vein
Matijevic; vein-rich
Matijevic; veneer
Matijevic; boxwork vein
Murray Ridge; vein-rich
Hueytown; vein
rock alteration
H
S_T
S_{CC}
MR
S_{GH}
M_m
S_{CL}
M_s
A
m

Figure 26.

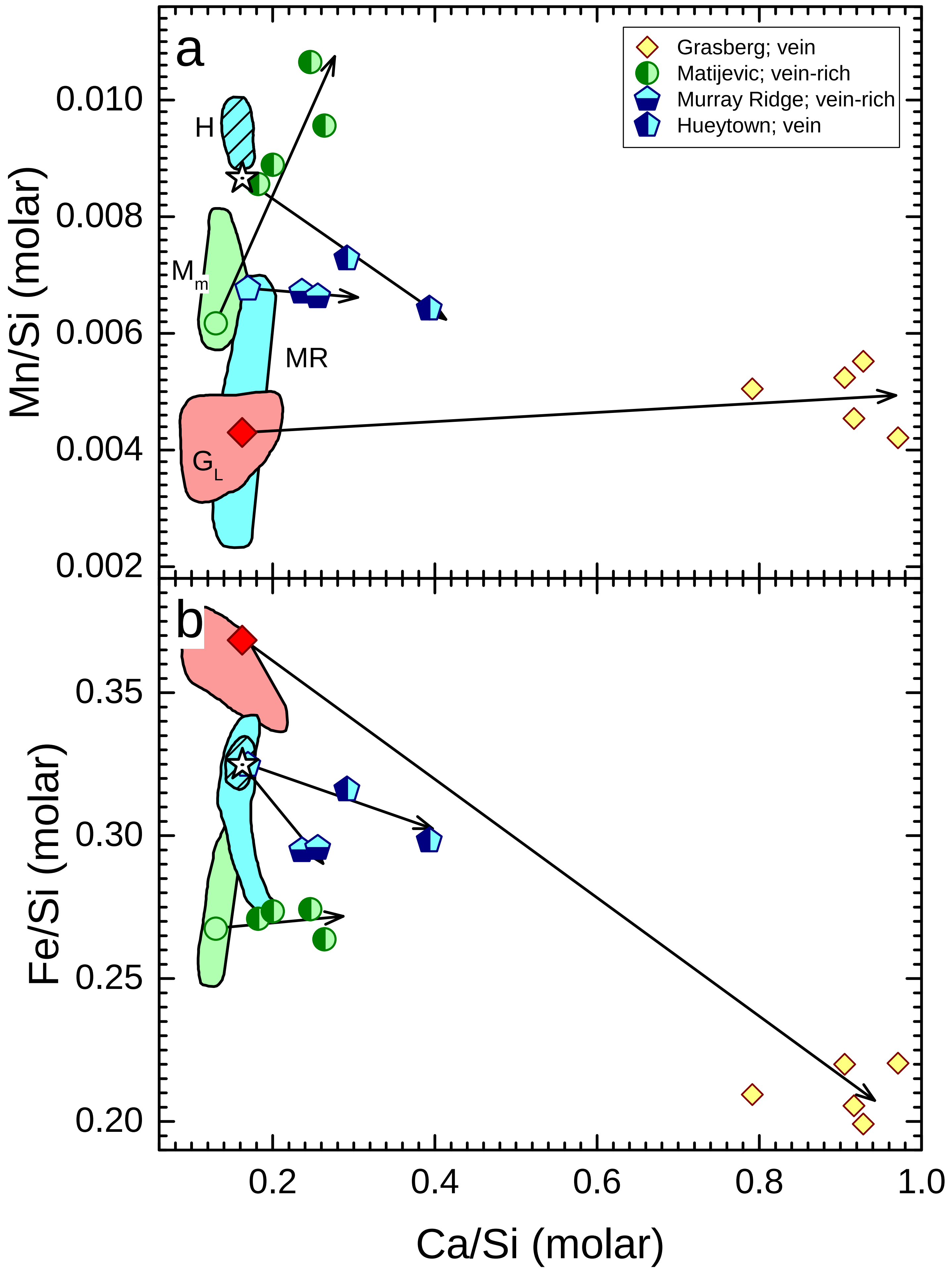

a
b
Grasberg; vein
Matijevic; vein-rich
Murray Ridge; vein-rich
Hueytown; vein
H
M m
MR
G L
0.010
0.008
0.006
0.004
0.002
Mn/Si (molar)
0.35
0.30
0.25
0.20
Fe/Si (molar)
0.2
0.4
0.6
0.8
1.0
Ca/Si (molar)